

**ANION-CONDUCTIVE MULTIBLOCK AROMATIC COPOLYMER  
MEMBRANES: STRUCTURE-PROPERTY RELATIONSHIPS**

A dissertation  
Presented to  
The Academic Faculty

by

Doh-Yeon Park

In Partial Fulfillment  
of the Requirements for the Degree  
Doctor of Philosophy in the  
School of Materials Science and Engineering

Georgia Institute of Technology  
August 2013

**COPYRIGHT 2013 BY DOH-YEON PARK**

**ANION-CONDUCTIVE MULTIBLOCK AROMATIC COPOLYMER  
MEMBRANES: STRUCTURE-PROPERTY RELATIONSHIPS**

Approved by:

Dr. Haskell W. Beckham, Advisor  
School of Materials Science and  
Engineering  
*Georgia Institute of Technology*

Dr. Paul A. Kohl  
School of Chemical and Biomolecular  
Engineering  
*Georgia Institute of Technology*

Dr. Anselm C. Griffin  
School of Materials Science and  
Engineering  
*Georgia Institute of Technology*

Dr. David G. Bucknall  
School of Materials Science and  
Engineering  
*Georgia Institute of Technology*

Dr. Seung Soon Jang  
School of Materials Science and  
Engineering  
*Georgia Institute of Technology*

Date Approved: [June 19, 2013]

[I sincerely dedicate this dissertation to my precious wife who is my supporter, counselor,  
and encourager]

## ACKNOWLEDGEMENTS

Without kind helps, valuable advises, and sincere encouragement from many people around me, I could not have made it where I am now. My special thanks go to my advisor, Dr. Haskell Beckham. He has given me tremendous opportunities to research the themes that I wanted to do and never hesitated to lend a help and support. I was also very fortunate to meet and work with Dr. Paul Kohl. Thanks to his guidance and insights, I was able to learn a lot about things that I was not familiar with. I would also like to thank my committee members, Drs. Anselm Griffin, David Bucknall, and Seung Soon Jang, and Drs. Stefan France and Leslie Gelbaum for their instructions and fruitful discussions. Dr. Johannes Leisen deserves my gratitude because I benefited from his deep knowledge and great experience for NMR experiments.

I must not forget to express my appreciation to my friends and colleagues. Dr. Rudra Choudhury has been my go-to guy whenever my works did not go well and a friend to whom I can open my mind as well. I'm thankful for him. Dr. Ryan Kincer was a great helper for me to settle in new environment during my early graduate student life. John Ahlfield, Dr. Junfeng Zhou's helps have been of great value in my research. I also owe thanks to many Korean friends for their kind friendship.

I want my parents and parents-in-law to have my heartfelt gratitude. They have always been there for provide unconditional care and supports in times of joy and trouble. Finally, I cannot thank my lovely wife, OkSo Lee, enough for her supports, patients, and prayers for me. She has to get my deepest appreciation and love.

# TABLE OF CONTENTS

	Page
ACKNOWLEDGEMENTS	iv
LIST OF TABLES	ix
LIST OF FIGURES	x
LIST OF SCHEMES	xiv
LIST OF SYMBOLS AND ABBREVIATIONS	xv
SUMMARY	xviii
 <u>CHAPTER</u>	
1 INTRODUCTION	1
1.1. Fuel Cell	1
1.2. Proton Exchange Membrane and Anion Exchange Membrane Fuel Cells	5
1.3. Conductivity Relating to Polymer Morphology	9
1.4. Previous Studies of Water Mobility in Fuel Cell Membranes	14
1.4.1. Imaging techniques	15
1.4.2. NMR relaxation times	16
1.4.3 Differential scanning calorimetry	18
1.5. Stability of Anion Conductive Membrane at High pH and Temperature	20
1.6. Research Objectives and Strategies	23
1.6.1. Multiblock copolymers for a model material	25
1.6.2. Characterization techniques of water transport in the membranes	26
1.6.3. Quantitative chemical stability test for anion conductive multiblock copolymers and fluorinated poly(aryl ether)s having different ion exchange groups	26

1.6.4. Usage of multiblock copolymers and poly aryl(ether)s for alkaline fuel cells	27
2 SYNTHESIS AND CHEMICAL STRUCTURE DETERMINATION OF MULTIBLOCK COPOLYMERS	29
2.1. Introduction and Objectives	30
2.2. Experimental Details	29
2.2.1. Materials	30
2.2.2. Synthesis of monomer, 3,3',4,4'-tetrafluorodiphenylsulfone (TFDPS)	30
2.2.3. Multiblock copolymerization (I)	31
2.2.4. Multiblock copolymerization (II)	32
2.2.5. Chloromethylation, quaternization, and membrane casting	34
2.2.6. Measurements	34
2.3. Results and Discussion	36
2.3.1. Synthesis and chemical structure determination of multiblock copolymers (mPES and mFPES) and random copolymers (rPES)	36
2.3.2. Synthesis and characterization of chloromethylated (CmPES and CmFPES) and quaternized multiblock copolymers (QmPES and QmFPES)	47
2.3.3. Membrane formation, water uptake, and hydroxide ion conductivity of QmPES and QmFPES	54
3 NMR RELAXATION TIMES FOR CHARACTERIZING THE EFFICIENCY OF ION CHANNELS	59
3.1. Introduction and Objectives	59
3.2. Experimental Details	60
3.3. Results and Discussion	60
4 DSC STUDY FOR THE CHARACTERIZATION OF VARIOUS WATER STATES IN THE MEMBRANE	69
4.1. Introduction and Objectives	69

4.2. Experimental Details	70
4.3. Results and Discussion	71
5 THE STUDY OF DIFFUSION ACTIVATION ENERGY FOR EXPLORING ANION TRANSPORTING MECHANISMS	75
5.1. Introduction and Objectives	75
5.2. Experimental Details	77
5.3. Results and Discussion	78
6 QUANTITATIVE CHEMICAL STABILITY TEST FOR ANION CONDUCTIVE MEMBRANE WITH <sup>1</sup> H AND DIFFUSION-ORDERED NMR SPECTROSCOPY	83
6.1. Introduction and Objectives	83
6.2. Experimental Details	85
6.2.1. Materials	85
6.2.2. Measurements	85
6.3. Results and Discussion	88
7 USAGE OF SYNTHESIZED ANION CONDUCTIVE POLYMERS FOR HYBRID DIRECT METHANOL FUEL CELLS	98
7.1. Introduction and Objectives	98
7.2. Experimental Details	101
7.2.1. Materials	101
7.2.2. Electrode fabrication	101
7.2.3. MEA assembly	103
7.3. Results and Discussion	103
7.3.1. Different ion exchange groups	103
7.3.2. Different circulation rate of methanol	106
7.3.3. Different oxidants (oxygen and air)	107

7.3.4. Different fabrication methods (thin-film and ionomer impregnation)	108
7.3.5. Multiblock copolymer ionomers	110
8. CONCLUSION AND FUTURE WORKS	113
8.1. Summary and Concluding Remarks	113
8.2. Suggested Future Works	115
8.2.1. Further development of nanostructure for more efficient ion conduction	115
8.2.2. Ion exchange groups other than quaternary ammonium groups	116
8.2.3. Nanocomposite polymer membranes for alkaline fuel cells	117
APPENDIX A: DIFFUSION ORDERED SPECTROSCOPY FOR CYLINDRICAL POLYMER BRUSHES	118
A.1. Introduction and Objectives	118
A.2. Experimental Details	119
A.3. Results and Discussion	120
REFERENCES	124

## LIST OF TABLES

	Page
Table 1.1: Comparison of fuel cell technologies	4
Table 1.2: Electrochemical reactions and charge carriers in fuel cells	5
Table 1.3: Representative examples of AEMs for the alkaline fuel cell	24
Table 2.1: Structural characteristics and properties of multiblock and random copoly(arylene ether sulfone)s	45
Table 3.1: Water uptake, IEC, relaxation times, and ion conductivity of QPES membranes	61
Table 3.2: Structural characteristics and properties of a series of mFPESs	67
Table 4.1: The quantity of non-freezable and freezable water molecules relating to IEC and water uptake in mFPES membranes	73
Table 5.1: The activation energy and conductivity of diffusion for the membranes and bulk water	81
Table 6.1: Percentage of remaining benzyltrimethyl ammonium groups relative to the initial state, which are determined by the integral ratio with respect to internal standard, DMSO	95
Table 7.1: Electrochemical reaction of methanol and hydrogen based fuel cells	99
Table 7.2: Properties of selected multiblock copolymers as an ionomer of the AEM cathode	111

## LIST OF FIGURES

	Page
Figure 1.1: Typical polarization curve of a hydrogen/air polymer electrolyte membrane fuel cells	2
Figure 1.2: Schematic diagram of the proton exchange membrane fuel cell	6
Figure 1.3: Schematic diagram of the anion exchange membrane fuel cell	7
Figure 1.4: Possible dominant transport mechanisms for hydroxide in the anion exchange membrane, analog to those for proton transport	11
Figure 1.5: Transport mechanism of hydrated ions in aqueous solution	12
Figure 1.6: Schematic diagram illustrating the different types of water in the hydrophilic pore of a membrane; Reducing the humidity reduces the amount of freezable water present in the pore and alters its size	19
Figure 1.7: Various degradation routes for anion conductive membrane containing quaternary ammonium groups: (a) Hofmann elimination, (b) nucleophilic substitution, and (c) ylide formation	21
Figure 1.8: Proposed aryl-ether cleavage of benyltrimethylammonium-functionalized poly(aryl ether)s under high pH environments	22
Figure 1.9: An illustration of the main resistances in alkaline fuel cells: (1) an inhibition of the oxygen diffusion by the blocking of secondary pores, (2) resistance to oxygen permeation from the secondary pores to a reaction site through the ionomer layers, and (3) a limitation of anion conductivity	28
Figure 2.1: $^1\text{H}$ spectra of SDFB and TFDDBS	37
Figure 2.2: $^1\text{H}$ NMR spectra of (a) the OH-terminated oligomer ( $X = 6.7$ ), (b) the F-terminated oligomer ( $Y = 7.7$ ), and (c) the resulting multiblock copolymer mPES- $X_{6.7}Y_{7.7}$	41
Figure 2.3: $^1\text{H}$ NMR spectra of (a) the OH-terminated oligomer ( $X = 4.8$ ), (b) the F-terminated oligomer ( $Y = 6.0$ ), and (c) the resulting multiblock copolymer mFPES- $X_{4.8}Y_{6.0}$	43
Figure 2.4: COSY spectra of (a) multiblock copolymer mPES- $X_{6.7}Y_{7.7}$ and (b) multiblock copolymer mFPES- $X_{4.8}Y_{6.0}$	44

Figure 2.5: Gel permeation chromatograms of reactant oligomers, the resulting multiblock copolymer; (a) mPES- $X_{6.7}Y_{7.7}$ , and the corresponding chloromethylated product CmPES- $X_{6.7}Y_{7.7}$ , (b) mFPES- $X_{4.8}Y_{6.0}$ , and the corresponding chloromethylated product CmFPES- $X_{4.8}Y_{6.0}$	46
Figure 2.6: Selected aromatic region of DEPT-135 $^{13}\text{C}$ NMR spectra of (a) the multiblock copoly(arylene ether sulfone), mPES- $X_{6.7}Y_{7.7}$ and (b) the random copoly(arylene ether sulfone), rPES- $X_{0.5\text{N}}Y_{0.5\text{N}}$	47
Figure 2.7: $^1\text{H}$ NMR spectra of the multiblock copoly(arylene ether sulfone), mPES- $X_{6.7}Y_{7.7}$ , after (a) chloromethylation to give CmPES- $X_{6.7}Y_{7.7}$ , and (b) quaternization to give QmPES- $X_{6.7}Y_{7.7}$	49
Figure 2.8: $^1\text{H}$ NMR spectra of the multiblock copoly(arylene ether sulfone), mFPES- $X_{4.8}Y_{6.0}$ , after (a) chloromethylation to give CmFPES- $X_{4.8}Y_{6.0}$ , and (b) quaternization to give QmFPES- $X_{4.8}Y_{6.0}$	52
Figure 2.9: HMBC NMR spectra of the chloromethylated multiblock copoly(arylene ether sulfone)s, (a) CmPES- $X_{6.7}Y_{7.7}$ .and (b) CmFPES- $X_{4.8}Y_{6.0}$	53
Figure 2.10: Experimental phase diagram for PS-b-PI diblock copolymer	56
Figure 2.11: Tapping mode AFM phase images: (a) QmFPES- $X_{5.6}Y_{14.7}$ , (b) QrFPES- $X_{0.5\text{N}}Y_{0.5\text{N}}$ , and (c) dry QmFPES- $X_{5.6}Y_{14.7}$	58
Figure 3.1: $^1\text{H}$ NMR stack plot of CPMG spectra of QmPES- $X_{6.7}Y_{3.4}$ as a function of the number of cycles	62
Figure 3.2: Signal intensity for CPMG spectra of QmPES- $X_{6.7}Y_{3.4}$ and QrPES- $X_{0.67\text{N}}Y_{0.33\text{N}}$ as a function of the number of cycles	63
Figure 3.3: (a) Conductivity as a function of IEC, (b) conductivity as a function of water uptake, (c) water uptake as a function of IEC, and (d) $T_2$ as a function of IEC for the series of mPESs	65
Figure 3.4: Schematic diagram of ion/water transport in (a) mPES- $X_{6.7}Y_{2.5}$ (b) mPES- $X_{6.7}Y_{3.4}$ , and (c) mPES- $X_{6.7}Y_{7.7}$ or mPES- $X_{6.7}Y_{11.1}$ . Block dots, $\oplus$ , and cylinders represent water molecules, quaternary ammonium cations, and ion channels, respectively	66
Figure 3.5: Water uptake as a function of IEC, (b) conductivity as a function of IEC for the series of mFPESs	68
Figure 4.1: DSC thermograms of mFPESs containing different hydrophilic segment at the same hydrophobic segment	72
Figure 4.2: Conductivity as a function of $N_{\text{fre}} / N_{\text{non}}$ for mFPES membranes	74

Figure 5.1: Plot of diffusion coefficients as a function of temperature for obtaining the activation energy	79
Figure 5.2: Plot of intensity decay as a function of gradient strengths for determining diffusion coefficient of water in (a) bulk, (b) mFPES-X <sub>5.6</sub> Y <sub>14.7</sub> , (c) mFPES-X <sub>5.6</sub> Y <sub>9.7</sub> , and (d) mFPES-X <sub>5.6</sub> Y <sub>6.0</sub>	80
Figure 6.1: Synthetic scheme for selected poly (arylene ether)s as model materials	87
Figure 6.2: Stack of overlaid <sup>1</sup> H spectra of (a) the region of 1.7 ppm, (b) the region of 3.1 ppm, (c) the region of 4.5 ppm, and (d) the region of 7.5 ppm in QmPES-X <sub>6.7</sub> Y <sub>7.7</sub> under the standard test condition and corresponding degrading mechanisms	90
Figure 6.3: Log (relative intensity) plot of each peak in QmPES-X <sub>6.7</sub> Y <sub>7.7</sub> with respect to time at 60°C showing relative degradation rates	91
Figure 6.4: DOSY spectra (a) of QmPES-X <sub>6.7</sub> Y <sub>7.7</sub> DMSO-D <sub>6</sub> / MeOD-d <sub>3</sub> without KOH and (b) of QmPES-X <sub>6.7</sub> Y <sub>7.7</sub> DMSO-D <sub>6</sub> / MeOD-d <sub>3</sub> with KOH after 557 min at 60°C	92
Figure 6.5: Plot of remaining benzyltrimethyl ammonium groups in selected four samples (QmPES-X <sub>6.7</sub> Y <sub>7.7</sub> , QmFPES-X <sub>6.4</sub> Y <sub>4.7</sub> , PAE-Q, and PAE-N) as a function of time	94
Figure 6.6: DOSY spectra of initial and degraded (a) PAE-Q, (b) PAE-N, and (c) QmFPES-X <sub>6.4</sub> Y <sub>4.7</sub>	97
Figure 7.1: Selected anion conductive ionomer with different ion exchange group, trimethylamine and quinuclidinium (PAE-Q and PAE-N)	104
Figure 7.2: Voltage and power density curves for the hybrid fuel cells with trimethyl ammonium and quinuclidinium ionomers at the AEM cathode using 2M MeOH of and 50 sccm O <sub>2</sub> at 55°C, (a) methanol flow rate is 5 ml/min and (b) methanol flow rate is 0.6 ml/min	105
Figure 7.3: Voltage and power density curves for the hybrid fuel cells with quinuclidinium ionomers at the AEM cathode using 50 sccm O <sub>2</sub> and 2M methanol at 55°C of (a) different methanol flow rates. (b) Steady state performance of the cell at constant voltage of 250mV at different flow rate	107
Figure 7.4: Voltage and power density curves for the hybrid fuel cells with quinuclidinium ionomers at the AEM cathode using 2M MeOH and 50 sccm of different oxidants, O <sub>2</sub> and air at 55°C	108
Figure 7.5: Schematic diagram of the electrode structure created by (a) thin-film and (b) ionomer impregnation methods	109

Figure 7.6: Steady state performance of the cell created by the thin-film method and the ionomer impregnaion at constant voltage of 400mV	110
Figure 7.7: Polarization and power density curves for the hybrid fuel cells with selected multiblock copolymer ionomers at the AEM cathode using 2M MeOH and 50 sccm of O <sub>2</sub> at 55°C	111
Figure A.1: Syntheses cylindrical polymer brushes by ATRP from $\alpha$ -CD-PEG polyrotaxane macroinitiators	120
Figure A.2: DOSY spectra of (a) the polyrotaxane and (b) the polybrush. (C) shows the change of diffusion coefficients after MMA polymerization	122
Figure A.3: Comparison of (a) GPC trace and (b) A slice at 0.8 ppm in the DOSY spectrum of the polybrush	123

## LIST OF SCHEMES

	Page
Scheme 2.1: Synthesis of 3,3',4,4'-tetrafluorodiphenylsulfone (TFDBS)	37
Scheme 2.2: Synthesis of multiblock copoly(arylene ether sulfone), mPES- $X_{6.7}Y_{7.7}$ , where X = the number of repeat units in hydrophobic block, Y = the number of repeat units in block that ultimately becomes hydrophilic and n = the degree of polymerization in the final polymer	40
Scheme 2.3: Synthesis of the additional fluorinated multiblock copoly(arylene ether sulfone), mFPES- $X_{4.8}Y_{6.0}$ , where X = the number of repeat units in hydrophobic block, Y = the number of repeat units in block that ultimately becomes hydrophilic and n = the degree of polymerization in the final polymer	42

## LIST OF SYMBOLS AND ABBREVIATIONS

$[Q^+]$	actual quaternary ion content
$\Delta C_p$	the difference between specific heat capacity of liquid water and that of ice
$\Delta G_m$	Gibb's free energy of mixing
$\Delta H_m$	enthalpy of mixing
$\Delta S_m$	entropy of mixing
$\Delta T_f$	the freezing point depression
$\Delta T_m$	melting point depression
$\chi$	Flory-Huggin's interaction parameter
$\Phi$ (or $f$ )	volume fraction of polymer
AEMFC	Anion exchange membrane fuel cells
AFC	alkaline fuel cell
AFM	atomic force microscopy
BPA	bisphenol-A
C	ion concentration
CmFPES	chloromethylated mFPES
CMME	Chloromethyl methyl ether
CmPES	chloromethylated mPES
COSY	Homonuclear correlation spectroscopy
CPMG	Carr-Parcell-Meiboom-Gill
DC	the degrees of chloromethylation
DEPT	distortionless enhancement by polarization transfer
DFDPS	3,3',4,4'-tetrafluorodiphenylsulfone
$D_H^+$	diffusion coefficient of proton
DMAc	<i>N,N</i> -dimethylacetamide
TMAFC	direct methanol alkaline fuel cell
DMF	dimethyl foramide
DMSO	dimethyl sulfoxide
$D_O$	the diffusion coefficient at infinite temperature

$D_{\text{OH}^-}$	diffusion coefficient of hydroxide
DOSY	diffusion-ordered NMR spectroscopy
DSC	differential scanning calorimetry
$E_a$	the activation energy
F	Faraday's constant
FPS	4,4'-Difluorodiphenyl sulfone
FT-IR	fourier transform infrared spectroscopy
g	gradient fields strength
GDL	gas diffusion layer
GPC	gel permeation chromatography
$H_f$	enthalpy of freezing of water in the membrane
HFBP	4,4'-(hexafluoroisopropylidene) diphenol
$H_{\text{ice}}$	enthalpy of freezing water
HMBC	heteronuclear multiple bond correlation
HSQC	heteronuclear single quantum coherence
$I(g)$	observable NMR signal intensity
$I_0$	the echo intensity without applying a field gradient
IEC	ion exchange capacity
IPA	isopropanol
$M_{\text{fre}}$	the mass of the freezable water
$M_{\text{tot}}$	the total mass absorbed in the membrane
$M_0$	equilibrium magnetization value
MCFC	molten carbonate fuel cell
MEA	membrane electrode assembly
mFPES	difluorinated mPES
mPES	multiblock poly(arylene ether sulfone)s
$M_{xy}$	transverse magnetization
$M_z$	the z component of magnetization in non-equilibrium state
$N_{\text{fre}}$	the number of freezable water molecules
NIPAM	N-Isopropylacrylamide
NMR	nuclear magnetic resonance

$N_{\text{non}}$	the number of non-freezable water molecules
OCV	open circuit voltage
PAE-N	poly (arylene ether)s with quaternary ammoniums
PAE-Q	poly (arylene ether)s with quinuclidines
PAFC	phosphoric acid fuel cell
PEMFC	proton exchange membrane fuel cell
PFG	pulsed field gradient
PNC	polymer nanocomposite
PVA	poly (vinyl alcohol)

## SUMMARY

Anion exchange membrane fuel cells (AEMFCs) are an alternative to proton exchange membrane fuel cells (PEMFCs) with potential benefits that include low cost (i.e., platinum-free), facile electro-kinetics, low fuel crossover, and use of CO-resistant metal catalysts. Despite these advantages, AEMFCs have not been widely used because they require more highly conductive anion exchange membranes (AEMs) that do not exhibit impaired physical properties. Therefore, the issues that this research is dealing with are to maximize conductivity and to improve chemical stability. As model materials for these studies, I synthesize a series of multiblock copolymers with which polymer structures and morphologies can be easily controlled. Chapter 2 presents the synthesis and the chemical structure determination of the multiblock copolymers.

With the objective of maximizing conductivity, an understanding of the impact of structural features such as organization, size, polarity and connectivity of ionic domains and channels within AEMs on ion/water transporting properties is necessary for the targeted and predictable design of an enhanced material. Chapters 3 to 5 describe three characterization techniques that reveal the role of these structural features in the transport process. Specifically, Chapter 3 demonstrates the possibility that the NMR relaxation times of water could be an indicator of the efficiency of ion channels. Low-temperature DSC measurements differentiate the state of water (i.e., bound water and free water) inside the membranes by measuring freezing temperature drop and enthalpy. Chapter 4 demonstrates that the number of water molecules in each state correlates with conductivity and suggests a major anion-conducting mechanism for the multiblock AEM

systems. In Chapter 5, the measurement of the activation energy of diffusion characterizes ion transporting behavior that occurs on the sub-nanometer scale.

For the characterization of the chemical stability of the AEMs under high pH conditions, I employ automated  $^1\text{H}$  NMR measurements as a function of time as well as diffusion-ordered NMR spectroscopy (DOSY) as shown in Chapter 6. Finally, I demonstrate that new multiblock copolymers are successfully utilized as an ionomer for a hybrid cell in Chapter 7. The properties of the polymer strongly influence overall cell performance. I believe that the combination of the techniques presented in this thesis will provide insight into the ion/water transporting mechanism in a polymer ion conductor and guidance for improving conductivity and the chemical stability of the AEMs.

# CHAPTER 1

## INTRODUCTION

### 1.1. Fuel Cell

The demand for alternative and clean energy has been growing over the last decade because of severe climate issues, surging oil prices, and continually increasing energy consumption. Among devices that address these issues, fuel cells that convert the chemical energy from hydrogen gas as a fuel into electric energy in the presence of atmospheric oxygen by the redox reaction have drawn significant attentions because they can be an efficient pollution free energy source.<sup>1</sup> In addition, the fuel cell continuously operates as long as fuel and oxidant are supplied without recharging and running down unlike a battery, which can expand its applications. The fuel cell has also an advantage in terms of energy efficiency compared to Carnot engines because it operates in isothermal condition with less energy loss and less irreversible condition.

The performance of the fuel cell is determined by its polarization curve as shown in Figure 1.1. The polarization curve shows a direct current voltage delivered at electrodes as a function of current density. Because of polarization, the operating voltage of a fuel cell is always less than the open circuit voltage (OCV). The power output of the fuel cell (in  $\text{mWcm}^2$ ) is given by the product of voltage and current density. Typical polarization curves indicate that the maximum efficiency is achieved at the open circuit voltage condition and the potential value drops off as the current density increases. The key characteristics of this curve are as follows:

- 1) The open circuit voltage (OCV) is less than the theoretical maximum voltage mostly because of crossover of reactants and diffusion to the other electrodes.
- 2) A rapid initial voltage drop is caused by the slowness of reactions taking place on the surface of the electrodes.
- 3) The voltage then falls less rapidly and more linearly, which is proportional to the resistance to the flow of electrons through materials on the electrode and the resistance to ion conduction through the electrolyte.
- 4) A drastic voltage drop occurs at a higher current density because of the limitation of mass transfer.

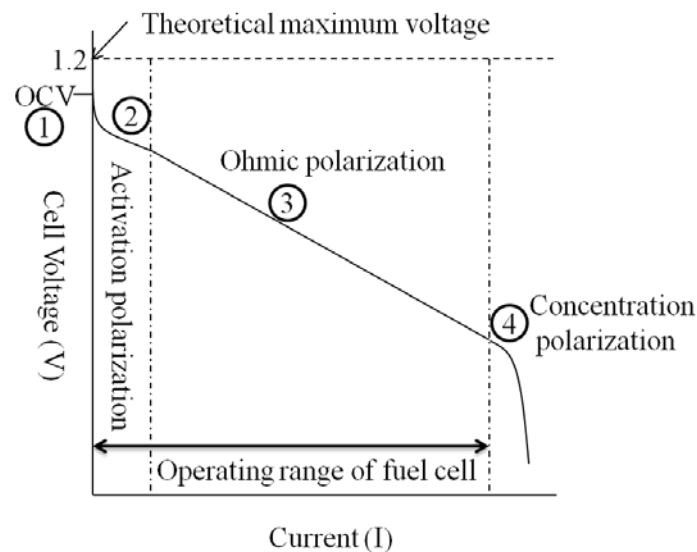


Figure 1.1. Typical polarization curve of a hydrogen/air polymer electrolyte membrane fuel cells

The fuel cell device is composed of mainly three components: an anode at which electrons produce by the fuel oxidizing, a cathode at which the oxidizing agent is reduced, and an electrolyte which is a barrier to separate reactants and the conductor of selective ions. Ion conduction through the electrolyte can occur in either direction, an anode to a cathode or a cathode to an anode, depending on the type of the fuel cell. The fuel cell can usually be classified by the ions which are transporting through the electrolyte. These

charge carriers include  $H^+$ ,  $OH^-$ ,  $CO_3^-$ ,  $O_2^-$ , etc.<sup>2</sup> Table 1.1 compares different types of fuel cells in terms of their applications, advantages, and disadvantages. Table 1.2 summarizes the types and the associated electrochemical reactions in corresponding fuel cells.

Table 1.1. Comparison of fuel cell technologies<sup>3</sup>

Fuel cell	Operating Temperature	Application	Advantages	Disadvantages
Proton exchange membrane (PEMFC)	50-100°C	<ul style="list-style-type: none"> <li>• Backup power</li> <li>• Portable power</li> <li>• Distributed generation</li> <li>• Transportation</li> <li>• Specialty vehicles</li> </ul>	<ul style="list-style-type: none"> <li>• Solid electrolyte reduces corrosion &amp; electrolyte management problems</li> <li>• Low temperature</li> <li>• Quick start-up</li> </ul>	<ul style="list-style-type: none"> <li>• Expensive catalysts</li> <li>• Sensitive to fuel impurities</li> <li>• Low temperature waste heat</li> </ul>
Alkaline (AFC)	90-100°C	<ul style="list-style-type: none"> <li>• Military</li> <li>• Space</li> </ul>	<ul style="list-style-type: none"> <li>• Cathode reaction faster in alkaline electrolyte, leads to high performance</li> <li>• Low cost components</li> </ul>	<ul style="list-style-type: none"> <li>• Sensitive to CO<sub>2</sub> in fuel and air</li> <li>• Electrolyte management</li> </ul>
Phosphoric acid (PAFC)	150-200°C	<ul style="list-style-type: none"> <li>• Distributed generation</li> </ul>	<ul style="list-style-type: none"> <li>• Higher temperature enables a combined heat and power (CHP)</li> <li>• Increased tolerance to fuel impurities</li> </ul>	<ul style="list-style-type: none"> <li>• Pt catalyst</li> <li>• Slow start-up</li> <li>• Low current and power</li> </ul>
Molten carbonate (MCFC)	600-700°C	<ul style="list-style-type: none"> <li>• Electric utility</li> <li>• Distributed generation</li> </ul>	<ul style="list-style-type: none"> <li>• High efficiency</li> <li>• Fuel flexibility</li> <li>• Can use a variety of catalysts</li> <li>• Suitable for CHP</li> </ul>	<ul style="list-style-type: none"> <li>• High temperature corrosion and breakdown of cell components</li> <li>• Slow start-up</li> <li>• Low power density</li> </ul>
Solid oxide (SOFC)	700-1000°C	<ul style="list-style-type: none"> <li>• Auxiliary power</li> <li>• Electric utility</li> <li>• Distributed generation</li> </ul>	<ul style="list-style-type: none"> <li>• High efficiency</li> <li>• Fuel flexibility</li> <li>• Can use a variety of catalysts</li> <li>• Solid electrolyte</li> <li>• Suitable for CHP and combined heat, hydrogen, and power (CHHP)</li> <li>• Hybrid/ gas turbin cycle</li> </ul>	<ul style="list-style-type: none"> <li>• High temperature corrosion and breakdown of cell components</li> <li>• High temperature operation requires long start up time and limits</li> </ul>

Table 1.2 Electrochemical reactions and charge carriers in fuel cells<sup>2</sup>

Fuel cell	Charge carriers	Anode reaction	Cathode reaction
Proton exchange membrane (PEMFC)	H <sup>+</sup>	H <sub>2</sub> → 2H <sup>+</sup> + 2e <sup>-</sup>	½ O <sub>2</sub> + 2H <sup>+</sup> + 2e <sup>-</sup> → H <sub>2</sub> O
Alkaline (AFC)	OH <sup>-</sup>	H <sub>2</sub> + 2OH <sup>-</sup> → 2H <sub>2</sub> O + 2e <sup>-</sup>	½ O <sub>2</sub> + H <sub>2</sub> O + 2e <sup>-</sup> → 2OH <sup>-</sup>
Phosphoric acid (PAFC)	H <sup>+</sup>	H <sub>2</sub> → 2H <sup>+</sup> + 2e <sup>-</sup>	½ O <sub>2</sub> + 2H <sup>+</sup> + 2e <sup>-</sup> → H <sub>2</sub> O
Molten carbonate (MCFC)	CO <sub>3</sub> <sup>2-</sup>	H <sub>2</sub> + CO <sub>3</sub> <sup>2-</sup> → H <sub>2</sub> O + CO <sub>2</sub> + 2e <sup>-</sup> CO + CO <sub>3</sub> <sup>2-</sup> → 2CO <sub>2</sub> + 2e <sup>-</sup>	½ O <sub>2</sub> + CO <sub>2</sub> + 2e <sup>-</sup> → CO <sub>3</sub> <sup>2-</sup>
Solid oxide (SOFC)	O <sup>2-</sup>	H <sub>2</sub> + O <sup>2-</sup> → H <sub>2</sub> O + 2e <sup>-</sup> CO + O <sup>2-</sup> → CO <sub>2</sub> + 2e <sup>-</sup> CH <sub>4</sub> + 4O <sup>2-</sup> → 2H <sub>2</sub> O + CO <sub>2</sub> + 8e <sup>-</sup>	½ O <sub>2</sub> + 2e <sup>-</sup> → O <sup>2-</sup>

Among the various kinds of fuel cells, my main focus of this research is the polymer electrolyte fuel cell including proton exchange membrane fuel cells and anion exchange membrane fuel cells. The operation mechanism and the comparison of these fuel cells will be discussed in order to clarify the issues that this research is dealing with.

## 1.2. Proton Exchange Membrane and Anion Exchange Membrane Fuel Cells

Proton exchange membrane fuel cells (PEMFCs) are composed of a solid polymer as an electrolyte and two electrodes containing a noble metal catalyst. At the anode, hydrogen gas ionizes to protons and electrons are released according to the following reaction.



At the cathode, oxygen reacts with electrons transferred from the anode and protons from electrolyte to produce water as follows.

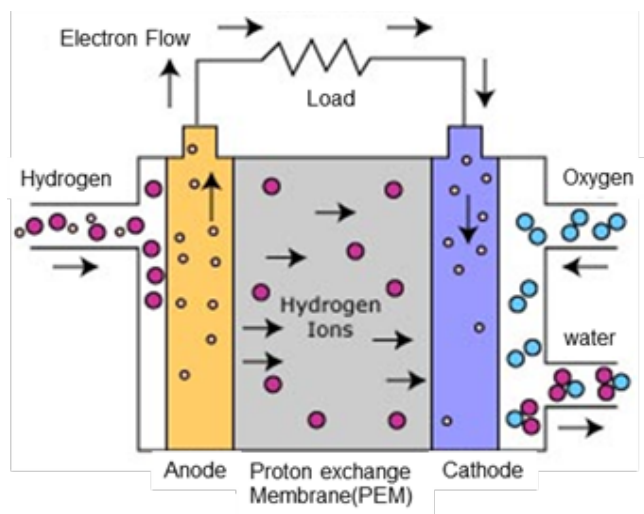


Figure 1.2. Schematic diagram of the proton exchange membrane fuel cell<sup>4</sup>

In PEMFCs, the most well-known and well-established electrolyte is Nafion<sup>®</sup>, developed by DuPont in 1962.<sup>5</sup> Nafion is a perfluoro-sulfonated copolymer that exhibits high ion conductivity and dimensional stability. Because of its superiority, Nafion is still the reference electrolyte against which other PEMs are judged. Despite the noble proton conductive electrolytes like Nafion, PEMFCs still have several obstacles that hinder commercialization. First of all, an expensive noble metal catalyst is necessary for maintaining high performance of fuel cells. In addition, water management in PEMFCs is inherently complicated because there are several contradictory water movements to, within, and from the electrolyte of a PEMFC.<sup>1</sup> Therefore, they require delicately maintained water balance between flooding and drying out. Another obstacle is catalyst poisoning by carbon monoxide contained in hydrogen gas stream, which leads to the slow reduction of oxygen at the cathode.

To address these problems of PEMFCs, I consider that anion exchange membrane fuel cells (AEMFCs) are the best candidate. At the cathode in AEMFCs, oxygen in air is reduced, producing hydroxide ions as follows,



These ions are transferred through the hydroxide conductive electrolyte to the anode at which the hydrogen is oxidized into water as follows,

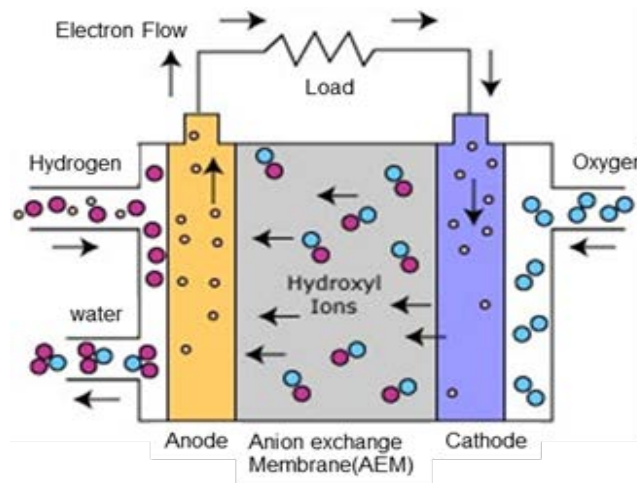
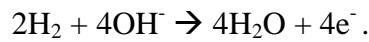


Figure 1.3. Schematic diagram of the anion exchange membrane fuel cell<sup>4</sup>

The first important advantage of AEMFCs is that the kinetics of the reduction of oxygen at the cathode is faster in an alkaline environment, so AEMFCs have a higher operating voltage than PEMFCs. As to the issue of cost, AEMFCs have a considerable advantage because the electrodes can be made of non-noble metal catalysts.<sup>6, 7</sup> In addition, the transport of hydroxide ions from the cathode to the anode, where fuel is provided, prevents a fuel crossover problem. The electro-osmotic drag associated with ion conduction resists the crossover of liquid fuel in AEMFCs, therefore allowing the use

of more concentrated liquid fuels.<sup>8</sup> Finally, water management is facilitated because of intrinsic balance between consumption at the cathode and generation at the anode. However, AEMFCs have a few drawbacks, one of which is a lower transport coefficient of a hydroxide anion than that of a proton ( $D_{H^+} = 9.31 \times 10^{-5}$ ,  $D_{OH^-} = 5.28 \times 10^{-5}$  cm<sup>2</sup>/sec in water at 25°C).<sup>9</sup> Consequently, it is thought that the conductivity of AEMs might not surpass the conductivity of PEMs under equivalent conditions. The inherently low diffusion coefficient of a hydroxide ion requires the AEM to have particularly high ion conductivity. As the AEMFCs operate under high pH, stability and durability issues also have to be carefully considered. All primary requirements of the AEM are listed as follows:

- High anion conductivity
- Chemical stability during manufacturing and operation, especially at high pH and operation temperature (~ 60°C)
- Proper water uptake and degree of swelling
- Barrier properties against hydrogen and oxygen
- Facile film formation
- Low cost

Above all the requirements, I believe that conductivity and chemical stability are the core properties to obtain high performance anion conductive membranes. Detail accounts about these two issues that this research is dealing with are following.

### 1.3. Conductivity Relating to Polymer Morphology

Appropriate interpretations of the ion-conducting behavior in AEMs can be initiated by the definition of conductivity and an understanding of the transport mechanisms for hydroxide conduction through the AEM. Generally, conductivity is proportional to ion concentration, the magnitude of its charge, and the mobility of charge carriers. Given the Faraday constant which is the proportionality factor relating ion conductivity to the ion concentration, the charge, and the mobility, ion conductivity is defined by the following equation (Equation 1.1),

$$\sigma = FC|Z|\mu \quad (1.1)$$

where,  $\sigma$  is conductivity of the ion,  $F$  is the Faraday's constant,  $C$  is the ion concentration,  $Z$  is the charge on the ion, and  $\mu$  is the mobility. Application of this definition to anion conducting system leads to Equation 1.2.<sup>10</sup>

$$\sigma_{OH^-} = F[Q^+]\mu'_{OH^-} \quad (1.2)$$

where,  $[Q^+]$  is actual quaternary ion content taking into account the degree of ion dissociation and  $\mu'_{OH^-}$  is the effective ion mobility. Equation 1.2 suggests that maximum conductivity can be achieved by the maximum ion content and the ion mobility.  $[Q^+]$  is a rather straightforward concept and relatively easy to evaluate from the ion exchange capacity (IEC), which can be determined by titration and  $^1H$  NMR. Unlike  $[Q^+]$ , effective ion mobility is more complicated and difficult to measure because it is affected by the channel size, tortuosity of ionic channels, and the geometrical proximity of ion carriers

and these are closely related to the polymer morphology, such as the degree of phase separation and the shape and size of the domains (i.e., channels).

To comprehend the transport mechanisms of hydroxide conduction, researchers tried to borrow the concept of proton conduction mechanisms through PEMs since dependencies of conductivity on relative humidity, temperature, and water uptake in the AEM system appear to be similar to those in the PEM system. Substantial experiments and simulations proposed that protons transport through the PEM according to the combination of several mechanisms including the Grotthuss mechanism, diffusion, convection, and surface site hopping along the ion exchange groups.<sup>11-13</sup> Figure 1.4 illustrates that listed transport mechanisms that might occur in an AEM. The anion transportation according to the Grotthuss mechanism is that hydroxide ions are moving through the formation and cleavage of hydrogen bonding network of water molecules (Figure 1.5).

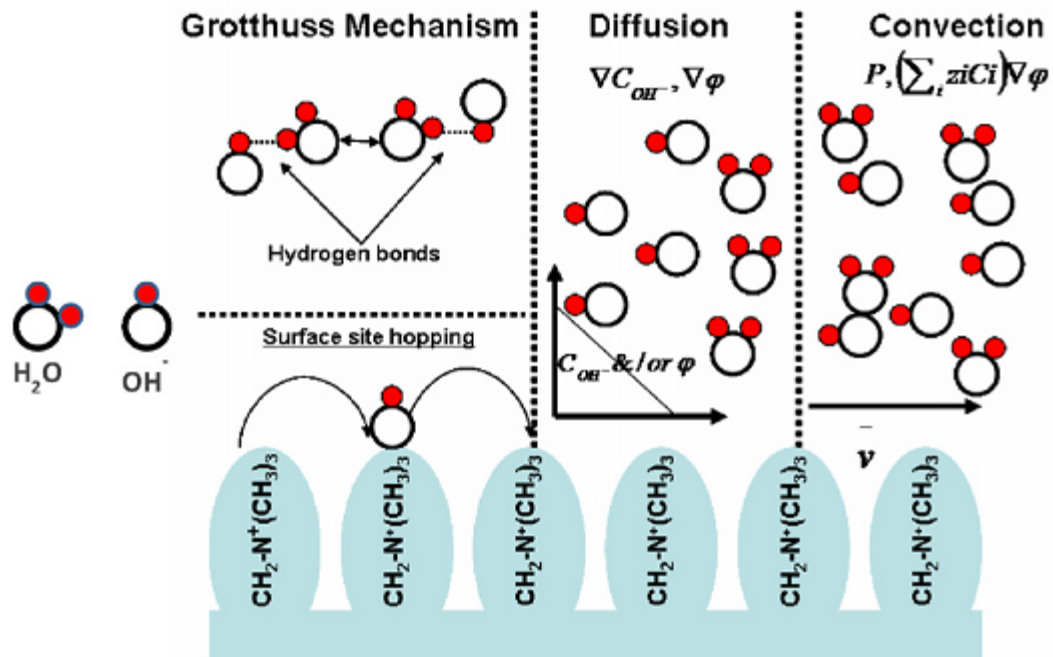


Figure 1.4. Possible dominant transport mechanisms for hydroxide in the anion exchange membrane, analog to those for proton transport.<sup>14</sup>

Diffusive transportation of anions can occur in the condition of concentration and/or electrical potential gradients. The anions can also convect across the membrane because anions drag the certain amount of water, which generates convective flow of water molecules in the membrane. Surface site hopping, as the name implied, is that transporting process to which ions hop from one quaternary ammonium group to the others.

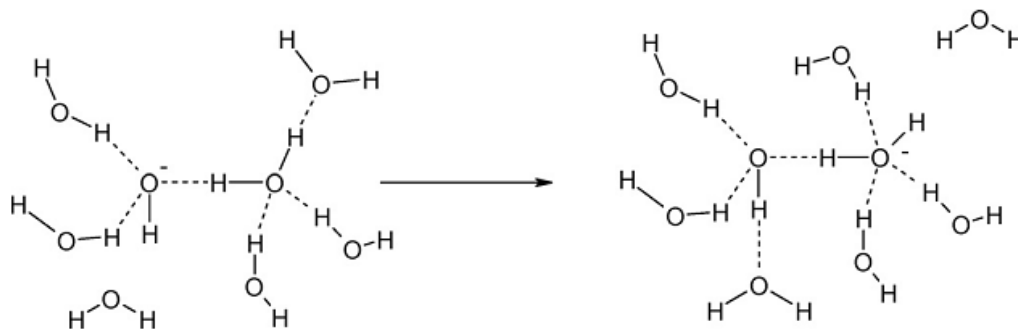


Figure 1.5. Transport mechanism of hydrated ions in aqueous solution<sup>15</sup>

Despite the reasonable assumption that the anion transport mechanism resembles the proton transport mechanism, significantly low conductivities of the AEMs compared to those of the PEMs have to be explained to design an efficient anion conducting membrane. As already mentioned, the transport coefficient of hydroxide ions is greater than that of protons, which can be attributed to the tendency that hydroxide anions have more stable and thus heavier solvation shells than hydronium ions. And, the low degree of anion dissociation caused by the weak basicity of quaternary ammonium groups associated with the lower ion mobility of hydroxide ions than that of proton (ion mobility in dilute solution of  $H^+ = 4.76$  and of  $OH^- = 2.69$  relative to  $K^+$ <sup>16</sup>) can hamper the facile anion conduction. Rapid conversion of hydroxides to carbonate ions by contacting with carbon dioxide in air could be detrimental to conducting performance. Summation of all penalties mentioned results in four times to twice lower hydroxide ion conductivity than proton conductivity at a similar IEC.

Considering plausible ion-conduction mechanisms and the comparison between a PEM and an AEM system, researchers have been attempted to improve conductivity through polymer morphology manipulation by which the efficient nanochannels for ion

transport might be created. Hibbs et al. compared the transport properties of water in hydroxide and proton conducting membranes.<sup>17</sup> They showed that water in an AEM is moving faster and is less bound within the polymer surface than it is in a PEM using self-diffusion coefficients and an enthalpy of melting. They attributed these observations to the different ion dissociation power of sulfonates for the PEM and quaternary ammoniums for the AEM. Since the sulfonate group in the PEM is considered to be a strong acid, the PEM yields more free ions, which require water molecules of hydration that may bind water more strongly than the relatively weak base in the AEM.

But they puzzled about the counterintuitive result of water permeability as a function of water binding. Water permeability for the AEM is greater than that for the PEM. Even though water in the AEM is more mobile and less bound, transport of water is slower. They attributed these curious observations to the degree of phase separation in the membrane. In other words, the PEM has a clearer phase separation and more organized ion channels than the AEM, which leads to higher conductivity and permeability. The transport is related to the water mobility in each case, but organized hydrated domains promote transport rates for a given degree of water binding. In summary, the membrane with high water mobility (i.e., high diffusion coefficients) will not necessarily improve conductivity, the organization of ion channels should be taken into account.

Numerous studies attributed Nafion's high conductivity to nanochannels generated through nanophase separation between a hydrophobic matrix and hydrophilic side groups. The initial model regarding the morphology of Nafion was suggested by Gierke in 1981 which claimed that a network of spherical water clusters is interconnected

by ~1 nm nanochannels.<sup>18</sup> Schmidt-Rohr and Chen<sup>19</sup> proposed a parallel water-channel model of Nafion which not only successfully explained outstanding proton conductivity and high water permeability but also expected the 10 times slower diffusion coefficient of water in Nafion containing 20 wt% water than in bulk water.

Attempts have been made to create proton conductivity in materials with Nafion-like morphology by incorporating monomers with perfluoroacid groups.<sup>20, 21</sup> Example alternative materials also include sulfonated poly(ether sulfone)s,<sup>22</sup> hydrophilic–hydrophobic multiblock copolymers based on poly(arylene ether sulfone),<sup>10, 23, 24</sup> and aromatic comb-shaped copolymers with highly sulfonated side chains.<sup>25</sup> Attempts have also been made to create materials with hydroxide conductivity using sequential hydrophobic and hydrophilic blocks. Tanaka et al. prepared anion-conductive multiblock copoly(arylene ether)s that had higher hydroxide ion conductivity than their corresponding random copolymers.<sup>26</sup> They attributed the enhanced conductivity of the multiblock copolymers to the well-developed phase-separated morphology of their polymers. Although the conductivity of AEM multiblock copolymers has been reported, the systematic study of water mobility in these types of polymer membranes has not been studied. An understanding of the relationships between polymer structure, water mobility, and ion conductivity is important to finding predictive pathways for improving conductivity.

#### **1.4. Previous Studies of Water Mobility in Fuel Cell Membranes**

Recently, researchers have achieved an advanced understanding of the transportation of protons and small molecules (e.g., water and/or alcohols as liquid fuel)

in sulfonated proton conductive polymer membranes (e.g., Nafion), which is related to polymer morphology or an ionic nanochannel structure. Although the detail morphological information is still under debate, the general agreement is that nano-phase separation between hydrophobic polymer backbone and hydrophilic ion exchange groups occurs under fully-hydrated conditions.<sup>27</sup> The developed nano-phase separation leads to nanochannels composed of the interconnected ionic network through which protons and hydrophilic small molecules transport. This general consensus proposed that an efficient phase separated morphology result in productive ion mobility, and thus improved conductivity. The design and development of the efficient ion-conducting polymer morphology require the accurate and intensive characterization techniques. In this section of the thesis, polymer morphology analysis using several characterization methods will be discussed.

#### **1.4.1 Imaging techniques**

The most popular and visualized morphology information can be obtained by the several imaging techniques including transmission electron microscopy (TEM) and atomic force microscopy (AFM). The imaging techniques are often employed to analyze the phase separation by showing ionic domains with different contrast. Watanabe's group took scanning TEM images of their anion conductive multiblock copolymers and random copolymers stained with tungstate ions.<sup>26</sup> The image of random copolymers showed a uniformly gray image, but multiblock copolymers exhibited dark ionic domains distributed in the entire image. They also estimated the size of spherical ion domains with widths of ~5 nm. TEM observations of the samples that are stained with lead ions and

cross-sectioned using a microtome used to reveal the interconnectivity of ionic clusters in densely sulfophenylated block copolymer membranes.<sup>28</sup> The TEM image showed dark and bright regions corresponding to the hydrophilic and hydrophobic domains, respectively and the hydrophilic domains were well-interconnected.

AFM is considered to be a more facile technique than TEM in terms of sample preparation for obtaining a similar type of morphological information. Takamuku and Jannasch obtained AFM images of their multiblock copolymers by tapping mode analysis of membrane surfaces to estimate the dependency of the domain size on the length of a unit block.<sup>29</sup> The AFM images of a series of multiblock copolymers showed that the size of the hydrophobic block length had a linear relationship to the size of hydrophobic phase domains. While imaging experiments provide valuable morphological data without complicated calculations and analysis, the information does not directly reflect the ion/water transport phenomenon or provide a quantitative metric for evaluating different materials. In addition, imaging techniques suffer from laborious and sometimes inconsistent sample preparation procedures. In contrast, NMR measurements enable direct characterization of local molecular dynamics and ion/water movement through domains inside membranes.

#### **1.4.2. NMR relaxation times**

NMR relaxation is the processes by which nuclear magnetization disturbed by pulses in a non-equilibrium state returns to equilibrium of the spin system. The equilibrium state implies that all coherences of spins are absent (i.e., there is no transverse ( $M_x$ ,  $M_y$ ) magnetization) and the net magnetization vector aligns along the

direction of the applied field ( $M_z = M_0$ ). This equilibrium state can be recovered through interaction of the spin system with a molecular environment. Relaxation processes may be divided into two types. Spin-lattice ( $T_1$ ) relaxation involves redistributing the populations of the nuclear spin states to Boltzmann distribution values. In other words,  $T_1$  is the time constant for the recovery of the z component of magnetization in non-equilibrium state ( $M_z$ ) from  $M_z = 0$  to the equilibrium magnetization value ( $M_0$ ) as explained in Equation 1.3.

$$M_z = M_0(1 - e^{-\frac{t}{T_1}}) \quad (1.3)$$

Spin-spin ( $T_2$ ) relaxation involves the decay of coherences.  $T_2$  is the time constant for recovery to equilibrium of the transverse magnetization ( $M_{xy}$ ) as explained in Equation 1.4.

$$M_{xy} = M_{xy,0} e^{-\frac{t}{T_2}} \quad (1.4)$$

Considering relaxation process is caused by magnetization fluctuation and the primary source of the magnetization fluctuation is molecular motion, researchers have used relaxation time data to correlate with mobility of molecules. Specifically, NMR spin-lattice ( $T_1$ ) and spin-spin ( $T_2$ ) relaxation times provide direct indications of the restricted motions of water in confined environments or near surfaces. The spin-lattice NMR relaxation time ( $T_1$ ) has been used to examine water confinement and physical interactions of water molecules with the polymer in Nafion.<sup>30</sup> Sierra-Martin et al. measured  $T_2$  to detect motional confinement of water molecules in a poly(NIPAM) microgel.<sup>31</sup> They found that  $T_2$  could be correlated with changes in water mobility and degree of confinement. Morphological differences between random and multiblock

copolymers in PEMs were revealed by analyzing bound versus free water through  $T_2$  values (water associated to sulfonic acid groups relaxed faster).<sup>23</sup>

### **1.4.3 Differential scanning calorimetry**

As I already discussed, ion transport is governed by the combination of various ion transporting mechanisms. The state of water such as bound water and free water is one of the key factors impacting ion transporting mechanisms because the proximity of water to ion-exchange groups or polymer materials alters the dynamics of water (Figure 1.6). So, distinction of various states of water inside hydrophilic ion cluster and determination of the amounts of each state of water is essential for explicit understanding of ion transport behaviors. In a real PEM system at ambient temperature, enormously rapid proton-exchange in acidic water makes difficult to discern the states of water, as illustrated by the single broad peak in the  $^1\text{H}$  spectrum of hydrated membranes.<sup>32</sup> However, differential scanning calorimetry (DSC) measurements at a low temperature where water inside the membranes can freeze enable quantifying and corroborating the existence of two types of water (i.e., freezable water and non-freezable water) by the value of freezing temperature drop and freezing enthalpy. Non-freezable water is defined as the water that is strongly associated with the ion groups or the polymer matrix, so that they are not able to crystallize. Non-freezable water yields no heat flow in DSC. By contrast, freezable water that is only weakly polarized exhibits similar thermal transitions to bulk water. This water produces the exothermic peak at lower temperature than  $0^\circ\text{C}$  in a cooling scan and the area of the peak provides the clue of estimating the amount of freezable water in membranes.

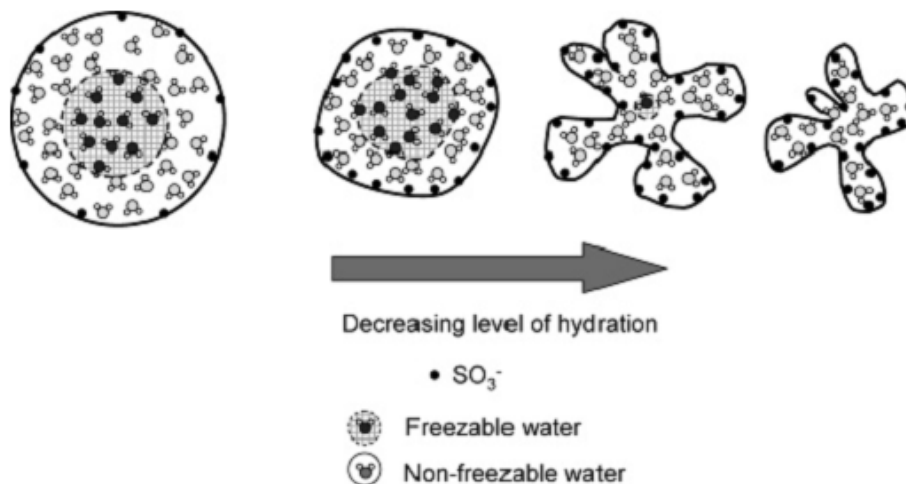


Figure 1.6. Schematic diagram illustrating the different types of water in the hydrophilic pore of a membrane; Reducing the humidity reduces the amount of freezable water present in the pore and alters its size.<sup>32</sup>

Several attempts have been made to investigate the water dynamics and ion-transportation in ion-conducting membranes using this DSC technique. The low-temperature proton conduction in Nafion was studied by Thompson et al.<sup>33</sup> and Nicotera et al.<sup>30</sup> The Holdcroft group addressed the nature of water inside the polymer membrane influenced by temperature and humidity. They also tried to correlate the DSC data with proton conductivity at subzero temperatures and low humidity conditions.<sup>32</sup> DSC analyses along with dynamic vapor sorption were employed to investigate water mobility in Nafion/zeolite composite membranes.<sup>34</sup>

## 1.5. Stability of Anion Conductive Membrane at High pH and Temperature

Another concern with AEMFCs along with inherently low anion conductivity is the stability of the membranes at high pH. The chemical durability of AEMs is necessary for the sustainability of high hydroxide ion conductivity and mechanical properties at elevated temperatures for the life time of fuel cell devices. Among the numerous AEMs developed for the fuel cell applications, early and still popular studies have focused on the use of quaternary ammonium cation groups,  $[\text{NR}_4]^+$ , which are tethered to a polymer backbone. Unfortunately, quaternary ammonium groups are prone to degrade by several reaction routes with hydroxide ions such as 1) Hofmann elimination, 2) nucleophilic substitutions, and 3) ylide formation (Figure 1.7).<sup>9</sup> Hofmann elimination is initiated by the attack of hydroxide to the  $\beta$ -hydrogen atom of a carbon, which results in the elimination of a tertiary amine,  $[\text{NMe}_3]$ , along with the formation of an alkene group. Nucleophilic substitutions cause the cleavage of a carbon-nitrogen bond or the conversion of quaternary ammonium to tertiary ammonium by the attack of hydroxide to an  $\alpha$ -carbon atom. Finally, the degradation through ylide formation indicates that hydroxide can attack the proton of a methyl group of a quaternary ammonium cation, which produces water and ylide intermediates.

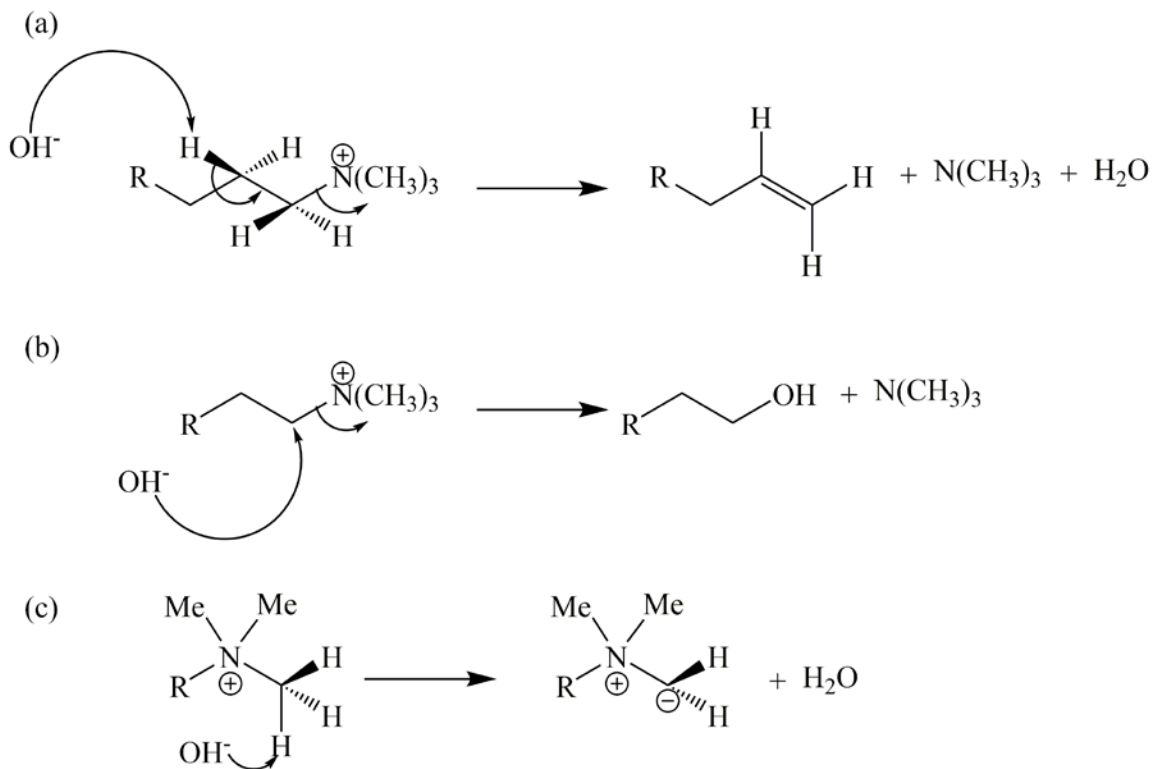


Figure 1.7. Various degradation routes for anion conductive membrane containing quaternary ammonium groups: (a) Hofmann elimination, (b) nucleophilic substitution, and (c) ylide formation

Researchers started to turn their attention to different cation species to address the chemical stability issues of the quaternary ammonium group. The Coates group synthesized phosphonium-functionalized polyethylene and evaluated the base stability of their polymers compared to quaternary ammonium-functionalized polymers.<sup>35</sup> They claimed that the tetrakis-(dialkylamino)phosphonium cation is almost immune to 15 M KOH at 22°C and 1 M KOH at 80°C when the benzyltrimethylammonium cation is significantly degraded at the same conditions. The new synthetic approach to a stable hydroxide-conductive membrane based on benzimidazolium hydroxide in which there is no ion-exchange group tethered to a polymer backbone had been attempted.<sup>36</sup> This

polymer was thought to be inherently stable against the attack of hydroxide ions because the reactive C2 positions in the bezimidazole unit were sterically crowded.

In addition to cation stability, polymer backbone stability has to be taken into account to improve AEMFC performance since the loss of mechanical toughness of anion conductive polymer membranes could cause drastic failure of the cell operation. Among a wide range of polymer architectures, polyaromatics such as poly(arylene ether)s and poly(phenylene)s have been primary candidates for AEMFC applications since their backbones are considered to be thermo-oxidatively and chemically stable. However, a few results are also reported that quaternized polyaromatics under certain alkaline conditions at an elevated temperature undergo a breakage of backbone linkages. For example, aryl-ether linkages in benzyltrimethylammonium functionalized poly(aryl ether)s are disconnected under high pH environments, as proposed in Figure 1.8.<sup>37</sup> The further investigation to elucidate the mechanism of backbone degradation and relationship to mechanical properties and ion conductivity is required to develop durable and robust anion conductive polymer membranes.

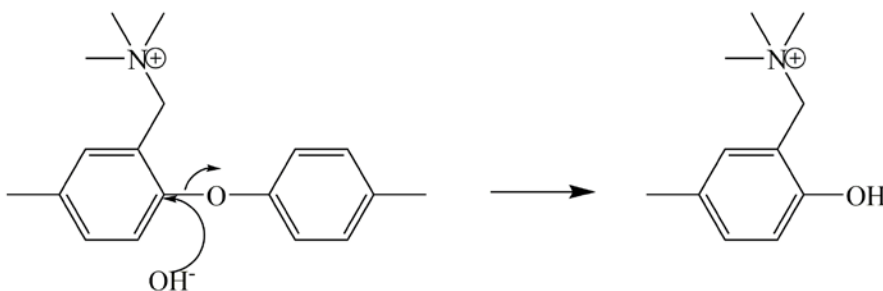
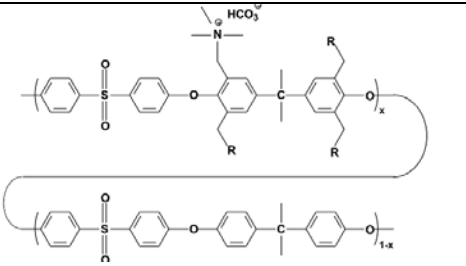
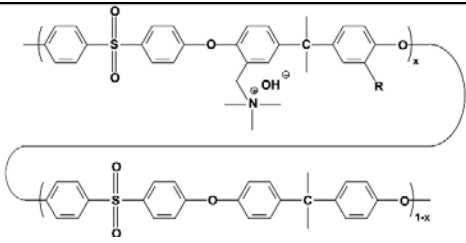
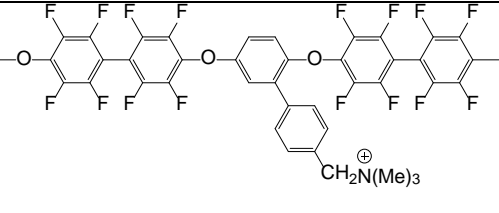
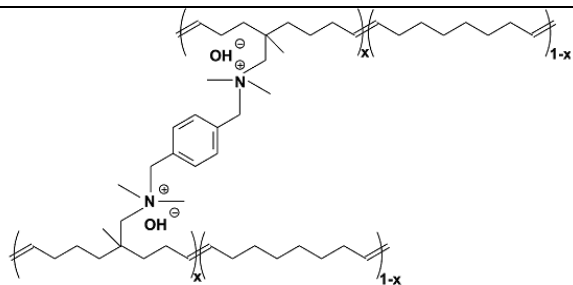
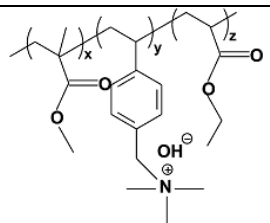
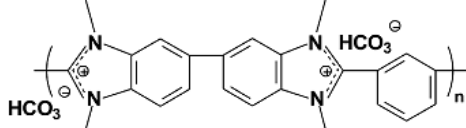


Figure 1.8. Proposed aryl-ether cleavage of benzyltrimethylammonium-functionalized poly(aryl ether)s under high pH environments.

## **1.6. Research Objectives and Strategies**

In this research, I aim at creating enhanced AEM materials that meet as many requirements as possible that I already discussed. Among all requirements, this research is focusing on two properties, conductivity and chemical stability, which are major determinants to operation of alkaline fuel cells incorporated with the new anion conductive polymers. Numerous studies have already been made to address the same issues as summarized in Table 1.3. Generally, iterative or random trials turn out to be unproductive and do not provide meanings that can lead to predictive approaches for improving the properties. So, a more desirable way would be a systematic study using model materials that is carefully controlled by limited factors. This systematic study might suggest the structure-property relationships for these materials to design a noble AEM. Performance of this study requires an appropriate model material and characterization methods.

Table 1.3. Representative examples of AEMs for the alkaline fuel cell

AEM Chemical structure	References
 <p>The structure shows a polymer backbone with a sulfonate group (-SO<sub>3</sub><sup>-</sup>) and a quaternary ammonium cation (-N<sup>+</sup>(Me)<sub>3</sub>). The counterion is a bicarbonate ion (HCO<sub>3</sub><sup>-</sup>). The backbone consists of a sulfonated aromatic ring and a methacrylate-like ring with substituents R.</p>	<p>Hickner et. al., 2010<sup>38</sup></p>
 <p>The structure is similar to the first one, but the counterion is a hydroxide ion (OH<sup>-</sup>).</p>	<p>Kohl et. al., 2010<sup>39</sup></p>
 <p>The structure features a perfluorinated aromatic backbone with a quaternary ammonium cation (-N<sup>+</sup>(Me)<sub>3</sub>) and a trimethylammonium counterion (CH<sub>2</sub>N<sup>+</sup>(Me)<sub>3</sub>).</p>	<p>Kohl et. al., 2011<sup>40</sup></p>
 <p>The structure shows a poly(ethylene glycol) backbone with a quaternary ammonium cation (-N<sup>+</sup>(Me)<sub>3</sub>) and a hydroxide counterion (OH<sup>-</sup>).</p>	<p>Coates et al., 2010<sup>41</sup></p>
 <p>The structure shows a poly(ethylene glycol) backbone with a quaternary ammonium cation (-N<sup>+</sup>(Me)<sub>3</sub>) and a hydroxide counterion (OH<sup>-</sup>).</p>	<p>Chu et al., 2010<sup>42</sup></p>
 <p>The structure shows a poly(2,6-pyridinediyl) backbone with a quaternary ammonium cation (-N<sup>+</sup>(Me)<sub>3</sub>) and a bicarbonate counterion (HCO<sub>3</sub><sup>-</sup>).</p>	<p>Holdcroft et al., 2011<sup>43</sup></p>

### 1.6.1 Multiblock copolymers for a model material

I used multiblock copolymers as a model material since the polymer morphology of these materials can be easily modified by the segment lengths and ion contents. Because of these reasons, block copolymers and multiblock copolymers were utilized to study the relationship between polymer morphology and proton conductivity. Bae et al. synthesized poly(arylene ether sulfone ketone) multiblock copolymer membranes having hydrophilic blocks that are highly sulfonated on bis(4-hydroxyphenyl)fluorine groups.<sup>44</sup> They found out that the multiblock copolymers have well-interconnected rodlike hydrophilic aggregates in their STEM images, which result in high proton conductivity even at low humidity. The Na group<sup>45</sup> and the Zhang group<sup>46</sup> prepared block sulfonated poly(arylene ether ketone) copolymers and investigated morphological characteristics using TEM and small angle X-ray scattering. But, the systematic research of hydroxide ion mobility and conductivity in AEMs has not been appeared. Even though Watanebe et al. measured scanning transmission electron microscope (STEM) to explain the enhanced conducting performance of multiblock AEMs, their results could not reveal ion mobility correlating with different block lengths or ion concentrations.<sup>26</sup> A series of multiblock copoly(arylene ether sulfone)s were synthesized with different block lengths and ion exchange capacities in this thesis to explore the ion transport behavior relating to different block lengths or ion contents. The detail synthesis procedure will be presented in Chapter 2.

### **1.6.2 Characterization techniques of water transport in the membranes**

I mainly employed two techniques to interpret the conductivity results of synthesized multiblock copolymers; NMR relaxation times and low-temperature DSC. Since both techniques directly characterize ion/water in the membranes instead of polymer materials, they can deliver more realistic and the accurate understanding of transport characteristics. The NMR relaxation time is the NMR observable that can reflect the degree of confinement for hydrophilic domains by which efficiency of the ion/water pathway could be judged. The measurement method of NMR relaxation times will be discussed in Chapter 3. The low-temperature DSC technique determines the amount of free water that is behaving like bulk water and bound water that is located close to ion groups due to the strong interaction with ion groups in the polymers. The DSC results along with the activation energy of diffusion expand the understanding of the ion transport mechanism that is dominated in new AEM systems and the number of water molecules that is needed to hydrate. The detail account about these experiments will be delivered in Chapters 4 and 5.

### **1.6.3 Quantitative chemical stability test for anion conductive multiblock copolymers and fluorinated poly(aryl ether)s having different ion exchange groups**

I compared the base stability of two sets of material; multiblock copolymers and fluorinated poly(aryl ether)s with different ion exchange groups. The methodology used for these comparisons is *in-situ*  $^1\text{H}$  NMR measurement under basic condition (high pH) at an elevated temperature. This technique provides not only quantitative chemical stability of the samples but also the detail mechanism of degradation relating to the characteristics of individual moieties of the polymers. Diffusion ordered spectroscopy (DOSY), the two

dimensional NMR spectrum presenting diffusion coefficients of each proton in the samples, supports the analyzing the degree of degradation by detecting the changes of diffusion coefficients as the degradation proceeded. The detail experimental procedures and discussions will be following in Chapter 6.

#### **1.6.4 Usage of multiblock copolymers and poly aryl(ether)s for alkaline fuel cells**

I tried to use anion conductive multiblock copolymers and fluorinated poly aryl(ether)s for alkaline fuel cell applications. An anion conducting polymer, which is used as a membrane and an ionomer for alkaline fuel cells, is a key element to govern device performance. For the systematic study on relationship between polymer properties and cell performance, the main resistances in alkaline fuel cells caused by polymer materials in the alkaline fuel cells must be defined as indicated in Figure 1.9 <sup>47</sup>: 1) an inhibition of the oxygen diffusion by the blockage of pores between agglomerated catalyst-supported carbon particles (i.e., secondary pores) 2) a resistance to oxygen permeation from the secondary pores to a reaction site through the ionomer layer, and 3) a limitation of anion conductivity. Chapter 7 will discuss the cell performance based on the different polymer properties and clarifying the dominating factors to determine cell performance. The major concerns of this research among the several types of alkaline fuel cells is a direct methanol hydrid fuel cell, where a high pH AEM cathode, a low pH PEM anode, and a PEM membrane are combined.

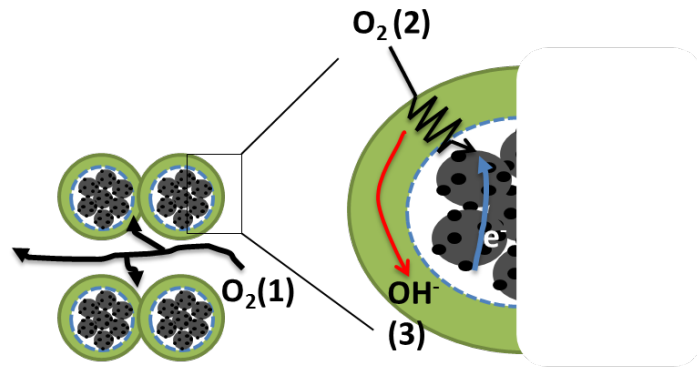


Figure 1.9. An illustration of the main resistances in alkaline fuel cells: (1) an inhibition of the oxygen diffusion by the blocking of secondary pores, (2) resistance to oxygen permeation from the secondary pores to a reaction site through the ionomer layers, and (3) a limitation of anion conductivity (modified from ref.<sup>47</sup>)

## CHAPTER 2

# SYNTHESIS AND CHEMICAL STRUCTURE DETERMINATION OF MULTIBLOCK COPOLYMERS

### 2.1. Introduction and Objectives

A series of anion-conductive multiblock copoly(arylene ether sulfone)s containing quaternary ammonium groups were synthesized through nucleophilic substitution polycondensation followed by chloromethylation and quaternization. A common way to polymerize dihalide aromatic sulfone with aromatic dihydroxide by making sequential ether linkages is nucleophilic aromatic substitution since molecular weights can be optimized by the reaction conditions such as the feed ratio of each monomer, reaction temperature, and polymerization time. Controlling the lengths of each segment in the multiblock copolymers enabled creating nanophase-separated morphologies. The corresponding random copolymers were also synthesized for the exact comparison with respect to the degree of randomness. Introducing additional fluorine groups to the hydrophobic segments was attempted to lead to more distinct nanophase separation. The comparison of the two sets of multiblock copolymers enabled discussing how the difference between the polarity of a hydrophobic block and that of a hydrophilic block affects polymer morphology, conductivity, and water mobility. The precise chemical structures of the copolymers were characterized using one-dimension spectra including  $^1\text{H}$ ,  $^{13}\text{C}$ , and distortionless enhancement by polarization transfer (DEPT) and two-

dimensional NMR including heteronuclear multiple bond correlation (HMBC) and heteronuclear single quantum coherence spectroscopy (HSQC). Gel permeation chromatography (GPC) was employed to ensure successful polymerization. Visual morphology information of synthesized multiblock copolymers was obtained by AFM.

## 2.2. Experimental Details

### 2.2.1. Materials

4,4'-Difluorodiphenyl sulfone (FPS), bisphenol-A (BPA), 1,1,2,2-tetrachloro ethane (TCE), trimethyl amine aqueous solution (50 wt%), and calcium hydride (CaH<sub>2</sub>) were obtained from TCI Co., Ltd. *N,N*-dimethylacetamide (DMAc), 4,4'-(hexafluoroisopropylidene) diphenol (HFBPA), tin(IV) chloride (SnCl<sub>4</sub>), 1,2-difluorobenzene (DFB), chlorosulfonic acid, and aluminum chloride (AlCl<sub>3</sub>) were obtained from Alfa Aesar. Chloromethyl methyl ether (CMME), potassium carbonate (K<sub>2</sub>CO<sub>3</sub>), and dimethyl sulfoxide-*d*<sub>6</sub> (DMSO-*d*<sub>6</sub>) were obtained from Aldrich Chemical. Chloroform-*d* was obtained from Cambridge Isotopes Inc. for NMR studies. All chemicals were used as received, unless otherwise specified.

### 2.2.2. Synthesis of monomer, 3,3',4,4'-tetrafluorodiphenylsulfone (TFDPS)<sup>47</sup>

1,2-Difluoro-benzene (10.3 g, 0.09 mol) was added to chlorosulfonic acid (33.7 g, 0.250 mol) slowly at 0 °C. The resulting solution was stirred at 80°C for 1 h and was poured into crushed ice. The product was extracted with dichloromethane (2x 30 mL). The organic extracts were combined, washed with distilled water, dried over anhydrous

magnesium sulfate, and filtered, and the solvent was removed. Purification by distillation in vacuum yielded 3,4-difluorobenzene-1-sulfonyl chloride as a pale yellow liquid.

3,4-difluorobenzene-1-sulfonyl chloride (5.02 g, 23.6 mmol) and 1,2-difluorobenzene (10.8 g, 94.4 mmol) were placed in a 100ml round bottom flask. Then, about 1 equiv. of  $\text{AlCl}_3$  was introduced into the well-stirred mixture at 80 °C. Immediately, hydrogen chloride began to evolve rapidly. The solution was heated to 100 °C and maintained at this temperature for 8 h. The dark reaction solution was then cooled to room temperature and poured into crushed ice with stirring. The brownish precipitate was collected by filtration and washed with a lot of water until the filtrate was neutral. The dried crude product was then recrystallized from ethanol twice to produce 3,3,4,4-tetrafluorodiphenylsulfone as white crystals.

### **2.2.3. Multiblock copolymerization (I)**

A typical procedure for the synthesis of hydroxy-terminated oligomer (for the number of repeat units,  $X = 6.7$ ) is as follows. DMAc was dried by distillation *in vacuo* at 130 °C over  $\text{CaH}_2$  and stored with activated 3A molecular sieves. FPS (1.63 g, 6.40 mmol), HFBPA (2.37 g, 7.04 mmol),  $\text{K}_2\text{CO}_3$  (2.21 g, 16.00 mmol), and DMAc (20 ml) were mixed under dry nitrogen in a dry 100-ml two-neck round-bottomed flask equipped with a condenser at room temperature for 10 min. The resulting mixture was heated at 120 °C using an oil bath for 3.5 h. HFBPA (0.79 g) was added to the mixture and allowed to react for 1 h at 120 °C to ensure that the ends were hydroxyl terminated. The slightly viscous mixture was poured into hot water to precipitate the product. The reddish powder was washed with water and methanol several times. The product was collected, isolated

by filtration, and dried at 80 °C for 24 h. The number of repeat units ( $X = 6.7$ ) and molecular weight ( $MW = 4040$  g/mol) were determined by  $^1\text{H}$  NMR.

A similar synthesis, purification, drying, and  $^1\text{H}$  NMR characterization procedure were followed to prepare a fluoro-terminated oligomer (number of repeat units,  $Y = 7.7$ ). FPS (1.79 g, 7.04 mmol), BPA (1.46 g, 6.40 mmol), and  $\text{K}_2\text{CO}_3$  (1.86 g, 12.80 mmol) were dissolved in 20 ml dry DMAc and stirred at 110 °C for 7 h. After addition of 0.27 g of FPS, the reaction was allowed to continue at 110 °C for 1 h, which finally yielded a white powder ( $Y = 7.7$ ,  $MW = 3660$  g/mol).

Copolymerization of the two oligomers was carried out to yield the multiblock copolymer, mPES- $X_{6.7}Y_{7.7}$ . The hydroxy-terminated oligomer (0.70 g, 0.17 mmol) was stirred with the fluoro-terminated oligomer (0.63 g, 0.17 mmol),  $\text{K}_2\text{CO}_3$  (0.24 g, 1.70 mmol), and DMAc (7.8 ml) at 130 °C for 2 h under nitrogen. This yielded a white product with molecular weight ( $M_n \sim 22.9$  kg/mol) and degree of polymerization ( $N \sim 3.9$ ) as measured by gel permeation chromatography (GPC). I also synthesized the random copolymer (rPES- $X_{0.5N}Y_{0.5N}$ ) through the polymerization of FPS (1.11 g, 4.38 mmol), HFBPA (0.74 g, 2.19 mmol), and BPA (0.50 g, 2.19 mmol) in the presence of DMAc (10 ml) and  $\text{K}_2\text{CO}_3$  (1.51 g, 10.9 mmol) at 130 °C for 4 h. The post-reaction workup and GPC characterization were the same as those described for the oligomerization.

#### **2.2.4. Multiblock copolymerization (II)**

The similar oligomerization procedures were utilized for the additional fluorinated multiblock copolymerization. For a fluoro-terminated oligomer (the number

of repeat units,  $X = 4.8$ ), TFDPS (2.04 g, 7.04 mmol), HFBPA (2.15 g, 6.40 mmol), and  $K_2CO_3$  (2.21 g, 16.00 mmol) were dissolved in 20 ml dry DMAc and stirred at 130 °C for 1.5 h. After addition of TFDPS (0.41g), the reaction was allowed to continue at 130 °C for 30 min, which finally yielded a white powder ( $X = 4.8$ , MW = 4094 g/mol). For a hydroxide-terminated oligomer (number of  $Y = 6.0$ ), FPS (1.63 g, 6.4 mmol), BPA (1.61 g, 7.04 mmol), and  $K_2CO_3$  (1.86 g, 12.80 mmol) were dissolved in 20 ml dry DMAc and stirred at 130 °C for 3 h. After addition of 0.54 g of BPA, the reaction was allowed to continue at 130 °C for 45 min, which finally yielded a white powder ( $Y = 6.0$ , MW = 2414 g/mol).

Copolymerization of the two oligomers was carried out to yield the additional fluorinated multiblock copolymer, mFPES- $X_{4.8}Y_{6.0}$ . The hydroxy-terminated oligomer (0.32 g, 0.101 mmol) was stirred with the fluoro-terminated oligomer (0.35 g, 0.106 mmol),  $K_2CO_3$  (0.14 g, 1.01 mmol), and DMAc (5.1 ml, 13 wt% of monomers) at 90 °C for 1.5 h under nitrogen. This yielded a white product with molecular weight ( $M_n \sim 31.2$  kg/mol) and the degree of polymerization ( $N \sim 4.8$ ) as measured by gel permeation chromatography (GPC). I also synthesized the random copolymer (rFPES- $X_{0.5N}Y_{0.5N}$ ) through the polymerization of DFDPS (1.09 g, 3.75 mmol), HFBPA (0.63 g, 1.87 mmol), and BPA (0.43 g, 1.87 mmol) in the presence of DMAc (6.3 ml) and  $K_2CO_3$  (1.29 g, 9.35 mmol) at 110 °C for 5 h. The post-reaction workup and GPC characterization were the same as those described for the multiblock copolymerization.

### 2.2.5. Chloromethylation, quaternization, and membrane casting

TCE was dried and stored over activated 3A molecular sieves. Dry TCE (5 ml) was added to mPES- $X_{6.7}Y_{7.7}$  or mFPES- $X_{4.8}Y_{6.0}$  (0.50 g). CMME (0.15 ml) and  $\text{SnCl}_4$  (0.01 ml) were then injected into the solution (Caution: chloromethyl methylether is carcinogenic and potentially harmful to human health). The reaction was allowed to continue for 4 h at 55°C. The crude chloromethylated polymer was recovered by pouring the reaction mixture into methanol and washing the precipitate with methanol several times.

The chloromethylated copolymers (CmPES or CmFPES) (0.50 g) were quaternized by adding 10 ml of 50 wt% trimethylamine aqueous solution to the copolymer at room temperature for 24 h. The dry quaternized copolymer (QPES) was recovered by evaporating the residual trimethylamine in a Petri dish. The QPES (0.50 g) was dissolved in DMF (3 ml) and the resulting solution was filtered through a 0.45  $\mu\text{m}$  PTFE membrane filter. A film was cast by pouring this solution into an aluminum dish followed by drying in a vacuum oven at 80°C for 24 h. The free-standing polymer films were about 100- $\mu\text{m}$  thick and 3.5  $\times$  3.5 cm. The chloride ions in the film were exchanged for hydroxide ions by soaking in 0.1 N KOH under nitrogen for about 12 h. After washing several times with water, the QPES membranes in hydroxide form were stored in distilled water in a closed vial.

### 2.2.6. Measurements

The chemical structures of the synthesized polymers were analyzed using a variety of NMR techniques: one-dimensional  $^1\text{H}$  and  $^{13}\text{C}$  NMR, DEPT, HSQC, and

HMBC. A Bruker Avance III 400 spectrometer with 5-mm sample tubes was used. Chloroform-*d* or DMSO-*d*<sub>6</sub> were used as NMR solvents. <sup>1</sup>H spectra (16 scans) were collected at 400.13 MHz with a 7.5 s recycle delay. The ion exchange capacities (IEC) and the degrees of chloromethylation (DC) were determined from the respective <sup>1</sup>H NMR spectra. The <sup>13</sup>C NMR spectra were collected at 100.61 MHz. The HSQC analysis was carried out using the Bruker pulse sequence, hsqcetgpsi, for 16 scans, 128 increments along t<sub>1</sub>, 1,024 data points along t<sub>2</sub>, and 160 Hz as a coupling constant. The HMBC analysis used the Bruker pulse sequence, hmbcgplpndqf, for 32 scans, 128 increments along t<sub>1</sub>, 1,024 data points along t<sub>2</sub>, 160 Hz as a one-bond coupling constant, and 10 Hz as a long-range coupling constant. The Bruker pulse sequence, deptsp135, was used for the DEPT-135 experiment.

The molecular weights of the polymers were determined by GPC using a Waters 2690 separations module and a 2410 differential refractive index detector, which was connected to Waters Styragel columns (HP 1, HP 3, HP 4). THF was used as the eluent and the solvent. The molecular weights were computed by a calibration curve based on polystyrene standards.

The water uptake of the membranes was evaluated according to equation 2.1:

$$\text{Water uptake} = \frac{W_w - W_d}{W_d} \times 100, \quad (2.1)$$

where  $W_d$  is the dry mass of the membranes determined after drying in a desiccator and  $W_w$  is the wet mass of the membranes without excess surface water after soaking for 24 h. The ionic conductivity measurements were performed in a four-probe electrochemical impedance spectrometer using a PAR 2273 potentiostat. The membrane strips (1 × 3 cm)

were mounted in a conductivity cell and stabilized at a specific temperature (i.e., 25 °C or 60 °C) under nitrogen. The frequency region from 1 Hz to 2 MHz was scanned, where the impedance had a constant value. The ionic conductivity was calculated using Equation 2:2.

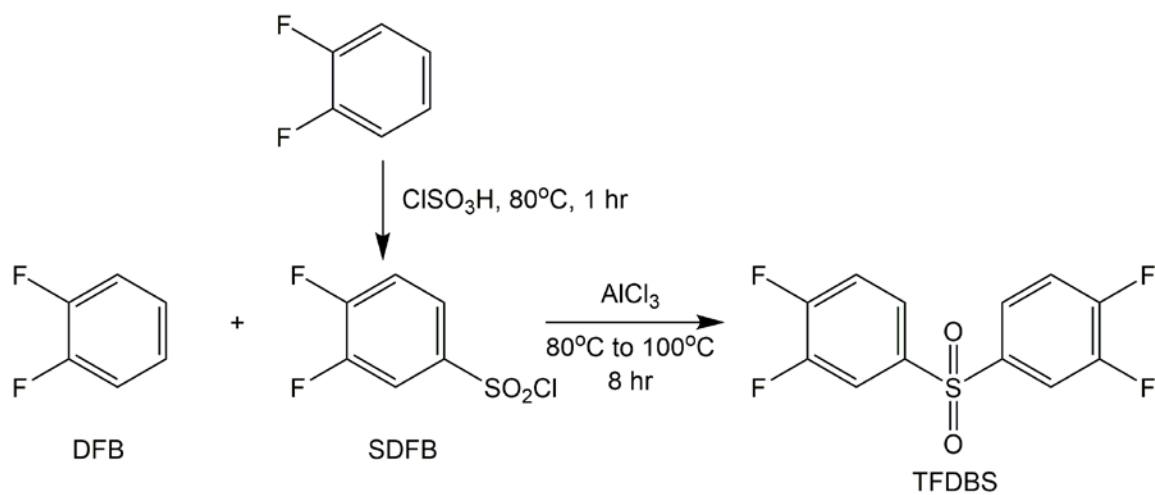
$$\sigma = \frac{L}{(Z' \times A)}, \quad (2.2)$$

where  $L$  is the length between sense electrodes (0.425 cm),  $Z'$  is the real component of the impedance response at a high frequency, and  $A$  is membrane surface area available for hydroxide conduction.

## 2.3. Results and Discussion

### 2.3.1 Synthesis and chemical structure determination of multiblock copolymers (mPES and mFPES) and random copolymers (rPES)

The monomer for additional fluorinated multiblock copolymers (mFPES), 3,3',4,4'-tetrafluorodiphenylsulfone (TFDPS) was synthesized by Friedel-Crafts sulfonation of 1,2-difluorobenzene with 3,4-difluorobenzene-1-sulfonyl chloride (SDFB) in the presence of anhydrous aluminum chloride ( $\text{AlCl}_3$ ) as a catalyst (Scheme 2.1). Figure 2.1 shows  $^1\text{H}$  spectra of SDFB and TFDPS. Successful sulfonation resulted that the integral ratio of  $^1\text{H}$  NMR peaks  $A'$  and  $B'$  in SDFB is 2:1, which is changed from 1:1 integral ratio in DFB. The chemical shift change of peaks  $A$  and  $B$  in TFDPS from SDFB proved the quantitative reaction between DFB and SDFB.



Scheme 2.1 Synthesis of 3,3',4,4'-tetrafluorodiphenylsulfone (TFDBS)

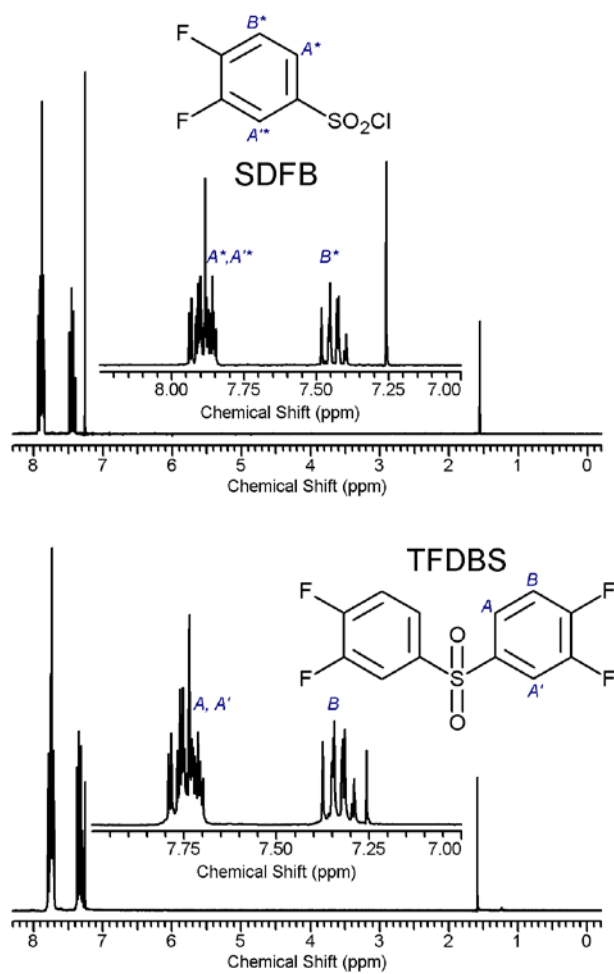
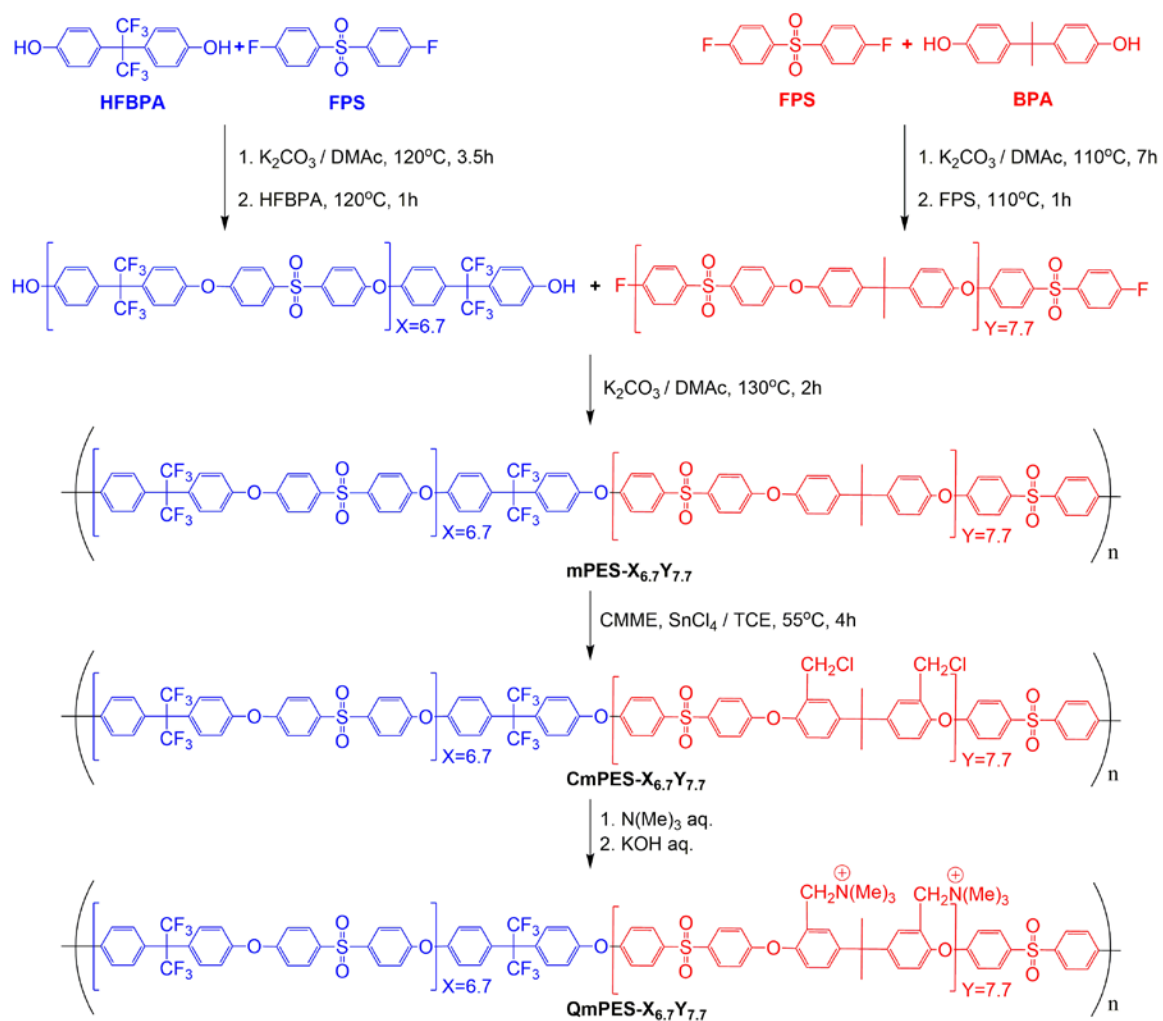


Figure 2.1  $^1\text{H}$  spectra of SDFB and TFDBS

A series of mPES copolymers were synthesized by polycondensation of separately prepared OH-terminated and F-terminated oligomers, as shown in Scheme 2.2. The length of each oligomer was carefully controlled by optimizing the polymerization time (i.e., 3.5 h to 7 h). The integral ratio of  $^1\text{H}$  NMR peaks  $b'$  and  $b$  allows calculation of the degree of polymerization for the hydrophobic OH-terminated oligomer, which is  $X = 6.7$  for the block shown in Figure 2.2 (a). In the same manner, the integral ratio of  $^1\text{H}$  NMR peaks  $e'$  and  $e$  allows calculation of the degree of polymerization for the F-terminated oligomer, which is  $Y = 7.7$  for the block shown in Figure 2.2 (b). The F-terminated oligomer will become the charge-carrying hydrophilic block after chloromethylation and quaternization, as described below.

As noted in Scheme 2.3, the preparation of mFPES multiblocks required a different procedure from that for mPES multiblock copolymers. The more active monomer TFDBS for nucleophilic aromatic substitution due to additional fluorine groups caused gelation problem during polymerization under the same condition as that for polymerization of mPESs. To avoid self-gelation process, the F-terminated oligomer was synthesized from TFDBS and HFBPA. The OH-terminated oligomer from BPA and FPS became charge-carrying hydrophilic segments. In addition, mild reaction conditions ( $90^\circ\text{C}$  for less than 3 hr) were also necessary to inhibit dramatic molecular weight increase and thereby gelation. The integral ratio of  $^1\text{H}$  NMR peaks  $b'$  and  $b$  allows the calculation of the degree of polymerization for the hydrophobic F-terminated oligomer, which is  $X = 4.8$  for the block shown in Figure 2.3 (a). In the same manner, the integral ratio of  $^1\text{H}$  NMR peaks  $g'$  and  $g$  allows the calculation of the degree of polymerization for the OH-terminated oligomer, which is  $Y = 6.0$  for the block shown in Figure 2.3 (b).

Homonuclear correlation spectroscopy (COSY) spectra assisted to assign peaks in  $^1\text{H}$  spectra to the accurate position of each proton in multiblock copolymers. Each crosspeak in Figure 2.4, showing COSY spectra of mPES- $\text{X}_{6.7}\text{Y}_{7.7}$  and mFPES- $\text{X}_{4.8}\text{Y}_{6.0}$ , indicates the correlation of two protons that are adjacent and thereby coupled each other (e.g., a-b, c-d, e-f, g-h correlations in Figure 2.4 (a) and b-a/c, d-e, f-g, h-I correlations in Figure 2.4 (b)). NMR peak assignments of oligomers and multiblock copolymers are presented in Figure 2.2, 2.3, and 2.4. A summary of the oligomer lengths, which are assumed to correspond to block lengths after incorporation into the multiblock copolymers, are shown in Table 2.1 along with the degrees of chloromethylation for the prepared copolymers.



Scheme 2.2. Synthesis of multiblock copoly(arylene ether sulfone), mPES-X<sub>6.7</sub>Y<sub>7.7</sub>, where X = the number of repeat units in hydrophobic block, Y = the number of repeat units in block that ultimately becomes hydrophilic and n = the degree of polymerization in the final polymer.

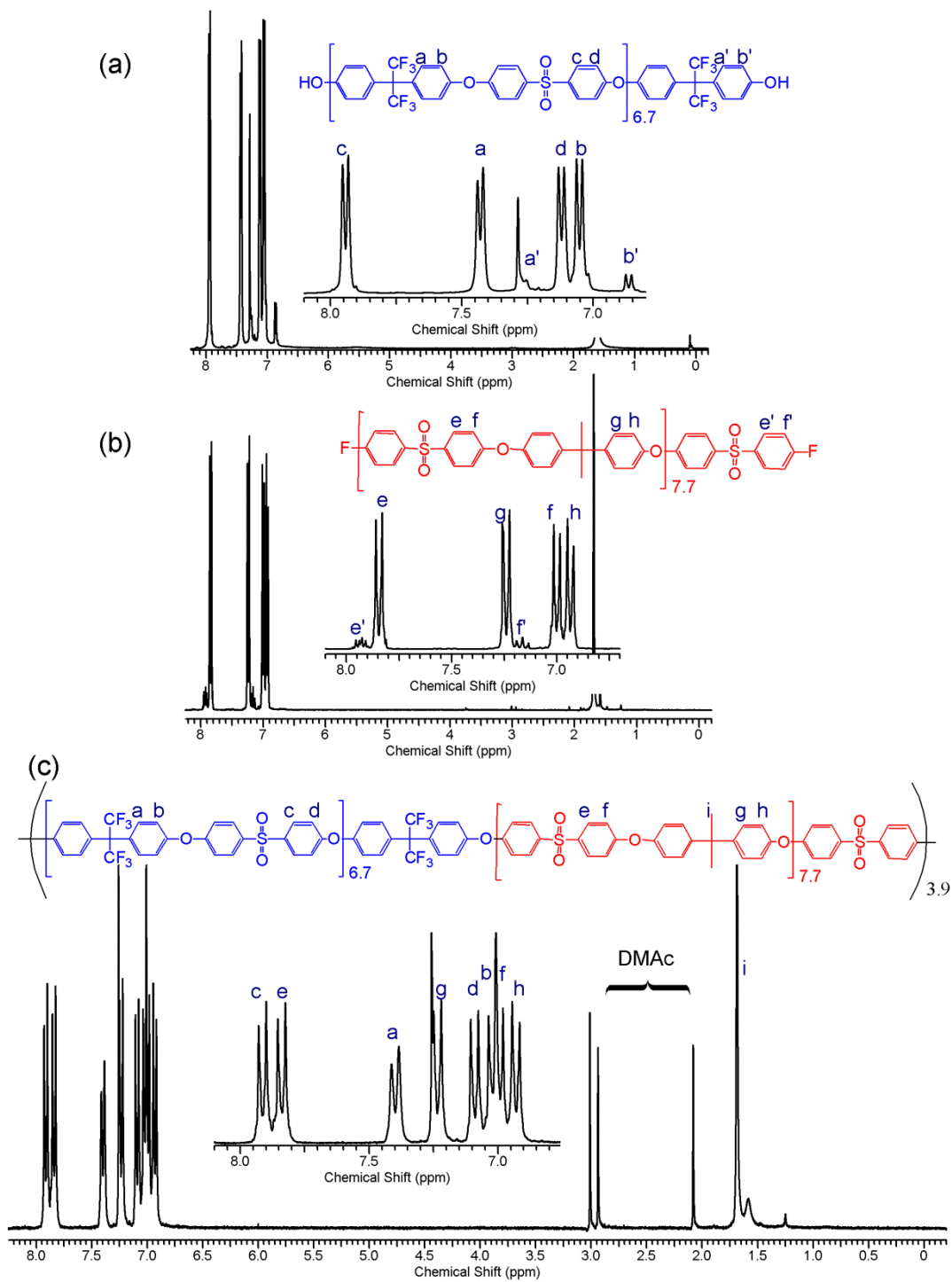
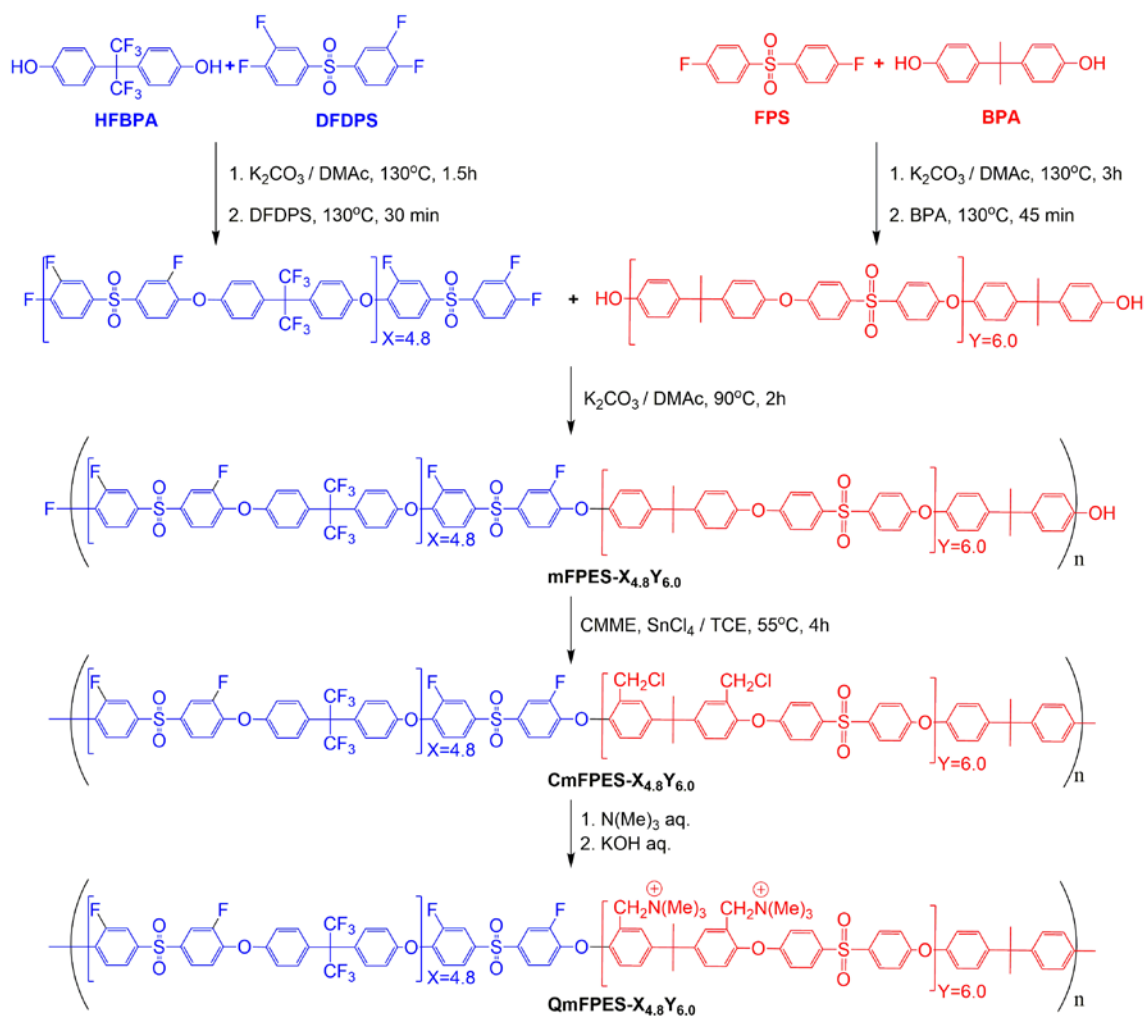


Figure 2.2.  $^1\text{H}$  NMR spectra of (a) the OH-terminated oligomer ( $X = 6.7$ ), (b) the F-terminated oligomer ( $Y = 7.7$ ), and (c) the resulting multiblock copolymer mPES- $X_{6.7}Y_{7.7}$ .



Scheme 2.3. Synthesis of the additional fluorinated multiblock copoly(arylene ether sulfone), mFPES- $X_{4.8}Y_{6.0}$ , where X = the number of repeat units in hydrophobic block, Y = the number of repeat units in block that ultimately becomes hydrophilic, and n = the degree of polymerization in the final polymer.

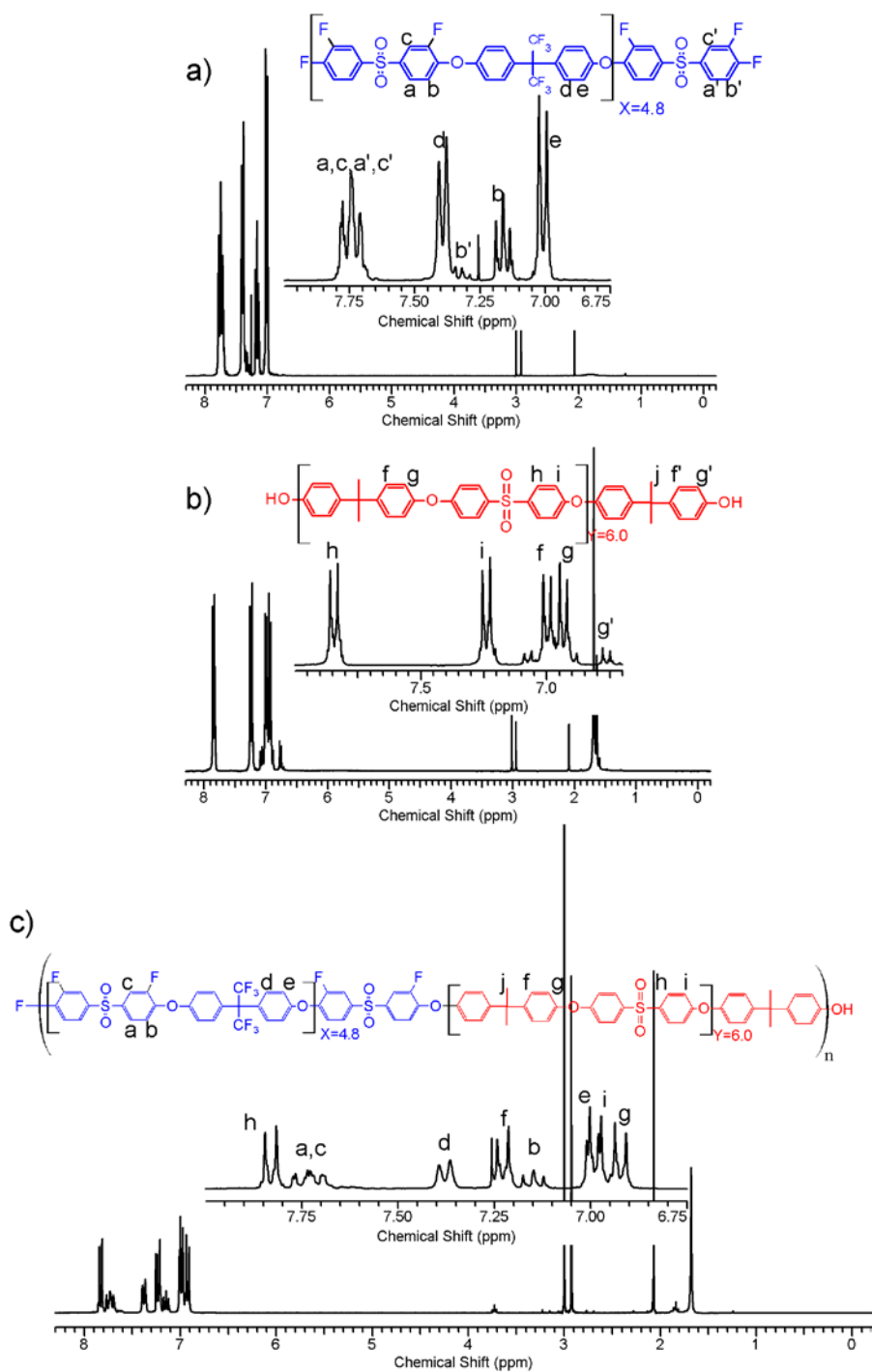


Figure 2.3.  $^1\text{H}$  NMR spectra of (a) the OH-terminated oligomer ( $X = 4.8$ ), (b) the F-terminated oligomer ( $Y = 6.0$ ), and (c) the resulting multiblock copolymer  $\text{mFPES-}X_{4.8}Y_{6.0}$ .

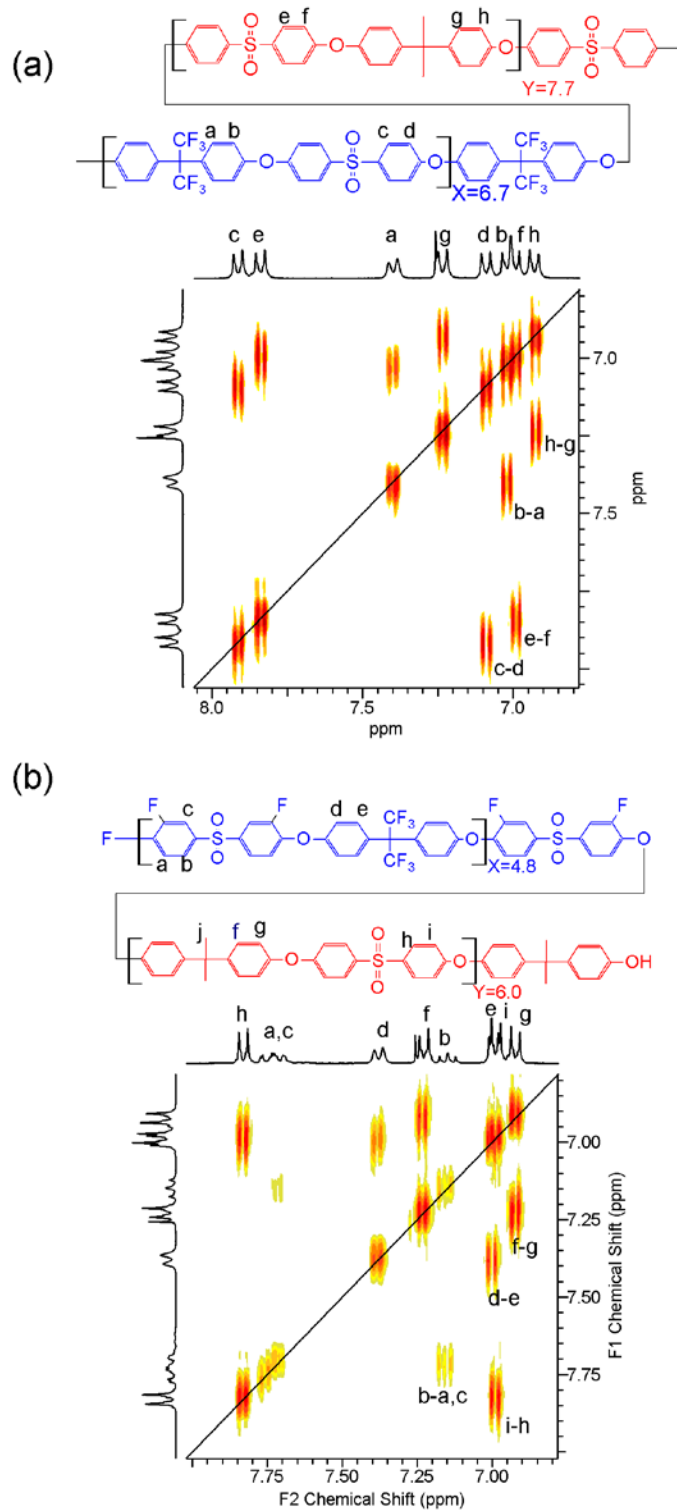


Figure 2.4. COSY spectra of (a) the multiblock copolymer mPES- $X_{6.7}Y_{7.7}$  and (b) the multiblock copolymer mFPES- $X_{4.8}Y_{6.0}$

Table 2.1 Structural characteristics and properties of multiblock and random copoly(arylene ether sulfone)s.

	Oligomer Repeat Units (X/Y) <sup>a</sup>	DC <sup>b</sup>	IEC <sup>c</sup>	Water uptake (%)	Conductivity (mS/cm)	
					at 25 °C	at 60 °C
mPES-X <sub>11.3</sub> Y <sub>3.4</sub>	11.3 / 3.4	2.4	1.1	13.5	2.4	5.0
mPES-X <sub>9.2</sub> Y <sub>3.4</sub>	9.2 / 3.4	2.8	1.5	18.0	4.9	12.7
mPES-X <sub>6.7</sub> Y <sub>3.4</sub>	6.7 / 3.4	2.1	1.4	24.5	15.7	37.7
mPES-X <sub>6.7</sub> Y <sub>2.5</sub>	6.7 / 2.5	2.0	1.0	8.4	3.2	7.2
mPES-X <sub>6.7</sub> Y <sub>7.7</sub>	6.7 / 7.7	2.1	2.3	47.5	13.9	27.9
mPES-X <sub>6.7</sub> Y <sub>11.1</sub>	6.7 / 11.1	2.2	2.8	57.5	14.2	29.0
rPES-X <sub>0.5N</sub> Y <sub>0.5N</sub>		2.0	2.0	31.1	11.5	25.0
rPES-X <sub>0.67N</sub> Y <sub>0.33N</sub>		2.1	1.4	16.0	5.7	13.6
mFPES-X <sub>5.6</sub> Y <sub>6.0</sub>	5.6 / 6.0	2.0	2.0	48.5	18.5	33.6
mFPES-X <sub>4.8</sub> Y <sub>6.0</sub>	4.8 / 6.0	1.9	2.0	49.0	27.6	43.6
mFPES-X <sub>5.6</sub> Y <sub>9.7</sub>	5.6 / 9.7	1.8	2.2	63.0	31.3	50.5
mFPES-X <sub>5.6</sub> Y <sub>14.7</sub>	5.6 / 14.7	2.0	3.0	147	29.2	48.7
mFPES-X <sub>3.5</sub> Y <sub>4.7</sub>	3.5 / 4.7	1.9	2.2	63.0	22.4	35.0
mFPES-X <sub>6.4</sub> Y <sub>4.7</sub>	6.4 / 4.7	2.0	1.7	25.0	17.4	31.4
rFPES-X <sub>0.5N</sub> Y <sub>0.5N</sub>		1.7	1.7		6.3	24.5

<sup>a</sup>X = the number of repeat units in hydrophobic block, Y = the number of repeat units in block that ultimately becomes hydrophilic.

<sup>b</sup>Degree of chloromethylation: the number of chloromethyl groups per Y-type repeat unit

<sup>c</sup>IEC = ion exchange capacity

The GPC elution curves for the mPES copolymers were unimodal and shifted to shorter elution times from those of the oligomers (cf. Figure 2.4), showing that the

polymerization was successful. The target molecular weight ( $M_n$ ) of the mPES was ca. 30 kg/mol allowing a free-standing film by a solvent casting method..

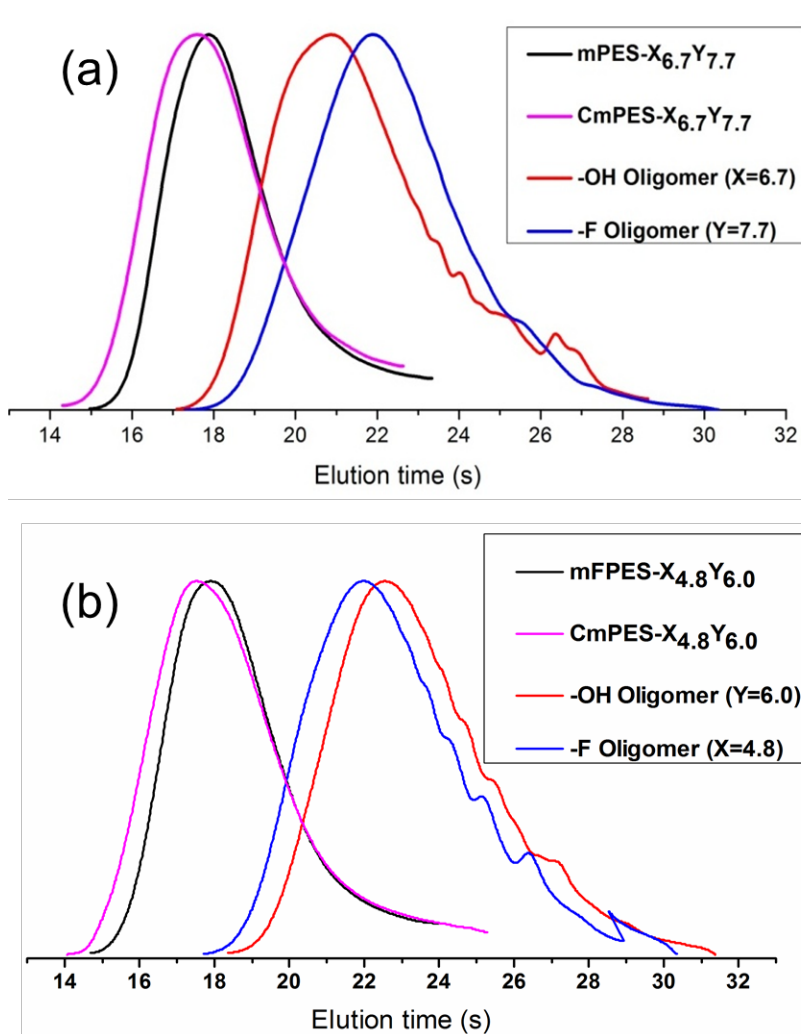


Figure 2.5. Gel permeation chromatograms of reactant oligomers, the resulting multiblock copolymer; (a) mPES- $X_{6.7}Y_{7.7}$ , and the corresponding chloromethylated product CmPES- $X_{6.7}Y_{7.7}$ , (b) mFPES- $X_{4.8}Y_{6.0}$ , and the corresponding chloromethylated product CmFPES- $X_{4.8}Y_{6.0}$

Random copoly(ether sulfone)s (rPES) were prepared in a one-pot polycondensation reaction of FPS, HFBPA, and BPA in the presence of  $K_2CO_3$ . The reaction of TFDBS, HFBPA, and BPA affords rFPESs. The feed ratio of each monomer

was controlled to afford rPES copolymers with the same overall ratio of repeat units as a given mPES copolymer. DEPT-135  $^{13}\text{C}$  NMR spectra for rPES and mPES are shown in Figure 2.6. A majority of the peaks for the multiblock copolymer, seen in Figure 2.6 (a), are sharp singlets. In contrast, most of the peaks for the random copolymer seen in Figure 2.6 (b) are multiplets. The randomly distributed repeat units in the rPES cause the peak splitting. These results clearly show that the multiblock copolymers have highly ordered structures compared to the random copolymers.<sup>48,49</sup>

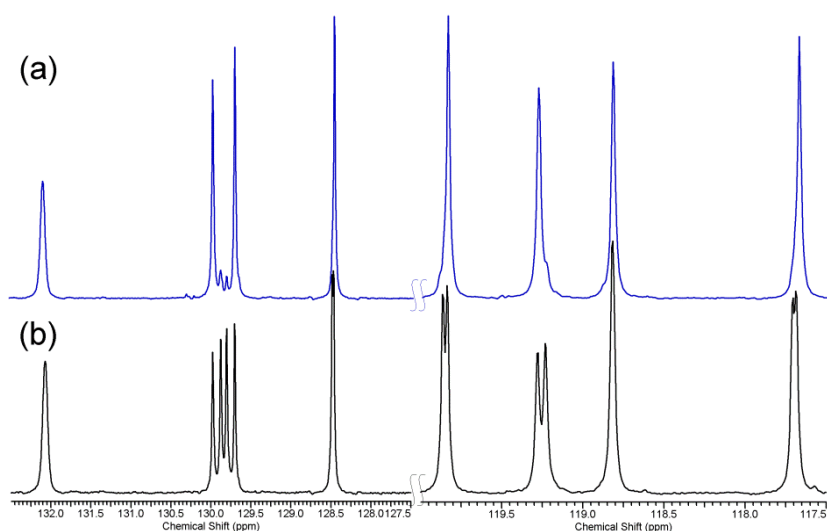


Figure 2.6. Selected aromatic region of DEPT-135  $^{13}\text{C}$  NMR spectra of (a) the multiblock copoly(arylene ether sulfone), mPES- $X_{6.7}Y_{7.7}$  and (b) the random copoly(arylene ether sulfone), rPES-  $X_{0.5N}Y_{0.5N}$ .

### 2.3.2. Synthesis and characterization of chloromethylated (CmPES and CmFPES) and quaternized multiblock copolymers (QmPES and QmFPES)

The multiblock copolymers were chloromethylated by the Friedel-Crafts reaction using CMME and  $\text{SnCl}_4$  in TCE solution (cf. Scheme 2.2 and 2.3). The resulting chemical structures (CmPES and CmFPES) were characterized with  $^1\text{H}$  NMR and COSY,

and the degree of chloromethylation was evaluated by  $^1\text{H}$  NMR. The new peak at 4.53 ppm in the  $^1\text{H}$  NMR spectrum of CmPES- $X_{6.7}Y_{7.7}$ , shown in Figure 2.7, was assigned to the methylene protons of the chloromethyl groups. And new peaks at 6.85, 7.15, and 7.35 ppm indicated that substitution of the  $-\text{CH}_2\text{Cl}$  groups changed the chemical shift of the BPA aromatic protons. The presence of these new peaks in the NMR spectra of the CmPES materials shows that the chloromethylation reaction was successful. The degree of chloromethylation (DC) in Table 2.1 was obtained by integrating the  $^1\text{H}$  NMR peak areas and comparing the ratio of the  $-\text{CH}_2\text{Cl}$  methylene protons to the dimethyl BPA protons. Likewise, the peak at 4.54 ppm in the  $^1\text{H}$  NMR spectrum of CmFPES- $X_{4.8}Y_{6.0}$ , as shown in Figure 2.8 was assigned to the methylene protons of the chloromethyl groups. And new peaks at 6.85, 7.15, and 7.35 ppm proved that the  $-\text{CH}_2\text{Cl}$  groups are located on the ortho position of the BPA aromatic protons. Previous studies reported the undesirable gelation of polymers caused by crosslinking during chloromethylation.<sup>50</sup> GPC evaluation of the CmPES materials was conducted to examine whether the molecular weight changed due to chloromethylation. As shown in Table 2.1 and Figure 2.5, the chloromethylated multiblock copolymers do not exhibit significantly different molecular weight characteristics from their multiblock copolymer precursors and therefore did not undergo gelation during chloromethylation.

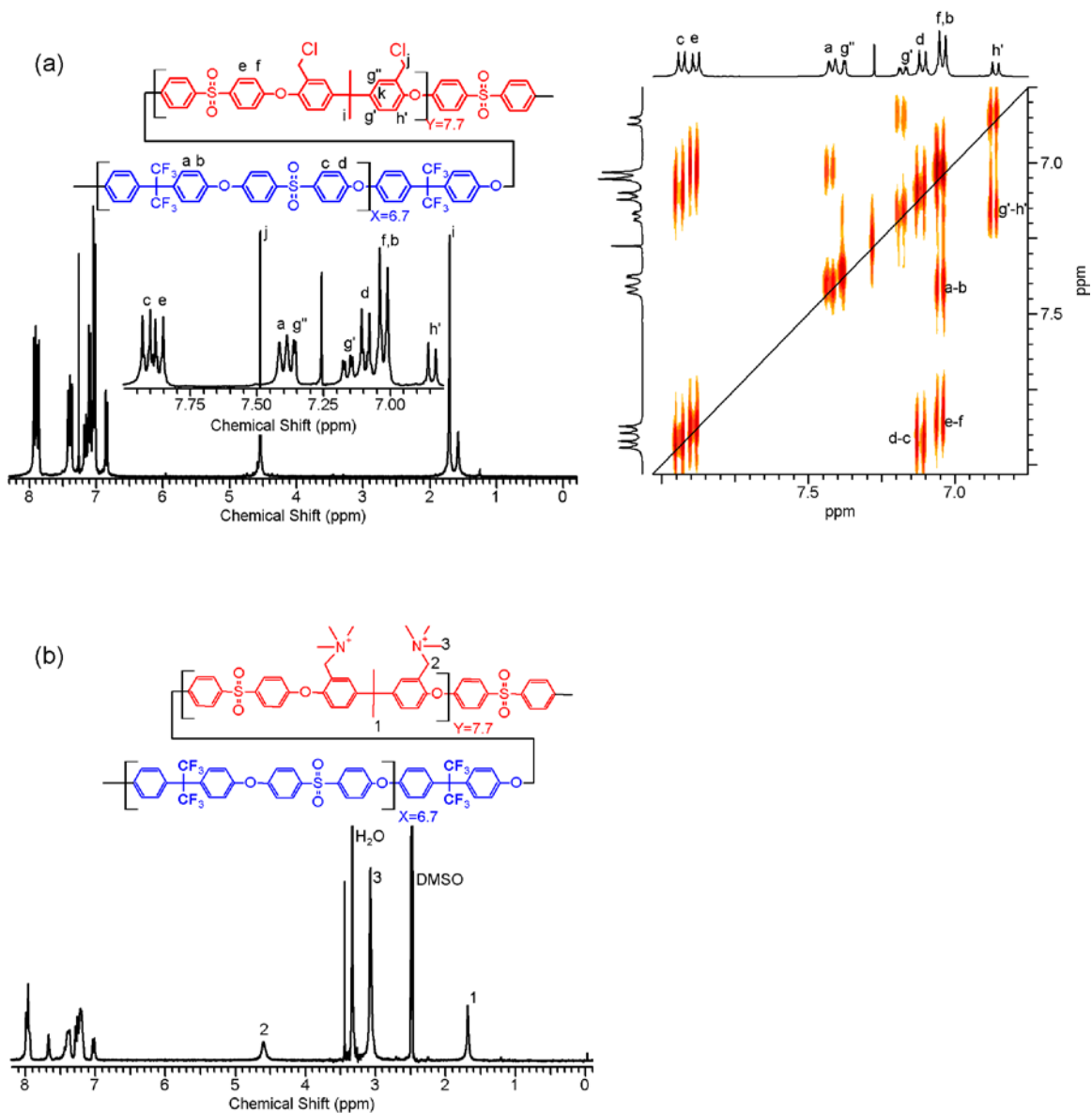


Figure 2.7.  $^1\text{H}$  NMR spectra of the multiblock copoly(arylene ether sulfone), mPES- $X_{6.7}Y_{7.7}$ , after (a) chloromethylation to give CmPES- $X_{6.7}Y_{7.7}$ , and (b) quaternization to give QmPES- $X_{6.7}Y_{7.7}$ .

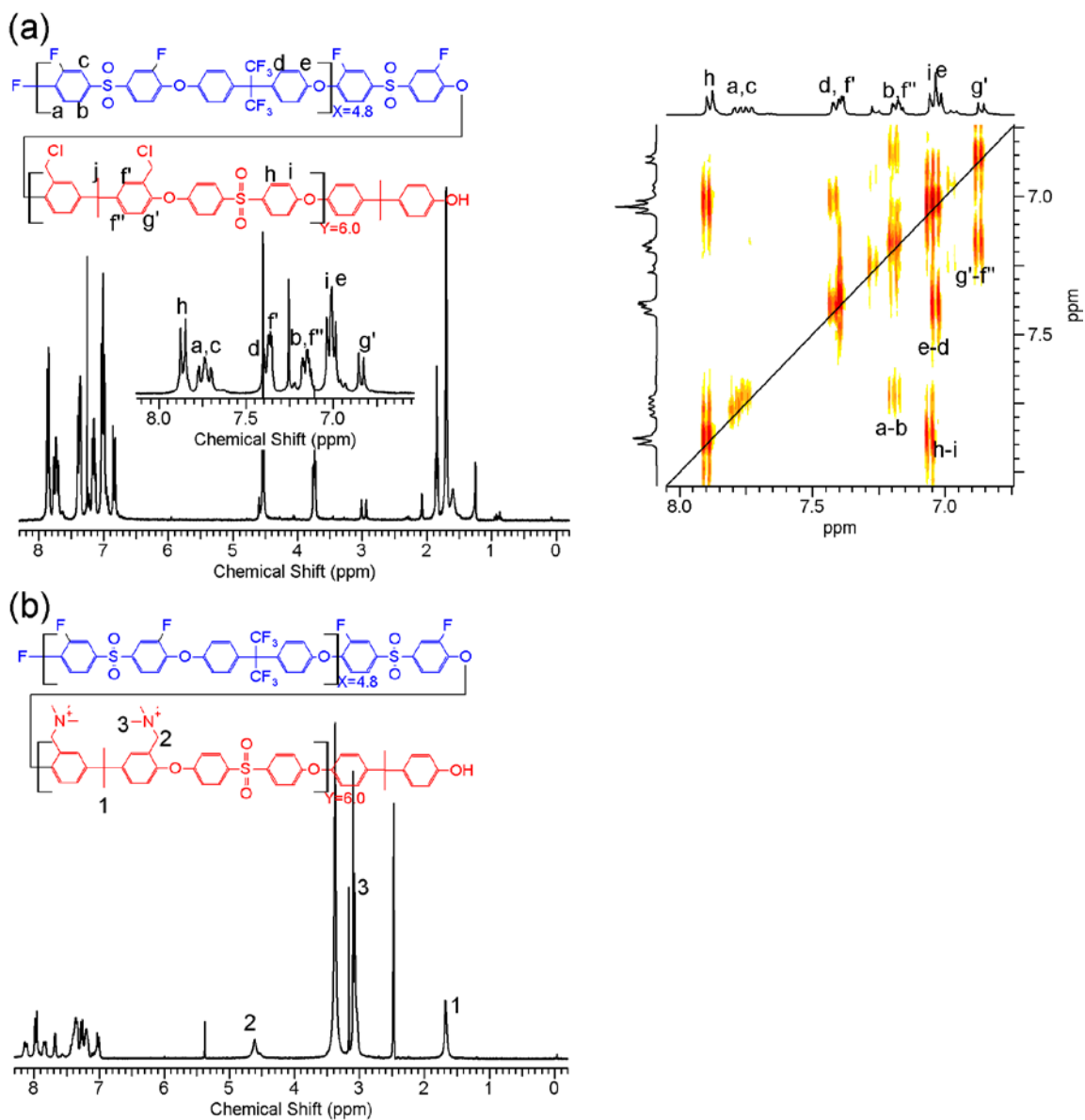


Figure 2.8  $^1\text{H}$  NMR spectra of the multiblock copoly(arylene ether sulfone), mFPES- $X_{4.8}Y_{6.0}$ , after (a) chloromethylation to give CmFPES- $X_{4.8}Y_{6.0}$ , and (b) quaternization to give QmFPES- $X_{4.8}Y_{6.0}$ .

It was expected that Friedel-Crafts alkylation of the chloromethyl groups should selectively occur at the BPA moiety that is more electron-rich than hexafluoroisopropylidene diphenyl and diphenyl sulfone groups. The disappearance of the peak at 6.9 ppm (the peak *h* in Figure 2.2) and the peak at 6.9 ppm (the peak *g* in Figure

2.3) after chloromethylation indicates that chloromethyl groups are attached at the ortho position to oxygen of the BPA. The two-dimensional HMBC spectrum was also obtained to verify the location of the chloromethyl group. In two-dimensional HMBC spectra, cross peaks signify the coupling of proton and carbon nuclei separated by two or three chemical bonds.<sup>51</sup> Unlike HSQC spectra that only reveal one-bond carbon-proton connectivity, HMBC spectra can be used to observe quaternary carbons and thereby provide valuable insight into substituents on aromatic rings. Figure 2.9 shows the HMBC spectra of CmPES-X<sub>6.7</sub>Y<sub>7.7</sub> and CmFPES-X<sub>4.8</sub>Y<sub>6.0</sub>, respectively.

Cross peak 1 in Figure 2.9 (a) is assigned to correlate the methyl protons (H<sub>i</sub>) with the aromatic quaternary carbon (C<sub>k</sub>) of the BPA. Cross peak 2 correlates the aromatic quaternary carbon, C<sub>k</sub>, with the aromatic proton (H<sub>h'</sub>). Cross peak 3 shows that the aromatic proton, H<sub>h'</sub>, is coupled to another aromatic quaternary carbon (C<sub>h</sub>) to which the chloromethyl group is attached. The position of the -CH<sub>2</sub>Cl groups are shown by the position of cross peak 4. This peak shows the correlation between C<sub>h</sub> and the methylene protons (H<sub>j</sub>) of the chloromethyl groups. The identical analysis is also possible for CmFPES-X<sub>4.8</sub>Y<sub>6.0</sub>. Cross peak 1 in Figure 2.9 (b) is assigned to correlate the methyl protons (H<sub>k</sub>) with the aromatic quaternary carbon (C<sub>m</sub>) of the BPA. Cross peak 2 correlates the aromatic quaternary carbon, C<sub>m</sub>, with the aromatic proton (H<sub>g'</sub>). Cross peak 3 shows that the aromatic proton, H<sub>g'</sub>, is coupled to another aromatic quaternary carbon (C<sub>g</sub>) to which the chloromethyl group is attached. The position of the -CH<sub>2</sub>Cl groups are shown by the position of cross peak 4. This peak shows the correlation between C<sub>g</sub> and the methylene protons (H<sub>k</sub>) of the chloromethyl groups.

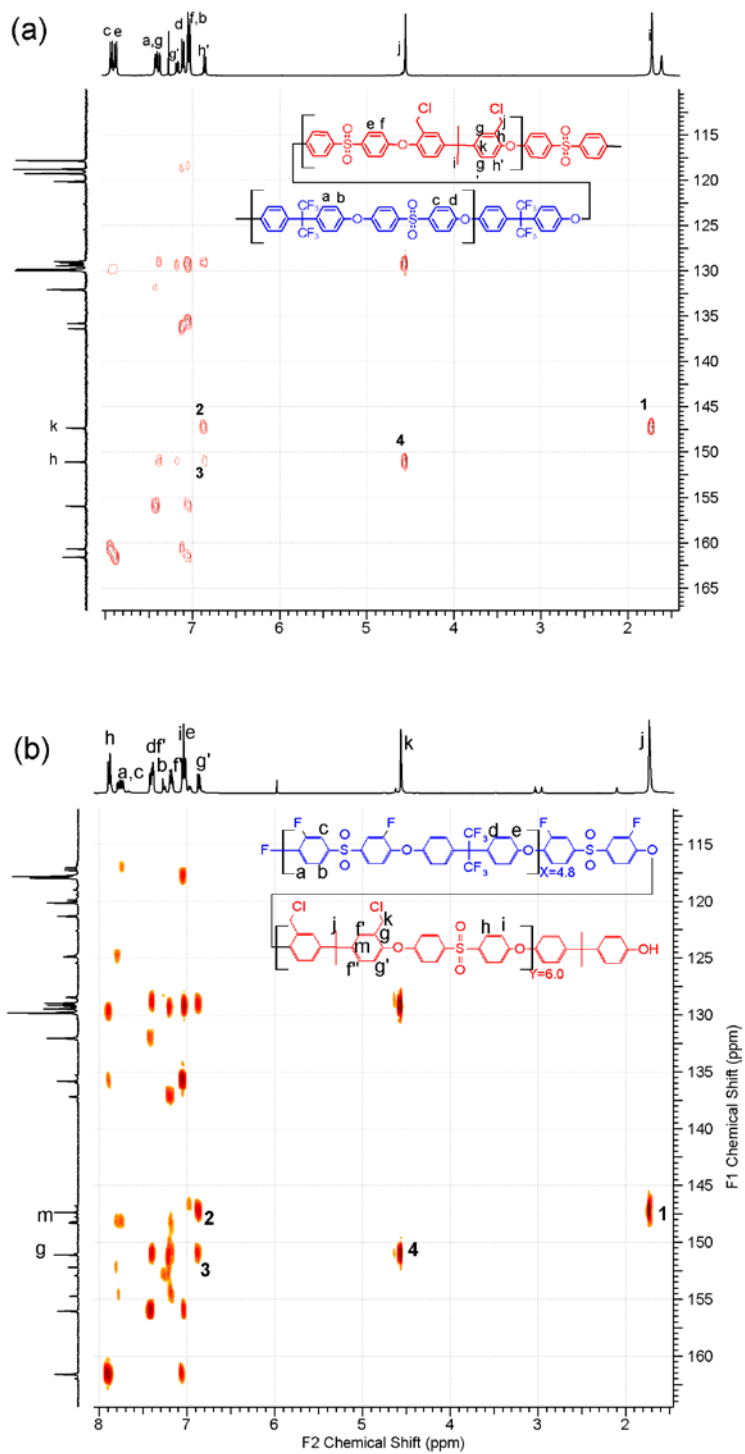


Figure 2.9. HMBC NMR spectra of the chloromethylated multiblock copoly(arylene ether sulfone)s, (a) CmPES- $X_{6.7}Y_{7.7}$ .and (b) CmFPES- $X_{4.8}Y_{6.0}$ .

The quaternary ammonium salt of CmPES was formed by immersing the dried powder in an aqueous trimethylamine solution. The quaternized copolymer (QmPES and QmFPES) had different solubility characteristics from CmPES and CmFPES. The quaternized copolymers were soluble in aprotic polar solvents such as DMSO, DMF, and DMAc.  $^1\text{H}$  NMR was used to investigate the chemical structure and completion of the chemical reaction for QmPES and QmFPES polymers, as shown in Figure 2.7 (b) and Figure 2.8 (b). The position of the amino methylene protons (4.63 ppm) shifted slightly downfield from that of the chloromethylene protons (4.53 ppm). The ratio of the integrated peaks between the amino methylene protons and the dimethyl protons of the BPA was consistent during the quaternization reaction. This comparison confirmed completion of the reaction. The integrated peak value for the trimethyl protons also supports quantitative quaternization.

The ion exchange capacity (IEC) of the QPES copolymers was computed using equation 2.3:

$$IEC = \frac{DC \times Y}{X \times M_{w,Phob} + Y \times M_{w,Phil}} \times 1000, \quad (2.3)$$

where DC is the degree of chloromethylation,  $M_{w,phob}$  is the repeat-unit molecular weight of the hydrophobic block, and  $M_{w,phil}$  is the repeat-unit molecular weight of the hydrophilic block. The IEC values for the copolymers are summarized in Table 2.1.

### 2.3.3. Membrane formation, water uptake, and hydroxide ion conductivity of QmPES and QmFPES.

Free-standing QPES membranes were obtained by solution casting from DMF. The chloride ion was exchanged for hydroxide in the membranes immediately before measuring the water uptake and ionic conductivity to minimize the effect of converting the hydroxide into carbonate through contact with CO<sub>2</sub> in air. Water uptake is particularly important for ion-exchange polymers used as ionomers in fuel cell electrodes. Typically, ionic conductivity is proportional to water uptake. However, excessive water uptake can swell the polymer and decrease its free volume resulting in poor reactant transport within the electrodes. Thus, the optimum ionomer has moderate water uptake and high conductivity.<sup>40</sup> Table 2.1 summarizes the water uptake at room temperature and hydroxide ion conductivities at 25°C and 60°C.

Since the DC of the membranes is approximately the same (cf. Table 2.1), the IEC is mostly determined by the ratio of the lengths of the charge-carrying hydrophilic to hydrophobic blocks (Y/X). As shown in Table 2.1, IEC and water uptake generally increase with increasing Y/X values (i.e., hydrophilic block content). However, the ionic conductivity does not exhibit a clear dependence on Y/X or IEC values. Moreover, it should be noted that QmPES-X<sub>6.7</sub>Y<sub>3.4</sub> showed the highest anionic conductivity in comparison to the other QmPES series in spite of its moderate IEC and water uptake. A comparison between multiblock and random copolymers with similar IEC and Y/X values, for example mPES-X<sub>6.7</sub>Y<sub>3.4</sub>,  $\sigma = 37.7$  mS/cm at 60°C, versus rPES-X<sub>0.67N</sub>Y<sub>0.33N</sub>, 13.6 mS/cm and mPES-X<sub>6.7</sub>Y<sub>7.7</sub>, 27.7 mS/cm, versus rPES-X<sub>0.5N</sub>Y<sub>0.5N</sub>, 25.0 mS/cm, clearly reveals that the multiblock copolymers exhibit higher ionic conductivity. A higher

conductivity of additional fluorinated multiblock copolymers compared to mPES with similar IEC (e.g., mFPES-X<sub>4.8</sub>Y<sub>6.0</sub>,  $\sigma = 43.6$  mS/cm at 60°C versus mPES-X<sub>6.7</sub>Y<sub>7.7</sub>,  $\sigma = 27.9$  mS/cm) was appeared. The overall observation of conductivities of multiblock copolymer and random copolymer AEMs are not simply a result of the IEC and water uptake. Rather, the phase separated morphology caused by different segment lengths, the degree of randomness, and polarity is important; the specific nanophase structure of the multiblock material contributes to a more facile form of ionic transport.

The phase separation in polymer systems can be explained by the fundamental thermodynamics in polymer mixing. When two polymers are blended, the miscibility of two polymers is determined by the following equation (Equation 2.4).

$$\Delta G_m = \Delta H_m - T\Delta S_m \quad (2.4)$$

where  $\Delta G_m$  is Gibb's free energy of mixing,  $\Delta H_m$  is enthalpy of mixing,  $\Delta S_m$  is entropy of mixing, and T is temperature. If  $\Delta G_m$  is negative (i.e.,  $\Delta H_m < T\Delta S_m$ ), two polymers are completely miscible. Considering the lattice theory (Equation 2.5 and 2.6), developed by Flory and Huggins, helps estimate the miscibility with parameters relating to characteristics of polymers.

$$\Delta S_m = -k(n_1 \ln \Phi_1 + n_2 \ln \Phi_2) \quad (2.5)$$

$$\Delta H_m = kT\chi_{12}N\Phi_1\Phi_2 \quad (2.6)$$

where  $\Phi_1$  and  $\Phi_2$  are the volume fraction of polymer 1 and polymer 2, respectively.  $N = n_1 + n_2$  is the total number of polymer molecules and  $\chi_{12}$  is interaction parameter between polymer 1 and polymer 2, called Flory-Huggin's interaction parameter. In summary, the miscibility of a binary polymer blend system is estimated by the parameters

such as Flory-Huggin's interaction parameter ( $\chi_{12}$ ), the number of polymer molecules ( $N$ ), and the volume fraction ( $\Phi_1$ ).

This thermodynamics is also employed to explain the phase separated morphology of block copolymer systems. In the block copolymer system,  $\chi$  is the segment-segment interaction parameter,  $N$  is the overall degree of polymerization,  $\Phi$  (or  $f$ ) is the composition. Since the entropic and enthalpic contribution to Gibb's free energy is proportional to  $N^{-1}$  and  $\chi$ , respectively, the product  $\chi N$  is often used as an indicator of phase separation in block copolymer systems. The phase separation is represented in the plot of  $\chi N$  as a function of composition, which is called a phase diagram. Figure 2.10 is an example of the phase diagram for poly(styrene)-block-poly(isoprene) copolymer.<sup>52</sup>

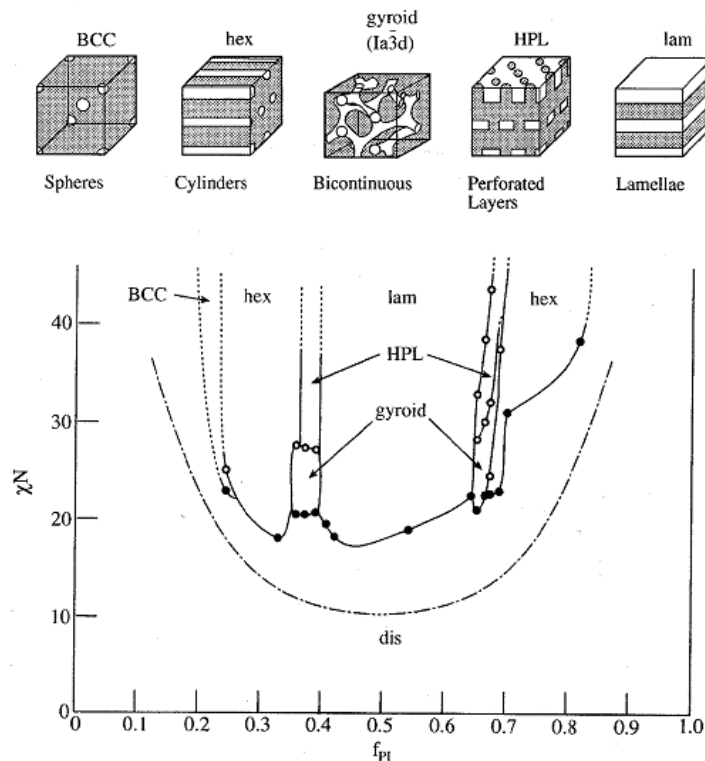


Figure 2.10. Experimental phase diagram for PS-b-PI diblock copolymer<sup>52</sup>

As indicated in Figure 2.10, phase separation (i.e., ordered structure) occurs when  $\chi N$  is greater than 10.5 for diblock copolymer system.<sup>53</sup> Even though the multiblock copolymer has different architectural characteristics from the diblock copolymer, the rough estimation of phase separation in the multiblock copolymer is possible using the phase diagram for the diblock copolymer. The phase separated morphology of the QmFPES and QrFPES was characterized by tapping mode AFM, as shown in Figure 2.11. A nano-segregated morphology was observed for the fully hydrated multiblock copolymer membrane. In contrast, the random copolymer does not exhibit a clear nano-separated morphology. Phase separation between hydrophobic domains and hydrophilic domains disappeared as the membrane dried. The morphological discrepancy for the wet sample and the dry sample must be caused by the difference of  $\chi$  because the degree of polymerization and the composition is exactly the same. In other words, water absorbed in the membrane seems to increase  $\chi$ . This postulation is supported by the fact that a polarity difference increases in the presence of water. Moreover, molecular weights of polymers ( $\sim 30$  kg/mol; i.e., low  $N$ ) are not high enough to develop spontaneous phase separation. The comparison between Figure 2.11 (a) and Figure 2.11 (b) might indicate that the higher regularity of the multiblock copolymer membrane (QmFPES- $X_{5.6}Y_{14.7}$ ) than that of the random copolymer membrane (QrFPES- $X_{0.5N}Y_{0.5N}$ ) leads to higher  $\chi$  parameter, and thus a more distinct phase separation is developed. The similar morphological AFM images were appeared with sulfonated block copoly(arylene ether sulfone) proton exchange membranes.<sup>54</sup>

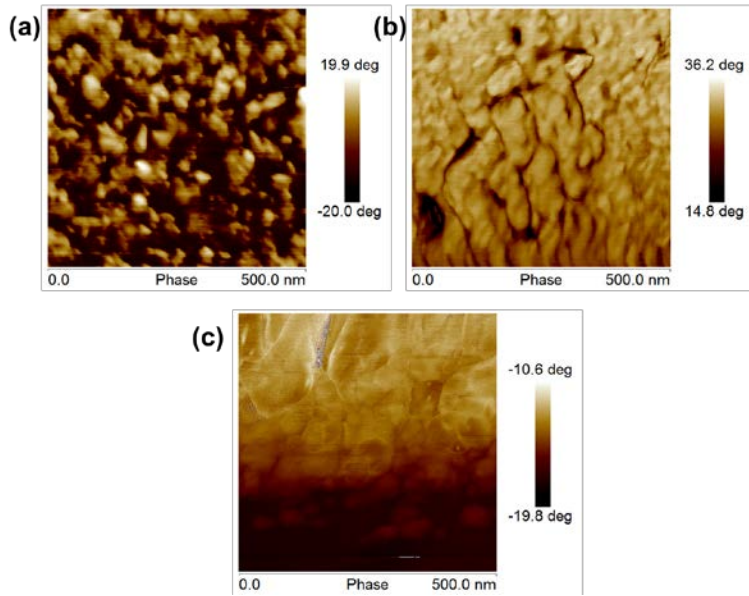


Figure 2.11. Tapping mode AFM phase images: (a) QmFPES- $X_{5.6}Y_{14.7}$ , (b) QrFPES- $X_{0.5N}Y_{0.5N}$ , and (c) dry QmFPES- $X_{5.6}Y_{14.7}$

# CHAPTER 3

## NMR RELAXATION TIMES FOR CHARACTERIZING THE EFFICIENCY OF ION CHANNELS

### 3.1. Introduction and Objectives

Since the principle of NMR relaxation process is the energy exchange of one proton spin with other proton spins and the energy exchange between the spin system and the surrounding lattice, NMR relaxation times can sensitively reflect the rate and the nature of molecular motions within a confined geometry. NMR spin-lattice ( $T_1$ ) and spin-spin ( $T_2$ ) relaxation times provide direct indications of the restricted motions of water in confined environments or near surfaces. Proton NMR relaxation time measurements had been employed to investigate molecular dynamics.<sup>55,56</sup> In this section of the thesis, the phase-separated morphologies of the copolymers were probed by measuring the NMR spin-lattice ( $T_1$ ) and spin-spin ( $T_2$ ) relaxation times of water absorbed in the anion-conductive polymeric matrices. Compared to atomic force microscopy (AFM) and transmission electron microscopy (TEM), NMR relaxation time measurements can be used to obtain quantitative water/ion mobility through the polymer membranes without laborious sample preparation.<sup>57</sup> The mobility information extracted from the NMR relaxation times of water in the polymers was then correlated with ionic conductivity. These studies aim at an understanding of the effect of structural parameters such as the lengths of each segment in the multiblock, the degree of randomness, and the polarity

difference between hydrophilic blocks and hydrophobic blocks on water/ion mobility and thus conductivity.

### **3.2. Experimental Details**

The QPES membranes in hydroxide form were stored in distilled water for at least one week prior to NMR studies in order to fully hydrate. A  $3 \times 10$  mm membrane strip was loaded into a 7-mm solid-state NMR rotor and  $^1\text{H}$  NMR spin-lattice ( $T_1$ ) and spin-spin ( $T_2$ ) relaxation times were measured at 25 °C using a Bruker DSX-300. The inversion recovery sequence,  $180^\circ\text{-}\tau\text{-}90^\circ$ , was used for the  $T_1$  measurements, and the Carr–Purcell–Meiboom–Gill pulse sequence (CPMG) was used for the  $T_2$  measurements with an interpulse delay of 0.2 ms.

### **3.3. Results and Discussion**

The nature of the ion/water channels in the copolymers synthesized were investigated by examining NMR relaxation times using the inversion recovery pulse sequence for  $T_1$  measurements and the CPMG pulse sequence for  $T_2$  measurements. The relaxation times, summarized in Table 3.1, correspond to water in the membranes rather than polymer protons. This is confirmed by the absence of peaks at 7 to 8 ppm belonging to the polymer as shown in Figure 3.1. In addition, the water content in the membranes was high enough (8.4 ~ 54.7%) so that the NMR peaks due to water dominated the NMR peaks due to the polymer.

Table 3.1 Water uptake, IEC, relaxation times, and ion conductivity of QPES membranes

	X/Y	IEC	Water uptake (%)	$T_1$ (ms)	$T_2$ (ms)	Conductivity (mS/cm)	
						at 25 °C	at 60 °C
mPES- X <sub>11.3</sub> Y <sub>3.4</sub>	0.30	1.1	13.5	309	28.0	2.4	5.0
mPES- X <sub>9.2</sub> Y <sub>3.4</sub>	0.37	1.5	18.0	304	33.3	4.9	12.7
mPES- X <sub>6.7</sub> Y <sub>3.4</sub>	0.51	1.4	24.5	224	20.2	15.7	37.7
mPES- X <sub>6.7</sub> Y <sub>2.5</sub>	0.37	1.0	8.4	229	22.2	3.2	7.2
mPES- X <sub>6.7</sub> Y <sub>7.7</sub>	1.15	2.3	47.5	376	48.0	13.9	27.9
mPES- X <sub>6.7</sub> Y <sub>11.1</sub>	1.66	2.8	57.5	483	95.6	14.2	29.0
rPES- X <sub>0.5N</sub> Y <sub>0.5N</sub>	~ 1.0	2.0	31.1	324	57.2	11.5	25.0
rPES- X <sub>0.67N</sub> Y <sub>0.33N</sub>	~ 0.5	1.4	16.0	212	50.2	5.7	13.6

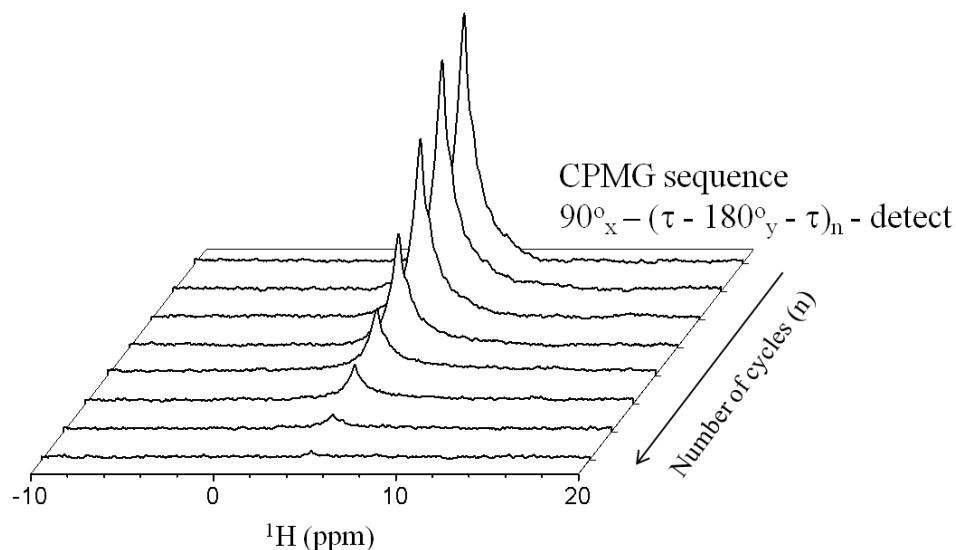


Figure 3.1.  $^1\text{H}$  NMR stack plot of CPMG spectra of QmPES- $X_{6.7}Y_{3.4}$  as a function of the number of cycles.

As shown in Table 3.1, the sample that exhibits the highest ion conductivity (15.7 mS/cm at 25 °C and 37.7 mS/cm at 60 °C) is the multiblock copolymer mPES- $X_{6.7}Y_{3.4}$ . The random copolymer with the same IEC (1.38 meq/g), rPES- $X_{0.67N}Y_{0.33N}$ , exhibited much lower conductivity (5.7 mS/cm at 25 °C and 13.6 mS/cm at 60 °C), but it also absorbed less water (16 versus 24.5%). However, despite the higher water content, the multiblock exhibits a  $T_2$  relaxation time that is significantly shorter (20.2 ms) than the  $T_2$  for the random copolymer (50.2 ms) (cf. Figure 3.2). The same relationships are also observed for another pair of multiblock and random copolymers with approximately the same IEC, mPES- $X_{6.7}Y_{7.7}$  (IEC = 2.28 meq/g) and rPES- $X_{0.5N}Y_{0.5N}$  (IEC = 2.17 meq/g): the multiblock copolymer exhibits the higher water uptake and conductivity, and the lower  $T_2$  value. For this to occur, the water molecules that are present in the multiblock must be more closely interacting with the solid polymer than the water in the random

copolymer. This implies that the water in the random copolymer pools in such a fashion that is inefficient for ion conductivity. This observation is consistent with previously reported studies<sup>26</sup> in which the authors claimed that multiblock copolymer AEMs with well-developed phase-separated morphologies utilize water molecules in hydrophilic blocks more efficiently than random copolymers for hydroxide ion transport.

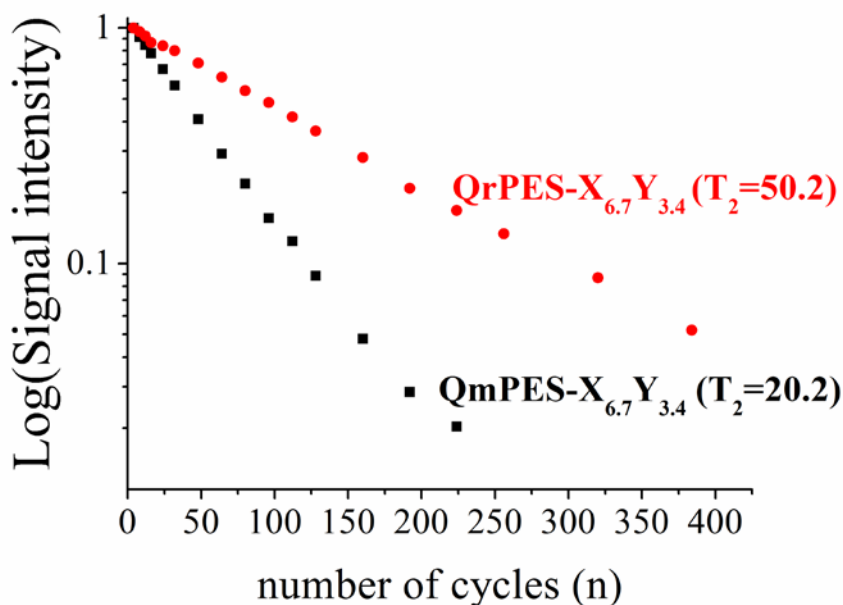


Figure 3.2. Signal intensity for CPMG spectra of QmPES-X<sub>6.7</sub>Y<sub>3.4</sub> and QrPES-X<sub>0.67N</sub>Y<sub>0.33N</sub> as a function of the number of cycles.

The sample that exhibits the highest ion conductivity, mPES-X<sub>6.7</sub>Y<sub>3.4</sub>, is not the sample with the greatest IEC or water uptake, in contrast to many, but not all,<sup>58, 59</sup> published reports on PEM polymers. Conductivity versus IEC is shown in Figure 3.3(a) for the multiblock copolymers. The samples with IEC values greater than 1.38 meq/g exhibit lower conductivities than the mPES-X<sub>6.7</sub>Y<sub>3.4</sub> multiblock copolymer. This trend is

similar to the one shown for a plot of conductivity versus water uptake in Figure 3.3(b). The sample with the highest conductivity does not absorb the most water. Such trends have been reported in the literature by Peckham et al. for an  $\alpha,\alpha,\beta$ -trifluorostyrene-based PEM: maximum conductivity was reached at  $\text{IEC} \approx 2$  meq/g after which the conductivity decreased and finally leveled off with increasing IEC.<sup>59</sup> Tsang et al. also observed the same trend for proton-conductive fluorosulfonic ionic graft copolymers.<sup>58</sup> Both publications attributed this non-linear relationship to a dilution of the available sulfonic acid groups caused by a significant increase in water. As shown in Figure 3.3(c), water uptake increases monotonically with IEC, as is often observed and expected. Figure 3.3(d) shows that  $T_2$  also generally increases with IEC, especially for the two multiblock copolymers with  $\text{IEC} > 1.38$  meq/g, indicating that the fraction of water that interacts with the ionic polymer segments decreases for the higher water contents. The observed relationships are indeed interesting and warrant further study.

For the following group of multiblock copolymers that do not contain the most conductive sample (i.e., mPES- $X_{6.7}Y_{2.5}$ , mPES- $X_{6.7}Y_{7.7}$ , and mPES- $X_{6.7}Y_{11.1}$ ),  $T_1$  and  $T_2$  increase as the length of the hydrophilic segment (Y) increases for the same hydrophobic segment length ( $X = 6.7$ ). This trend is consistent with the concept that longer hydrophilic blocks generate morphologies with larger aqueous domains, and is consistent with the water uptake values (8.4, 47.5, and 57.5%). No significant effect on the NMR relaxation times is observed for the multiblock copolymers with the same hydrophilic segment length ( $Y = 3.4$ ) but different hydrophobic segment lengths of  $X = 11.3$  and  $X = 9.2$ .

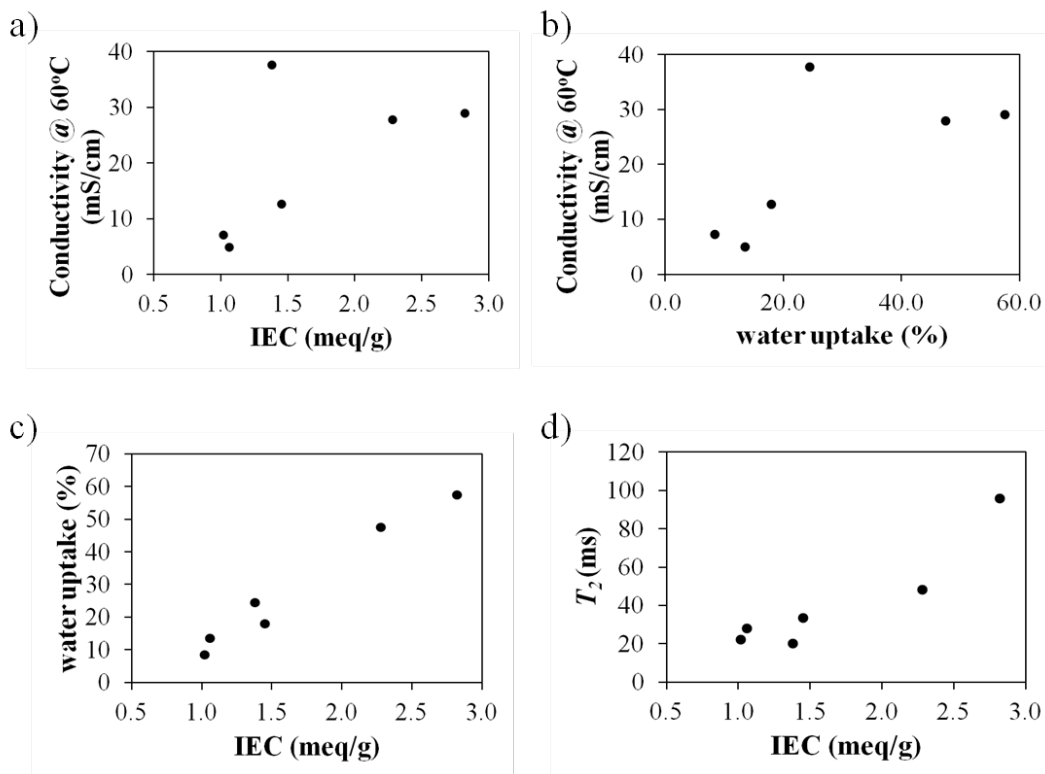


Figure 3.3. (a) Conductivity at 60 °C as a function of IEC, (b) conductivity at 60 °C as a function of water uptake, (c) water uptake as a function of IEC, and (d)  $T_2$  as a function of IEC for the series of mPESs. Data in these plots were extracted in Table 3.1

Figure 3.4 is a schematic diagram explaining the efficient ion/water transport relating the size of hydrophilic blocks and  $T_2$ . First of all, Figure 3.4 (b) indicates that water molecules in the mPES- $X_{6.7}Y_{3.4}$ , which has short  $T_2$ , might be closely interacted with quaternary ammonium groups. Therefore, the utilization of water increases and well-connected ion-transport pathway is developed. Even though water molecules in the mPES- $X_{6.7}Y_{2.5}$  are located close to quaternary ammonium groups, as indicated Figure 3.4 (a), ion transport is not efficient due to scarce ion exchange groups. In the other hands, rich ion exchange groups in mPES- $X_{6.7}Y_{7.7}$  or mPES- $X_{6.7}Y_{11.1}$  do not lead to efficient ion

transport because a fraction of water molecules are not participated in interaction with ion exchange groups, which is judged by long  $T_{2s}$ .

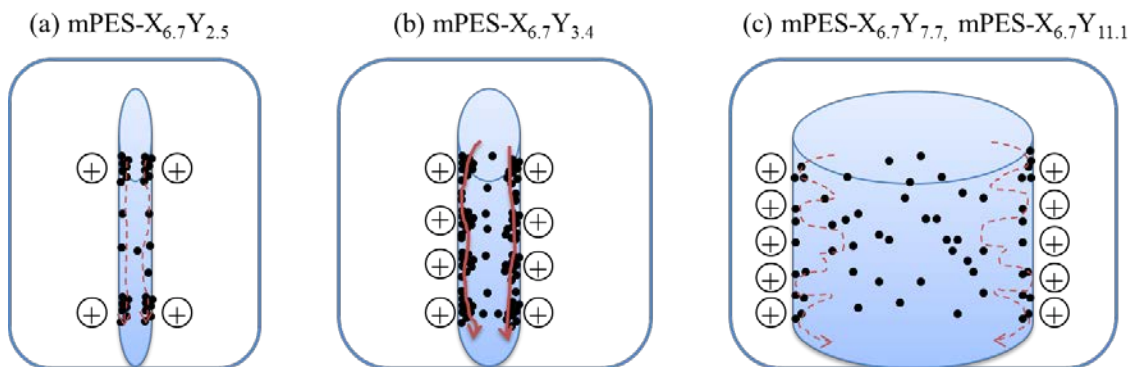


Figure 3.4. Schematic diagram of ion/water transport in (a) mPES- $X_{6.7}Y_{2.5}$  (b) mPES- $X_{6.7}Y_{3.4}$ , and (c) mPES- $X_{6.7}Y_{7.7}$  or mPES- $X_{6.7}Y_{11.1}$ . Block dots,  $\oplus$ , and cylinders represent water molecules, quaternary ammonium cations, and ion channels, respectively.

Based on these analyses, I could hypothesize that increasing hydrophobicity on hydrophobic segments will expand the IEC range being proportional to conductivity. The idea was to create more strongly phase-separated multiblock copolymers to examine whether the channel structure could be made more efficient, and therefore more conductive, for a given IEC and water content. Table 3.2 and Figure 3.5 explain this hypothesis. The linear relationship between IEC and water uptake for mFPESs appears just as shown in the series of mPESs (cf. Figure 3.4 (a)). Higher conductivities of mFPESs than those conductivities of mPESs are observed at similar IECs. (e.g.,  $\sigma = 27.9$  mS/cm for mPES- $X_{6.7}Y_{7.7}$  with IEC = 2.3 meq/g versus  $\sigma = 50.5$  mS/cm for mFPES- $X_{5.6}Y_{9.7}$  with IEC = 2.2 meq/g and  $\sigma = 29.0$  mS/cm for mPES- $X_{6.7}Y_{11.1}$  with IEC = 2.8 meq/g versus  $\sigma = 48.7$  mS/cm for mFPES- $X_{5.6}Y_{14.7}$  with IEC = 3.0 meq/g). One possible

explanation of this observation might be the more distinct phase-separation morphology caused by increased polarity difference in mFPES leads to more efficient water / ion pathway through ion channels even at the longer hydrophilic segments.

Table 3.2. Structural characteristics and properties of a series of mFPESs

(Excerpt from Table 2.1)

	Oligomer Repeat Units (X/Y) <sup>a</sup>	DC <sup>b</sup>	IEC <sup>c</sup>	Water uptake (%)	Conductivity (mS/cm)	
					at 25 °C	at 60 °C
mFPES-X <sub>6.4</sub> Y <sub>4.7</sub>	6.4 / 4.7	2.0	1.7	25.0	17.4	31.4
mFPES-X <sub>5.6</sub> Y <sub>6.0</sub>	5.6 / 6.0	2.0	2.0	48.5	18.5	33.6
mFPES-X <sub>5.6</sub> Y <sub>9.7</sub>	5.6 / 9.7	1.8	2.2	63.0	31.3	50.5
mFPES-X <sub>5.6</sub> Y <sub>14.7</sub>	5.6 / 14.7	2.0	3.0	147	29.2	48.7

Conductivity comparison of mFPESs as a function of IEC demonstrates the similar pattern to that for mPES series, in which conductivity linearly increases as the IEC increased, then reaches to a maximum point at a certain IEC value, and finally levels off at lower value than the maximum. Here, it should be noticed that increased polarity difference between hydrophobic and hydrophilic segments (i.e., mFPESs compared to mPESs) extended the linear relationship regime. In other words, the IEC value of mFPESs that gives rise to the maximum conductivity is higher than that of mPES (IEC = 2.2 meq/g for mFPESs and IEC = 1.4 meq/g for mPESs). I have discussed that expanded hydrophilic ion channels caused by high water uptake and long hydrophilic segments could lead to unproductive interaction of water with ion exchange groups in wider ion channels. This suggests that adding more fluorine atoms to hydrophobic segments keep

the ion channels from significant expanding, and thus it can sustain the nature of efficient utilization of water even at the higher IEC.

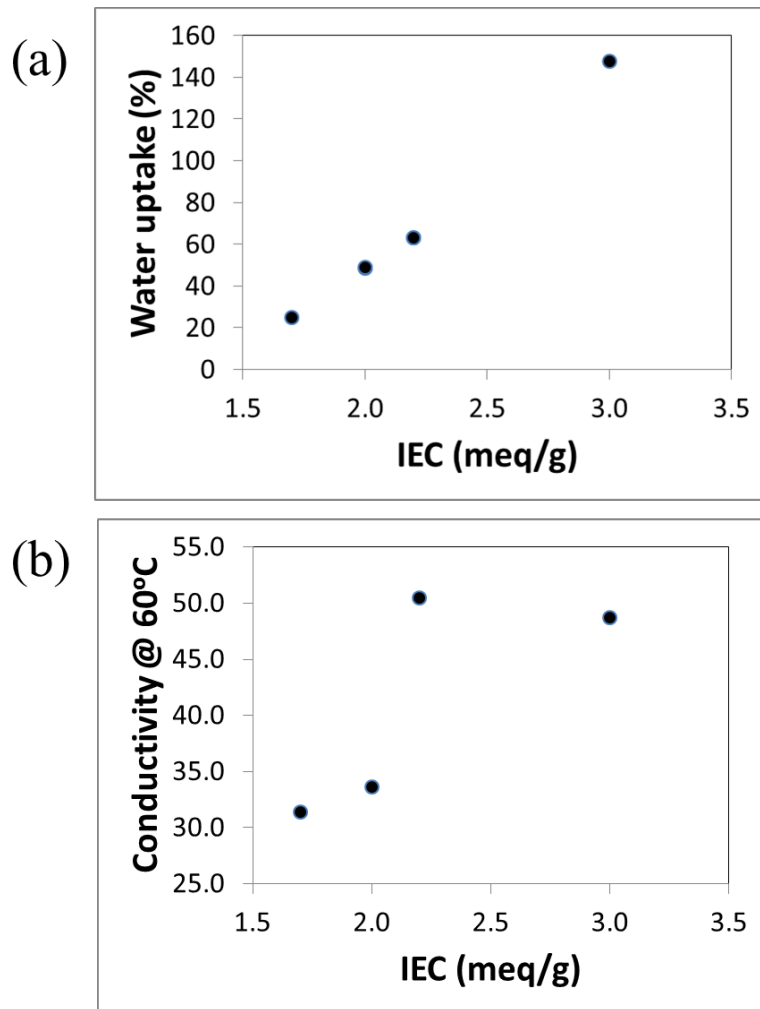


Figure 3.5.(a) Water uptake as a function of IEC, (b) conductivity as a function of IEC for the series of mFPESs. Data in these plots were extracted in Table 3.2

## CHAPTER 4

### DSC STUDY FOR THE CHARACTERIZATION OF VARIOUS WATER STATES IN THE MEMBRANE

#### 4.1. Introduction and Objectives

Water absorbed in an ion exchange membrane is believed to be in three different states: 1) free water that possesses physical characteristics identical to those of bulk water frozen at 0°C, 2) freezable water that is slightly associated with ion exchange groups frozen at subzero temperatures, and 3) non-freezable water that is strongly bound to an ion exchange group or a polar polymer matrix. An understanding of these different states of water is crucial to the operation of polymer electrolyte fuel cells, particularly at high and low temperatures. Since only non-freezable water will remain in the membrane under the dehydrated condition at high / low temperatures (i.e., below 0°C or above 100°C), the cell start-up speed and electrical properties are mainly determined by this state of water.<sup>60, 61</sup> The water state is also a key factor to improve conductivity. Several studies had already been attempted to explain the relationship between the amount of water in different states and ion conductivity or ion mobility.<sup>62, 63</sup> The types of ion transporting mechanisms in the membranes can also be elucidated by studies about the water state because various ion transporting mechanisms are closely related to the proximity of water to the ion exchange groups.

Among other techniques including FT-IR <sup>64</sup>, NMR <sup>30, 65</sup>, and dielectric relaxation spectroscopy <sup>66, 67</sup>, DSC is one of the most efficient and facile techniques for characterizing the various states of water. In this study, I utilized this technique to interpret the conductivity data of mFPES as a function of the amount of freezable water and reveal a dominant ion transporting mechanism for anion conductive mFPES systems.

## 4.2. Experimental Details

DSC measurements were carried out on DSC Q200 of a TA instrument. Membrane samples were fully-hydrated by soaking them in deionized water at least for one week before measurements. After the water on the membrane surface was wiped off with absorbent wipers, 3-5mg of the membrane was quickly sealed in an aluminum pan. The sealed pan containing the sample and an empty reference pan were placed in a DSC cell, cooled down from 25°C to -70°C at a rate of 5°C, and heated up 25°C at the same rate under N<sub>2</sub> flow (20ml/min). The quantities of freezable and non-freezable water were determined by the following equations. <sup>34, 68</sup> The total number of water molecules per quaternary ammonium group was calculated by the gravimetric data of the sample using Equation 4.1.

$$\lambda = \frac{M_w - M_d}{18M_d} \times \frac{1}{IEC} , \quad (4.1) ,$$

where  $M_w$  is the mass of the wet sample and  $M_d$  is the mass of the dry sample. The ratio between the mass of the freezable water and  $\lambda$  enable estimation of the number of freezable water molecules as shown in Equation 4.2.

$$N_{fre} = \frac{M_{fre}}{M_{tot}} \times \lambda, \quad (4.2),$$

where  $M_{fre}$  is the mass of the freezable water and  $M_{tot}$  is the total mass of water absorbed in the membrane. Here, the value of freezing temperature drop and enthalpy of water freezing has to be involved in the following Equation 4.3 to determine the weight fraction of freezable water.

$$\frac{M_{fre}}{M_{tot}} = \frac{H_f / H_{ice}}{(M_w - M_d) / M_w}, \quad (4.3),$$

where  $H_f$  is enthalpy obtained by the integration of the DSC freezing peak and  $H_{ice}$  is enthalpy of freezing water, corrected for the subzero freezing point according to Equation 4.4.

$$\begin{aligned} H_{ice} &= H^o - \Delta C_p \Delta T_f, \\ H^o &= 333.8 J / g \end{aligned}, \quad (4.4),$$

where  $\Delta C_p$  is the difference between specific heat capacity of liquid water and that of ice,  $\Delta T_f$  is the freezing point depression.

### 4.3. Results and Discussion

The investigation of water states in a series of mFPES membranes was performed using DSC. Figure 4.1 shows the DSC thermograms of selected mFPESs. The increased integral of the freezing peak was observed as water uptake increased, which suggests that the amount of freezable water increases. In contrast, the higher water uptake leads to the lower freezing temperature depression. This observation implies that augmented

hydrophilic channels caused by a significant amount of water loosen the association of water to quaternary ammonium groups or the polymer matrix. The number of water molecules per cation exchange group, the depression freezing temperature, and the quantities of freezable and non-freezable water are summarized in Table 4.1.

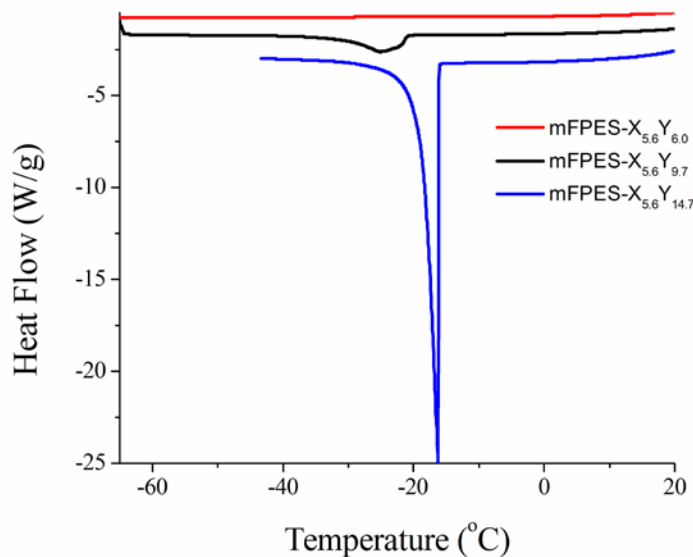


Figure 4.1. DSC thermograms of mFPESs containing different hydrophilic segment at the same length of hydrophobic segment.

As shown in Table 4.1, the comparison of multiblock copolymers with different lengths of the hydrophilic segments but containing the same size of hydrophobic segments suggested that the samples exhibited a similar number of non-freezable water molecules regardless of water uptake (i.e.,  $N_{\text{non}} = 12.8$  for mFPES- $X_{5.6}Y_{6.0}$ ,  $N_{\text{non}} = 12.3$  for mFPES- $X_{5.6}Y_{9.7}$ , and  $N_{\text{non}} = 13.9$  for mFPES- $X_{5.6}Y_{14.7}$ ). Since non-freezable water is considered as water that hydrates the ion exchange group of the membrane, a certain number of water molecules volume fraction of polymer may need to hydrate the quaternary ammonium groups in the polymer membrane. It should be noticed that the

majority of the absorbed water was non-freezable in most cases. This result suggests that water tends to hydrate the polymer first when the membrane is soaked in water.

I prepared the two sets of membranes with the same IEC and therefore the same water uptake, but different lengths of segments (i.e., mFPES- $X_{5.6}Y_{6.0}$  versus mFPES- $X_{4.8}Y_{6.0}$  and mFPES- $X_{5.6}Y_{9.7}$  versus mFPES- $X_{3.5}Y_{4.7}$ ), which showed very different conductivities. These results were unusual in that the same water uptake and IEC generally produce the same conductivity for ion conductive polymer membranes. Studies pertaining to water states provided insight into the interpretation of these curious observations.

Table 4.1 The quantity of non-freezable and freezable water molecules relating to IEC and water uptake in mFPES membranes.

	IEC <sup>c</sup>	Water uptake (%)	$\lambda$	$N_{non}$	$N_{fre}/N_{non}$ (%)	Conductivity (mS/cm) at 60 °C
mFPES- $X_{6.4}Y_{4.7}$	1.7	25.0	8.2	8.0	2.5	31.4
mFPES- $X_{5.6}Y_{6.0}$	2.0	48.5	13.5	12.8	5.2	33.6
mFPES- $X_{4.8}Y_{6.0}$	2.0	49.0	13.6	12.3	10.7	43.5
mFPES- $X_{5.6}Y_{9.7}$	2.2	63.0	15.9	12.3	28.7	50.5
mFPES- $X_{3.5}Y_{4.7}$	2.2	63.0	15.9	15.5	2.7	36.8
mFPES- $X_{5.6}Y_{14.7}$	3.0	147	27.3	13.9	97.4	48.7

Table 4.1 and Figure 4.2 demonstrate that conductivity and  $N_{\text{fre}} / N_{\text{non}}$  appear to have a linear relationship at a lower IEC than 2.2 meq/g, which could indicate that freezable water offers an additional contribution to improving conductivity. However, conductivity does not increase at higher IEC than 2.2 meq/g. This tendency is analogous to that shown in Figure 3.3 (b). Both can be explained by the possible detrimental impact of extra water beyond necessity, as discussed in Chapter 3. The observation that relatively high conductivity appeared even in the membrane with almost no freezable water (e.g.,  $\sigma = 31.4$  mS/cm for mFPES- $X_{6.4}Y_{4.7}$  and  $\sigma = 36.8$  mS/cm for mFPES- $X_{3.5}Y_{4.7}$ ) implies the dominant ion transport may occur extremely close to the ion exchange group through the assistance of non-freezable water.

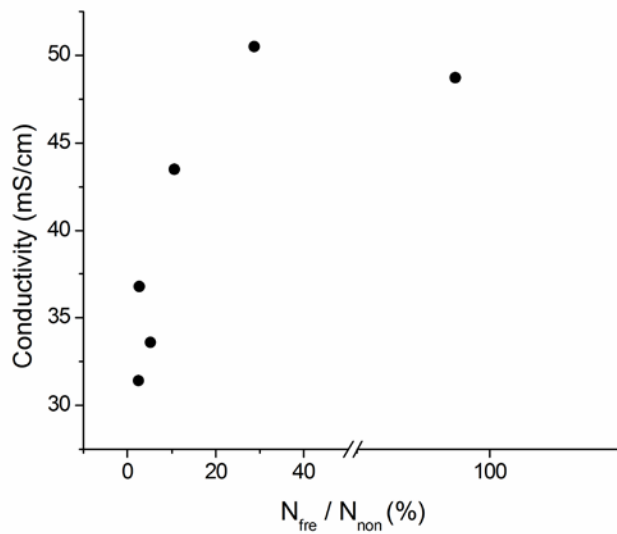


Figure 4.2. Conductivity as a function of  $N_{\text{fre}} / N_{\text{non}}$  for mFPES membranes.

## CHAPTER 5

### THE STUDY OF DIFFUSION ACTIVATION ENERGY FOR EXPLORING ANION TRANSPORTING MECHANISMS

#### 5.1. Introduction and Objectives

Unraveling the mystery of ion transport dynamics and mechanisms in the ion conductive polymer membrane requires an understanding of the hierarchical information of polymer morphology and structure (i.e., from molecular interaction on the scale of sub nanometers to phase segregation on the scale of micrometers). The very fundamental processes of ion transportation which occur on the sub-nanometer scale can be revealed by the activation energy  $E_a$  of diffusion.<sup>69</sup> The activation energy is calculated by the Arrhenius equation (Equation 5.1):

$$D(T) = D_0 e^{-E_a / RT}, \quad (5.1)$$

where  $D(T)$  is a diffusion coefficient as a function of temperature,  $D_0$  is a pre-exponential constant representing the diffusion coefficient at infinite temperature, and  $R$  is the gas constant. The  $E_a$  and  $D_0$ , obtained by the diffusion coefficient measurement, which depends on the temperature, provide important physical meaning relating to the ion transportation mechanisms. Intensive studies on proton transport mechanisms generally agree that three major types of proton transfer take place in proton conductive polymer membranes: the vehicle mechanism through which protons are transported by diffusion

or convection, the Grotthuss mechanism through which the protons are transferred between adjacent water molecules in a hopping manner induced by the exchange of hydrogen bonding, and surface hopping that represents proton hopping between two adjacent sulfonate groups on the polymer matrix. In most proton conductive membranes, the relative predominance of each mechanism strongly depends on water uptake. Eikerling et al. classified the proton conduction mechanism into surface and bulk mechanisms.<sup>70</sup> The surface mechanism, the proton-transporting mechanism at low water content, is characterized by high activation energy and thus low mobility. The larger channel size in the membrane created at high water uptake enable water to reside and move through the bulk, where it has lower activation energy. As water uptake increases, ion/water has increased mobility according to the different mechanisms and the overall activation energy should decrease to an asymptotic point. Therefore, the activation energy could be an indicator of the ion-conducting mechanism in the membranes. Merinov et al.<sup>71</sup> employed the diffusion coefficient and corresponding activation energy obtained from molecular dynamics simulations to explain the possible mechanisms of hydroxide transport in a quaternized aromatic polysulfone. They proposed the OH-diffusion probably combines both the vehicle and the Grotthuss-type proton diffusion mechanisms.

This section of the thesis aims at exploring hydroxide transportation processes relating to water uptake, the IEC, and the lengths of hydrophilic segments for fluorinated multiblock copolymers (mFPES series) using the activation energy of diffusion. For comparison, I also measure the activation energy of pure water. In the previous section, I suggested that predominant ion/water transportation at low hydration condition takes

place near a polymer matrix using low-temperature DSC measurement. The investigation of the activation energy of diffusion will partially support the suggestion.

## 5.2. Experimental Details

The membrane samples (mFPES-X<sub>5.6</sub>Y<sub>6.0</sub>, mFPES-X<sub>5.6</sub>Y<sub>9.7</sub>, and mFPES-X<sub>5.6</sub>Y<sub>14.7</sub>) of 3 × 10 mm strips were fully hydrated by soaking them in deionized water before measurements. After water on the polymer surface was removed, the hydrated membrane samples were quickly placed in a 5 mm NMR tube and wet Kimwipes covered the top of the tube to maintain a fully hydrated condition. All NMR measurements were carried out using a Bruker AV-3 400MHz NMR instrument equipped with a diffusion probe. The pulsed-gradient stimulated echo sequence with a gradient pulse length ( $\delta$ ) of 1.4ms and a diffusion time ( $\Delta$ ) of 20 or 50 ms was used to measure the diffusion coefficients. Gradient strengths were incremented in 24 steps and the number of scans was 8. The diffusion coefficients ( $D$ ) were calculated by fitting the signal intensity ( $I$ ) decay along with the incrementing gradient field ( $g$ ) according to the following equation<sup>72</sup> :

$$I = I_o \exp(-D\gamma^2 g^2 \delta^2 (\Delta - \delta/3)) = I_o \exp(-Db) , \quad (5.2)$$

where  $\gamma$  is the magnetogyric ratio of proton. The signal intensities followed mono-exponential fitting indicating water in all samples has a single diffusion coefficient.

The activation energy of diffusion was obtained by fitting the diffusion coefficients as a function of temperature from 20°C to 40°C in an interval of 5°C according to Equation 5.1. The sample was equilibrated for 30 min at each temperature under minimum flowing of air (170 L/h) for avoiding possible errors caused by vibration.

### 5.3. Results and Discussion

The investigation of the activation energy for a series of multiblock copolymer membranes (i.e., mFPES- $X_{5.6}Y_{6.0}$ , mFPES- $X_{5.6}Y_{9.7}$ , and mFPES- $X_{5.6}Y_{14.7}$ ) was carried out using the measurements of diffusion coefficients as a function of temperature. Figure 5.1 shows the plots of the diffusion coefficients as a function of temperature to obtain the activation energy and Figure 5.2 shows representative diffusion plots for corresponding membrane samples and water at 25°C.

As discussed in Chapter 4, the low-temperature DSC measurement revealed that water in the membranes has different states (i.e., freezable water and non-freezable water), which implied that two different diffusion coefficients were expected. However, all diffusion plots exhibited mono-exponential decay indicating water in the membranes has a single diffusion coefficient. This discrepancy can be resolved by the fact that water rapidly exchanged from one physical state to the other at the temperature range (i.e., 20°C to 40°C) during the diffusion times (20ms or 50ms). As shown in Figure 5.1, the diffusion rates of water in the mFPES- $X_{5.6}Y_{6.0}$ , mFPES- $X_{5.6}Y_{9.7}$  were approximately 10 times slower than that of bulk water. And, the diffusion rate of water in mFPES- $X_{5.6}Y_{14.7}$  was faster than that in mFPES- $X_{5.6}Y_{6.0}$  and mFPES- $X_{5.6}Y_{9.7}$ , but slower than that of bulk water. As I take into account of the observation that most of water in mFPES- $X_{5.6}Y_{6.0}$  and mFPES- $X_{5.6}Y_{9.7}$  was non-freezable water (Table 4.1), the diffusion coefficients from measurements for mFPES- $X_{5.6}Y_{6.0}$  and mFPES- $X_{5.6}Y_{9.7}$  might represent the diffusion behavior of non-freezable or bound water. The diffusion coefficient appeared in mFPES- $X_{5.6}Y_{14.7}$  suggested that the water molecules in the bound state and the bulk-like state rapidly exchange.

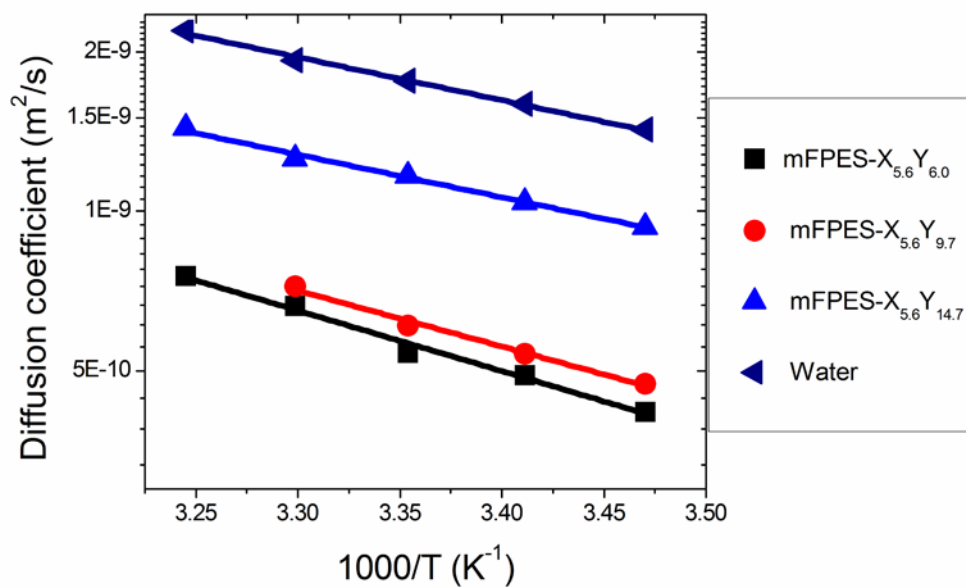


Figure 5.1. Plot of diffusion coefficients as a function of temperature for obtaining the activation energy

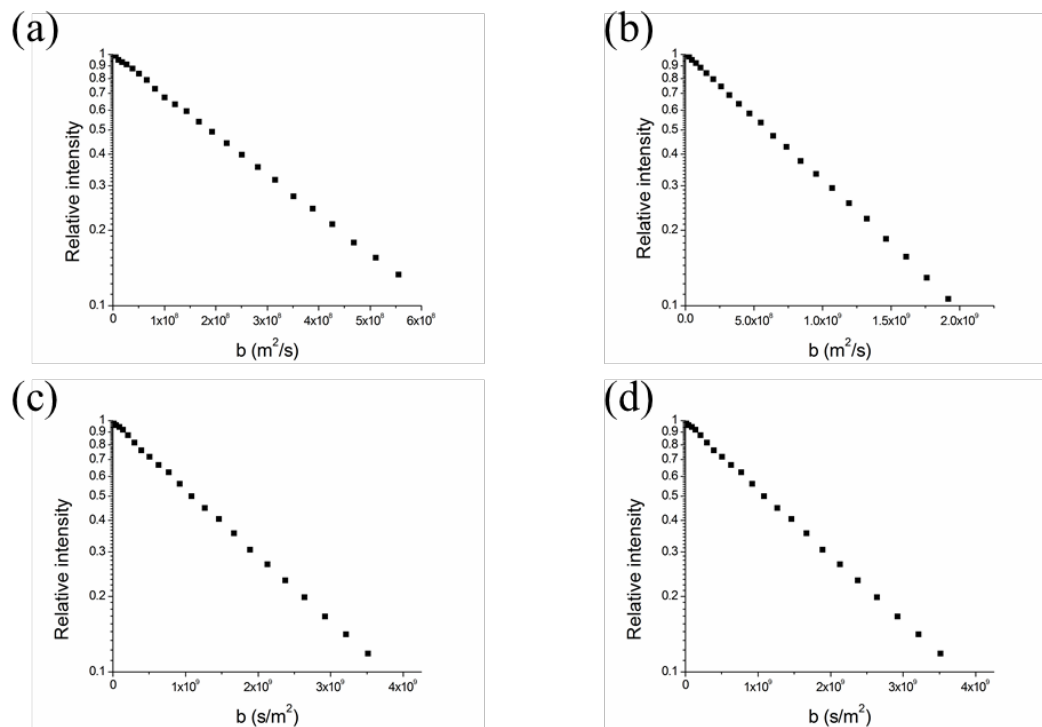


Figure 5.2. Plot of intensity decay as a function of gradient strengths for determining diffusion coefficient of water in (a) bulk, (b) mFPES-X<sub>5.6</sub>Y<sub>14.7</sub>, (c) mFPES-X<sub>5.6</sub>Y<sub>9.7</sub>, and (d) mFPES-X<sub>5.6</sub>Y<sub>6.0</sub>.

$$b = \gamma^2 g^2 \delta^2 (\Delta - \delta/3) \text{ in Equation 5.2}$$

Table 5.1 summarizes the activation energy ( $E_a$ ) for the membranes and bulk water. As the lengths of hydrophilic segments and water uptake increased, the activation energy decreased. This observation suggested that local energetics and transporting processes of water changed as a function of the ion-channel size and water uptake. Specifically, the water in the mFPES-X<sub>5.6</sub>Y<sub>6.0</sub> (i.e., the sample of low water uptake) might be transported close to the surface because it has high activation energy. As indicated in Table 4.1, 95% of water in the mFPES-X<sub>5.6</sub>Y<sub>6.0</sub> is non-freezable or bound water, which is located in proximity to the surface of the polymer. This supported that the water

transporting mechanism might take place in the surface in which bound water is predominantly involved. By contrast, the water in the mFPES- $X_{5.6}Y_{14.7}$  (i.e., the sample of high water uptake) has almost the same activation energy as bulk water. This observation might demonstrate that the water in mFPES- $X_{5.6}Y_{14.7}$  is transported through the vehicle or the Grotthus mechanism in which free water is mainly involved.

Table 5.1 The activation energy and conductivity of diffusion for the membranes and bulk water

	$E_a$ (kJ/mol)	Water uptake (%)	Conductivity at 60°C (mS/cm)
mFPES- $X_{5.6}Y_{6.0}$	22.2	48.5	33.6
mFPES- $X_{5.6}Y_{9.7}$	20.6	63.0	50.5
mFPES- $X_{5.6}Y_{14.7}$	15.5	147	48.7
Bulk water	15.7	-	-

I have not reached the distinct conclusion about the correlation of the activation energy and conductivity. The mFPES- $X_{5.6}Y_{9.7}$  sample with the activation energy in between that of mFPES- $X_{5.6}Y_{6.0}$  and mFPES- $X_{5.6}Y_{14.7}$  has the highest conductivity. This observation could be a result of adding the contribution of the transport on the surface and that on bulk. Even though the activation energy of diffusion provide valuable information of local energetics of water in the membrane, it is not enough to fully reveal the types of hydroxide transporting mechanisms such as surface-hopping, vehicle, and Grotthus mechanisms. In order to investigate the mechanisms, I need supporting information such as the computation of activation energy for each mechanism, the

estimation of the number of water molecules passing through the membrane, and the conducting performance relating to the different mechanisms.

# CHAPTER 6

## QUANTITATIVE CHEMICAL STABILITY TEST FOR ANION CONDUCTIVE MEMBRANE WITH $^1\text{H}$ AND DIFFUSION- ORDERED NMR SPECTROSCOPY

### 6.1. Introduction and Objectives

The chemical stability at high pH and high temperature is believed to be a key issue to broaden the usage of anion exchange membranes (AEMs) in various devices. Specifically, durable AEMs for anion exchange membrane fuel cells (AEMFCs) are a prerequisite to long-term operation of the cells. Recent studies presented several characterization techniques to determine chemical stability including time-dependent conductivity measurements <sup>73</sup>, FT-Raman <sup>74</sup>, FT-IR <sup>37</sup>, GPC <sup>37</sup>, and  $^1\text{H}$  NMR <sup>75, 76</sup>. Most of the research has been focusing on monitoring an ion exchange capacity (IEC) or conductivity as a function of time while an AEM is treated with a concentrated alkaline solution at elevated temperatures. These approaches are based on the assumption that a change in the IEC and conductivity represents the chemical stability of AEMs. However, this assumption suffers from the possibility that hydroxide ions have a tendency of converting to carbonate or bicarbonate ions in the presence of air.<sup>38</sup> In addition, quantitative chemical analysis and the detail degradation mechanism or kinetics cannot be revealed by this method.<sup>77</sup>

This section of the thesis aims at introducing the quantitative and *in-situ* characterization method using automated  $^1\text{H}$  NMR measurements as well as diffusion-ordered NMR spectroscopy (DOSY) for investigating the chemical stability of the synthesized polymers. I chose two types of poly (arylether sulfone)s based multiblock copolymers and poly (arylene ether)s with two different ion exchange groups: quaternary ammoniums and quinuclidines. These comparisons offered insight into the degradation mechanism of AEMs.

DOSY, two dimensional NMR spectroscopy in which diffusion coefficients of each proton with respect to a chemical shift, is employed to demonstrate the degradation processes.<sup>78</sup> This technique can be considered as a special chromatographic technique for separating a mixture based on diffusion coefficients relating to size and shape of molecules or physical properties of surrounding such as temperature, viscosity, etc. The measurement of diffusion coefficients is carried out using pulse-field gradient experiments. A series of one-dimensional  $^1\text{H}$  spectra are collected as a function of the gradient field strength and the relative intensity of each peak in the spectra is monitored. The decay rate of the relative intensity is proportional to the diffusion coefficient. All signals corresponding to a certain molecule are subject to have the same diffusion coefficients, which makes all cross peaks in the DOSY spectrum located in the same line along the diffusion coefficient axis.

DOSY measurements provided valuable information about the degradation of the AEMs because the products resulted from degradation should have a different diffusion coefficient from that of starting materials. DOSY also enabled distinguishing peaks

according to the polymer from peaks according to the solvents, which reveals the accurate chemical structure information.

## **6.2. Experimental Details**

### **6.2.1. Materials**

The detail preparation procedure of the multiblock arylene ether sulfone copolymer, QmPES- $X_{6.7}Y_{7.7}$  and the fluorinated arylene ether sulfone multiblock copolymer, QmFPES- $X_{6.4}Y_{4.7}$  is presented in Chapter 2. Anion conductive poly (arylene ether)s, PAE-Q and PAE-N, (Figure 6.1) are obtained from the Kohl's group, and synthetic procedure has been reported.<sup>79</sup>

### **6.2.2 Measurements**

A standard condition for a chemical stability test is set up for an accelerated degradation study. DMSO / KOH in MeOD- $d_3$  co-solvent system was chosen for homogeneous alkaline solution of the all samples. 30 mg of selected chloride form of AEMs (QmPES- $X_{6.7}Y_{7.7}$ , QmFPES- $X_{6.4}Y_{4.7}$ , PAE-Q, and PAE-N) were dissolved in 260mg of DMSO- $d_6$  until the clear polymer solution was obtained. 130mg of 2 M KOH in MeOD- $d_3$  solution is added to the polymer solution. The resulting sample solution was immediately transferred to a 5mm NMR tube and put it into a NMR spectrometer that was already set at 60°C.

Automated acquisition of  $^1\text{H}$  NMR at a designed time interval (1 min to 557 min) using a Bruker Avance-III 400 MHz NMR spectrometer was performed with a delay time of 5 s. The time between sample preparation and NMR measurements was minimized and the first acquisition started almost exactly after 5 min for all samples. The monitored integral of polymer peaks' area with respect to the integral of DMSO peak (internal standard) was used for determining the rate of degradation.

Diffusion ordered NMR spectroscopy (DOSY) was conducted at 23 °C using 5-mm NMR tubes on a Bruker AV3 400 operating at 400 MHz. All DOSY spectra were collected using a pulse gradient stimulated echo sequence. For the pulse sequence, gradients were applied for 1 ms ( $\delta$ ), and the diffusion time ( $\Delta$ ) was 30 ms. The delay between each scan was 1 s and the number of scans was 32. The gradients were incremented from 5.0 to 668.4 G/cm, which enabled the final intensity of each peak to be less than 10% of its original intensity. Consequently, 32 free induction decays containing 4k data points were collected. The DOSY spectra were constructed based on the assumption that the intensity trends of all chemical shifts over the gradients followed bi-exponential decays since the diffusion coefficient of the polymer is significantly different from those of solvents and small molecules generated by degradation processes.

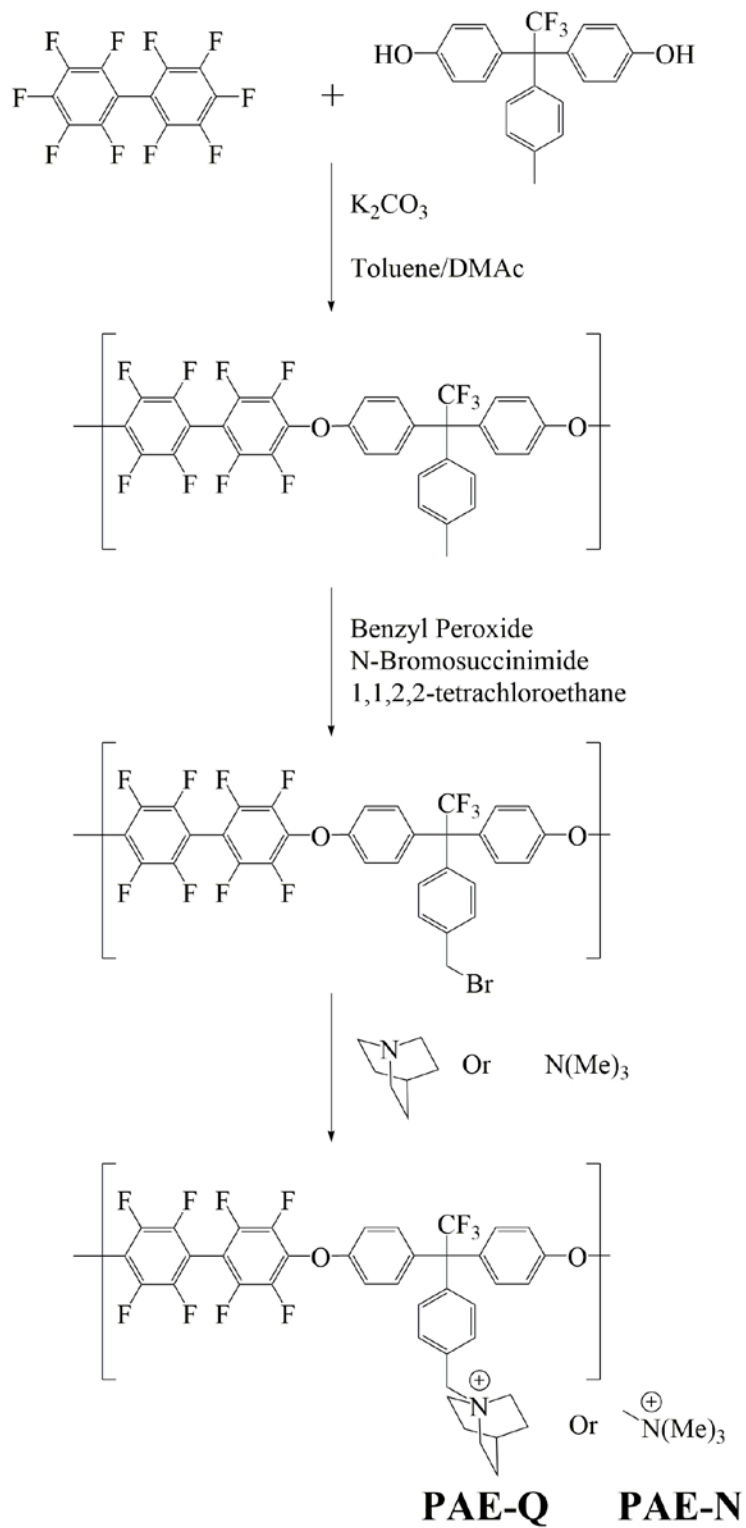
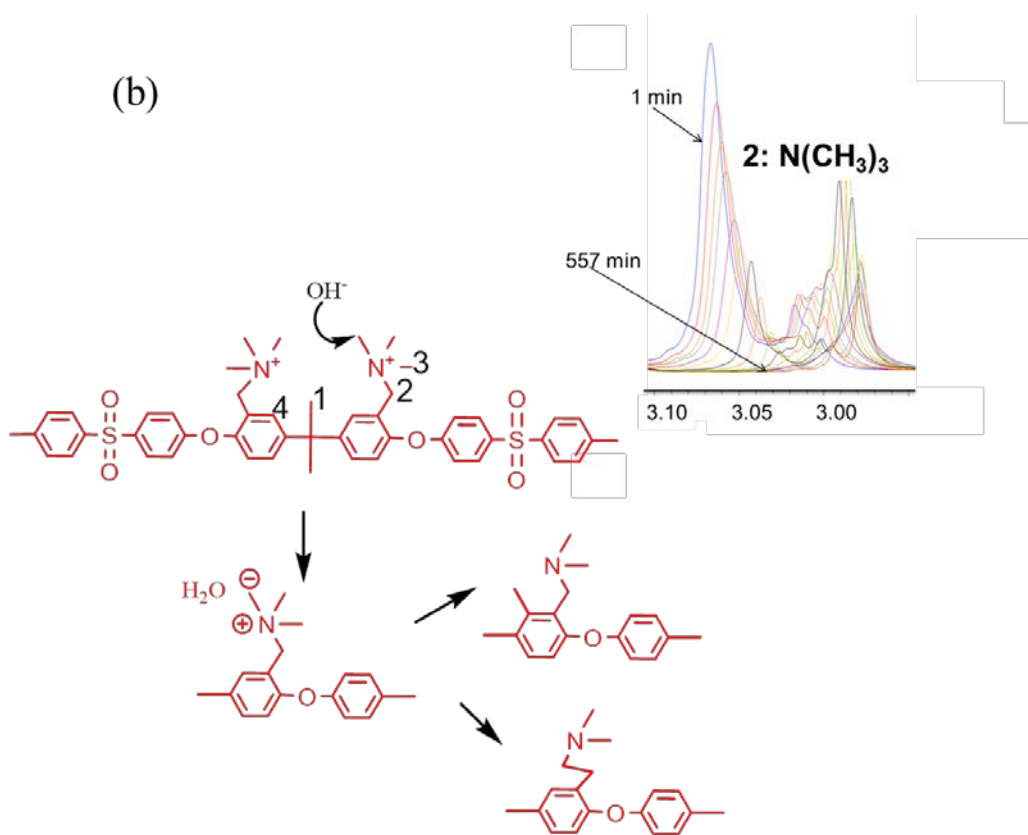
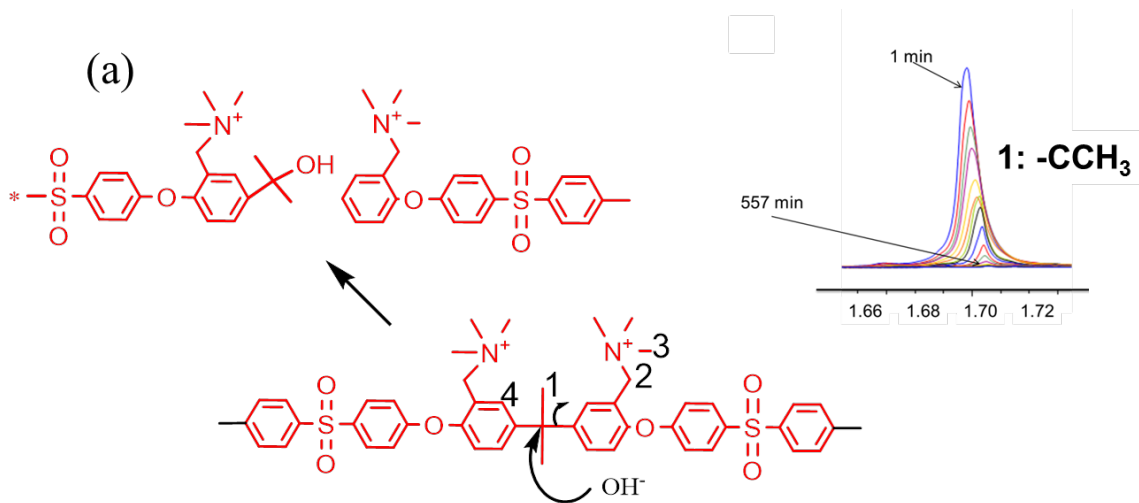


Figure 6.1 Synthetic scheme for selected poly(arylene ether)s as model materials.

### 6.3. Results and Discussion

Under the standard test condition, backbone and ion exchange group degradation was analyzed. Figure 6.2 shows a stack of overlaid  $^1\text{H}$  spectra for the QmPES- $X_{6.7}Y_{7.7}$  as a function time at each chemical shift region and corresponding degradation mechanisms that might be happened. As indicated in Figure 6.2 (a) and (d), the peaks at 1.7 ppm and 7.5 ppm, which are corresponded to the dimethyl protons of BPA units and aromatic proton at the meta position to oxygen of BPA units respectively, decayed away. For these to occur, methoxides or hydroxides might attack the quaternary carbon of BPA and tertiary alcohols are generated.<sup>80</sup> This degradation leads to the change of chemical shifts of peaks at 1.7 ppm and 7.5 ppm. Figure 6.2 (b) depicts that the peak intensity of trimethyl protons of quaternary ammonium groups (3.1 ppm) decreases due to the direct attack of methoxides or hydroxides to trimethyl groups. Degradation of benzyl groups due to de-protonation followed by ylide formation and the rearrangement of a methyl group or de-quaternization is shown in Figure 6.2 (c). Chemical shift movements toward low-field were also observed, which can be explained by the strength change of hydrogen bonding.<sup>81</sup> Figure 6.2 (b) and Figure 6.2 (c) revealed the new peaks are also generated, which are believed to be the product caused by degradation. Substitution of methoxide (i.e.,  $\text{MeO}^-$ ) to benzyl groups may lead to arise the peaks at 4.40-4.45 ppm and 2.95-3.02 ppm according to benzylmethyl ether (i.e.,  $-\text{CH}_2\text{OCH}_3$ ).<sup>75, 82</sup> In addition, the new peak at 2.2 ppm after degradation could be corresponded to detached trimethyl ammonium groups.



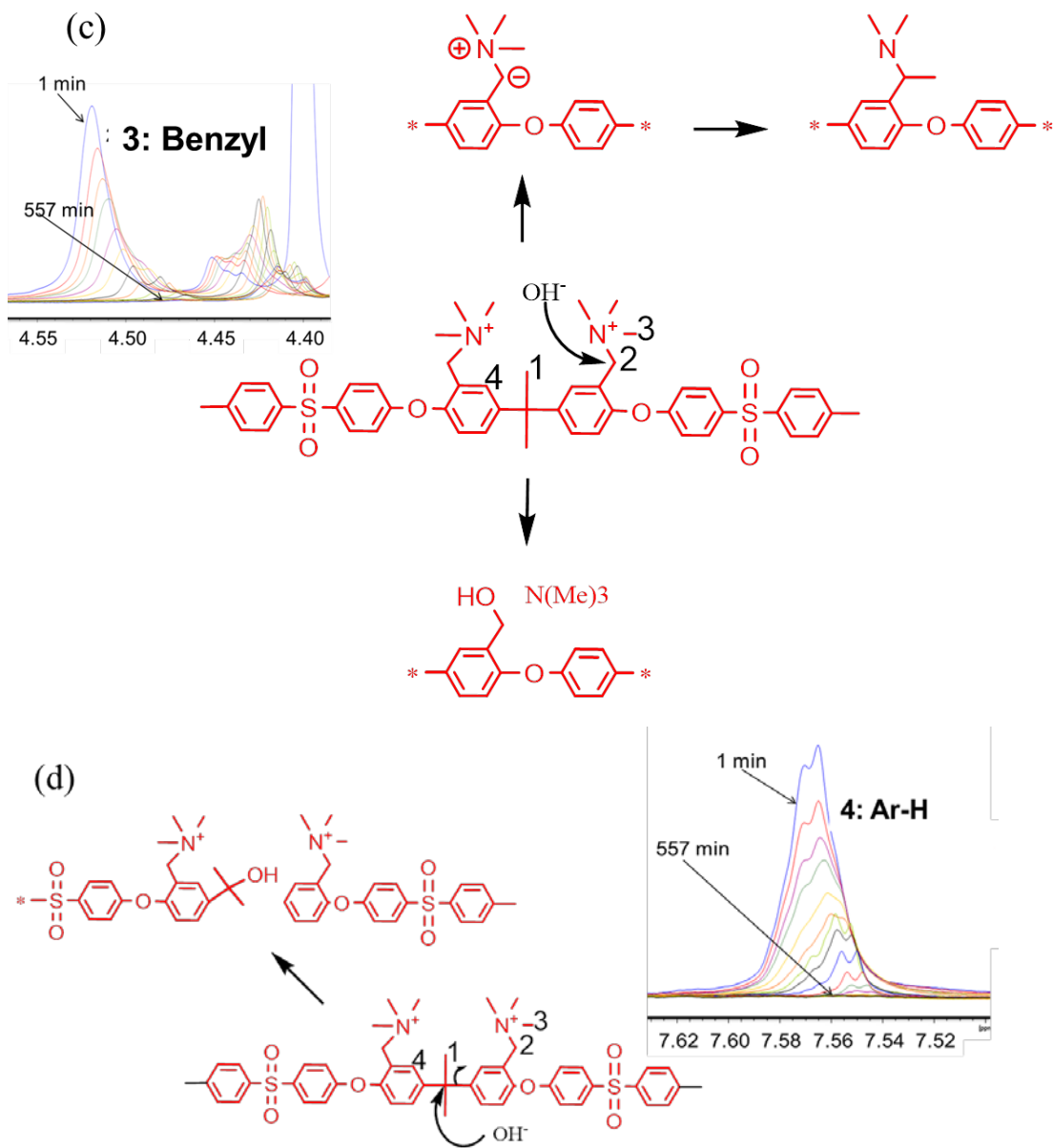


Figure 6.2. Stack of overlaid  $^1\text{H}$  spectra of (a) the region of 1.7 ppm, (b) the region of 3.1 ppm, (c) the region of 4.5 ppm, and (d) the region of 7.5 ppm in QmPES- $\text{X}_{6.7}\text{Y}_{7.7}$  under the standard test condition and corresponding degrading mechanisms.

Further quantitative analysis was made by tracking the integral of each peak (i.e., 7.57 ppm, 4.53 ppm, 3.07 ppm, and 1.70 ppm) with respect to the integral of internal

standard (i.e., the peak at 2.5 ppm corresponding to DMSO). As shown in Figure 6.3, the relative degradation rate of the peak at 7.57 ppm and the peak at 1.70 ppm was almost identical. This observation could be interpreted by two possible explanations: 1) Polymer backbone degradation by the cleavage of the aromatic carbon-oxygen bonds occurred along with degradation of quaternary ammonium groups and 2) the decay of trimethyl ammonium groups without backbone degradation leads to changes the chemical shift of aromatic protons. The comparison of DOSY spectra of the QmPES- $X_{6.7}Y_{7.7}$  solution of DMSO- $d_6$  / MeOD- $d_3$  in the presence of aq. KOH and in the absence of aq. KOH offered a clue to understand polymer backbone stability. (Figure 6.4)

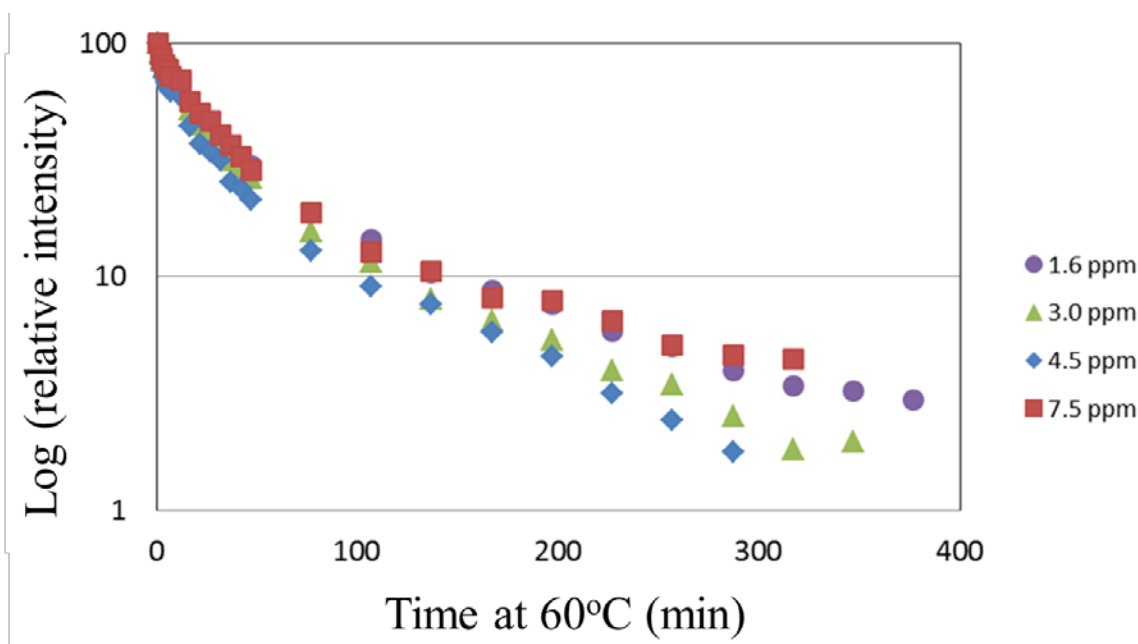


Figure 6.3. Log (relative intensity) plot of each peak in QmPES- $X_{6.7}Y_{7.7}$  with respect to time at 60°C showing relative degradation rates.

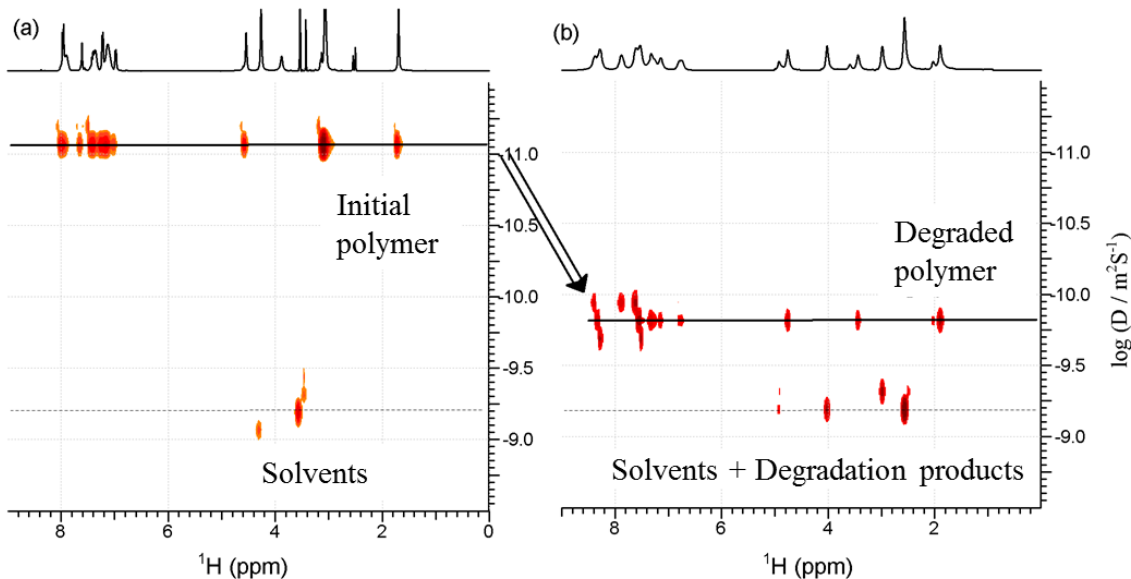


Figure 6.4. DOSY spectra (a) of QmPES- $X_{6.7}Y_{7.7}$  DMSO- $D_6$  / MeOD- $d_3$  without KOH and (b) of QmPES- $X_{6.7}Y_{7.7}$  DMSO- $D_6$  / MeOD- $d_3$  with KOH after 557 min at 60°C.

Figure 6.4 clearly demonstrates that the diffusion coefficients of the peaks according to the polymer significantly decreased after degradation under hot alkaline condition ( $\log D = -11.2$  to  $-9.85$   $m^2/s$ ), which implied that scissoring aromatic C-O bonds and/or the bond between quaternary carbons and aromatic carbons in BPA unit also occurred along with detaching the quaternary ammonium groups. Although all protons ended up exhibiting the same diffusion coefficients after degradation for 557 min (Figure 6.4 (b)), degradation kinetics of each protons were not identical. As shown in Figure 6.3, decay rate of bezyltrimethyl ammonium moiety (3.0 and 4.5 ppm region) is faster than that of arylene ether moiety (1.6 and 7.5 ppm).

The comparison of four different samples, QmPES- $X_{6.7}Y_{7.7}$ , QmFPES- $X_{6.4}Y_{4.7}$ , PAE-Q, and PAE-N, in terms of chemical stability was attempted by monitoring the disappearance of the peak corresponding to the bezyltrimethyl ammonium groups. Table 6.1 and Figure 6.5 show that the percentage of remaining bezyltrimethyl ammonium

groups of each sample as a function of time under the standard test condition. As demonstrated in Figure 6.5, four selected AEMs exhibited remarkably different chemical stability under the standard test condition. This discrepancy seemed to stem mainly from the different chemical characteristics of the polymers. The polymers based on the arylene ether sulfones (i.e., QmPES- $X_{6.7}Y_{7.7}$  and QmFPES- $X_{6.4}Y_{4.7}$ ) showed lower chemical stability than the poly (arylene ether)s (i.e., PAE-Q and PAE-N). I believe that electron-withdrawing character of the sulfone groups may increase the electrophilicity of the benzyl position of benzyltrimethyl ammonium groups and thus this position became more vulnerable to the nucleophile attack of methoxides.

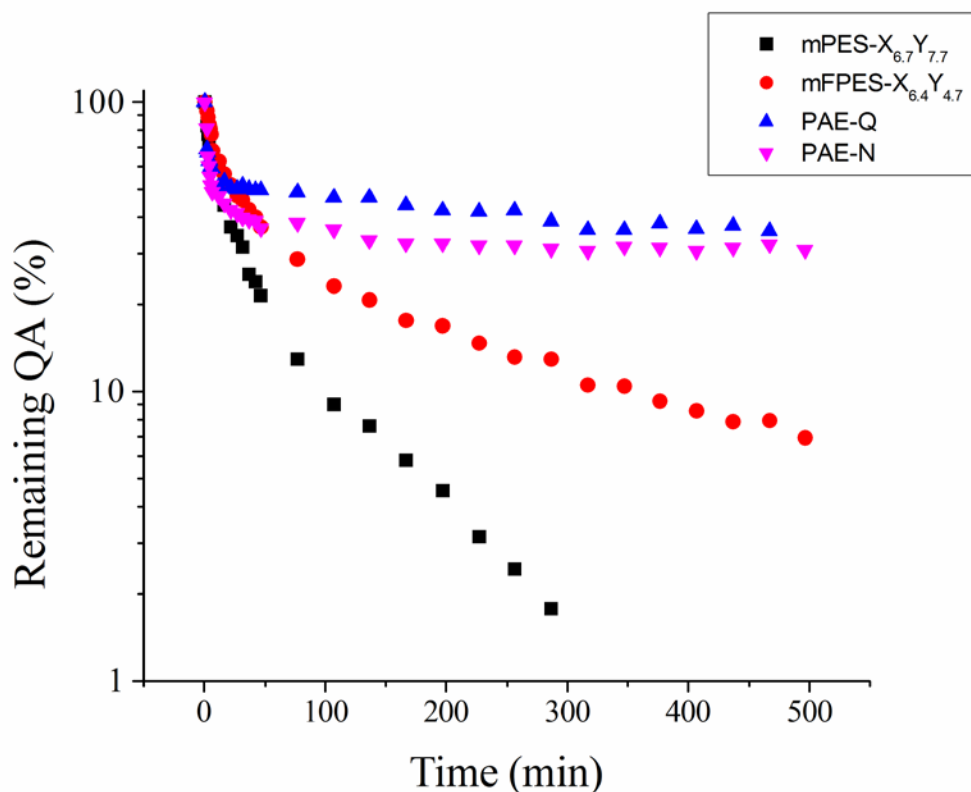


Figure 6.5 Plot of remaining benzyltrimethyl ammonium groups in selected four samples (QmPES-X<sub>6.7</sub>Y<sub>7.7</sub>, QmFPES-X<sub>6.4</sub>Y<sub>4.7</sub>, PAE-Q, and PAE-N) as a function of time. (The raw data is given in Table 6.1 and remaining benzyltrimethyl ammonium groups is estimated by monitoring the integral of benzylic protons with respect to internal standard as a function of time)

The hydrophobicity of the polymer also may influence on the chemical stability. As shown in Figure 6.5, the multiblock copolymer with additional fluorine groups (QmFPES-X<sub>6.4</sub>Y<sub>4.7</sub>) had better durability than the multiblock copolymer without fluorines on aromatic rings (QmPES-X<sub>6.7</sub>Y<sub>7.7</sub>). This tendency might be explained by the steric hindrance effects of fluorine groups located on the proximity of the benzylic methylene position. Further investigations are necessary to prove this rationale. Unlike the polymer backbone structures and hydrophobicity, different ion exchange groups (i.e.,

quinuclidines versus quaternary ammoniums) did not impact considerably on the chemical stability under the standard test condition. The comparison between PAE-Q and PAE-N, which are the same backbone with different ion exchange groups, revealed PAE-Q exhibited slightly better stability.

Table 6.1 Percentage of remaining benzyltrimethyl ammonium groups relative to the initial state, which are determined by the integral with respect to internal standard, DMSO.

Time (min)	QmPES- X <sub>6.7</sub> Y <sub>7.7</sub>	QmFPES- X <sub>6.4</sub> Y <sub>4.7</sub>	PAE-Q	PAE-N
<b>1</b>	100.0	100.0	100.0	100.0
<b>2</b>	83.0	93.6	68.9	81.7
<b>3</b>	77.2	89.0	67.0	65.0
<b>4</b>	71.0	83.4	62.4	60.2
<b>5</b>	67.4	80.6	62.6	55.3
<b>6</b>	64.2	77.6	59.7	51.9
<b>7</b>	62.1	68.4	59.1	49.2
<b>12</b>	58.9	62.3	51.1	47.4
<b>17</b>	44.1	56.4	53.3	44.7
<b>22</b>	37.0	52.0	50.5	42.5
<b>27</b>	34.5	47.6	50.1	41.5
<b>32</b>	31.5	45.9	51.5	40.1
<b>37</b>	25.5	42.5	50.0	39.5
<b>42</b>	23.9	40.2	49.5	39.1
<b>47</b>	21.4	37.0	49.7	36.6
<b>77</b>	12.9	28.6	48.6	38.4
<b>107</b>	9.0	23.2	46.7	36.3
<b>137</b>	7.6	20.7	46.8	33.6
<b>167</b>	5.8	17.6	44.1	32.7
<b>197</b>	4.5	16.8	42.0	32.5
<b>227</b>	3.1	14.7	41.9	31.9
<b>257</b>	2.4	13.2	42.0	32.1
<b>287</b>	1.8	12.9	38.7	31.3
<b>317</b>	0.6	10.6	36.1	30.8
<b>347</b>	0.0	10.5	36.2	31.7
<b>377</b>	0.0	9.2	38.0	31.5
<b>407</b>	0.0	8.6	36.4	30.6
<b>437</b>	0.0	7.9	37.5	31.4
<b>467</b>	0.0	7.9	35.8	32.3

It should be also noticed that the degradation rate was not consistent over the time. For all samples, the degradation at the initial stage is significantly faster than that at the final stage. This observation indicates that degradation process of selected AEMs cannot be expressed by the simple first-order kinetics. The chemical environment change caused by the degradation of electron-withdrawing quaternary ammonium groups could alter the susceptibility of benzylic methylene to the methoxide nucleophile. The similar results were also found by Nuñez and Hickner.<sup>75</sup> They attributed the change of degradation kinetics to functionalization distribution or a change in solubility. In other words, when most of the benzyl trimethylammonium groups are intact, electron-withdrawing quaternary ammoniums might increase electrophilic character and the local hydration around benzylic position, which allow for an increased susceptibility to attack by KOH.

To investigate the stability of the polymer backbone, I compared DOSY spectra of each sample. Figure 6.6 along with Figure 6.4 demonstrate the diffusion coefficient of the polymer membranes changed after degradation for 557 min. The diffusion coefficient depression of QmFPES- $X_{6.4}Y_{4.7}$  and QmFPES- $X_{6.4}Y_{4.7}$  is greater than that of PAE-Q and PAE-N, which suggest that poly (arylene ether sulfone)s (i.e., QmFPES- $X_{6.4}Y_{4.7}$  and QmFPES- $X_{6.4}Y_{4.7}$ ) underwent a significant molecular weight decrease due to the disconnection of polymer chains. This result is agreed with the previous report that decomposition of polysulfone backbones can take place by treating with concentrated aqueous base solution at high temperature.<sup>83</sup> As discussed above, the inductive effect of the electron-withdrawing sulfone group may contribute this phenomenon.

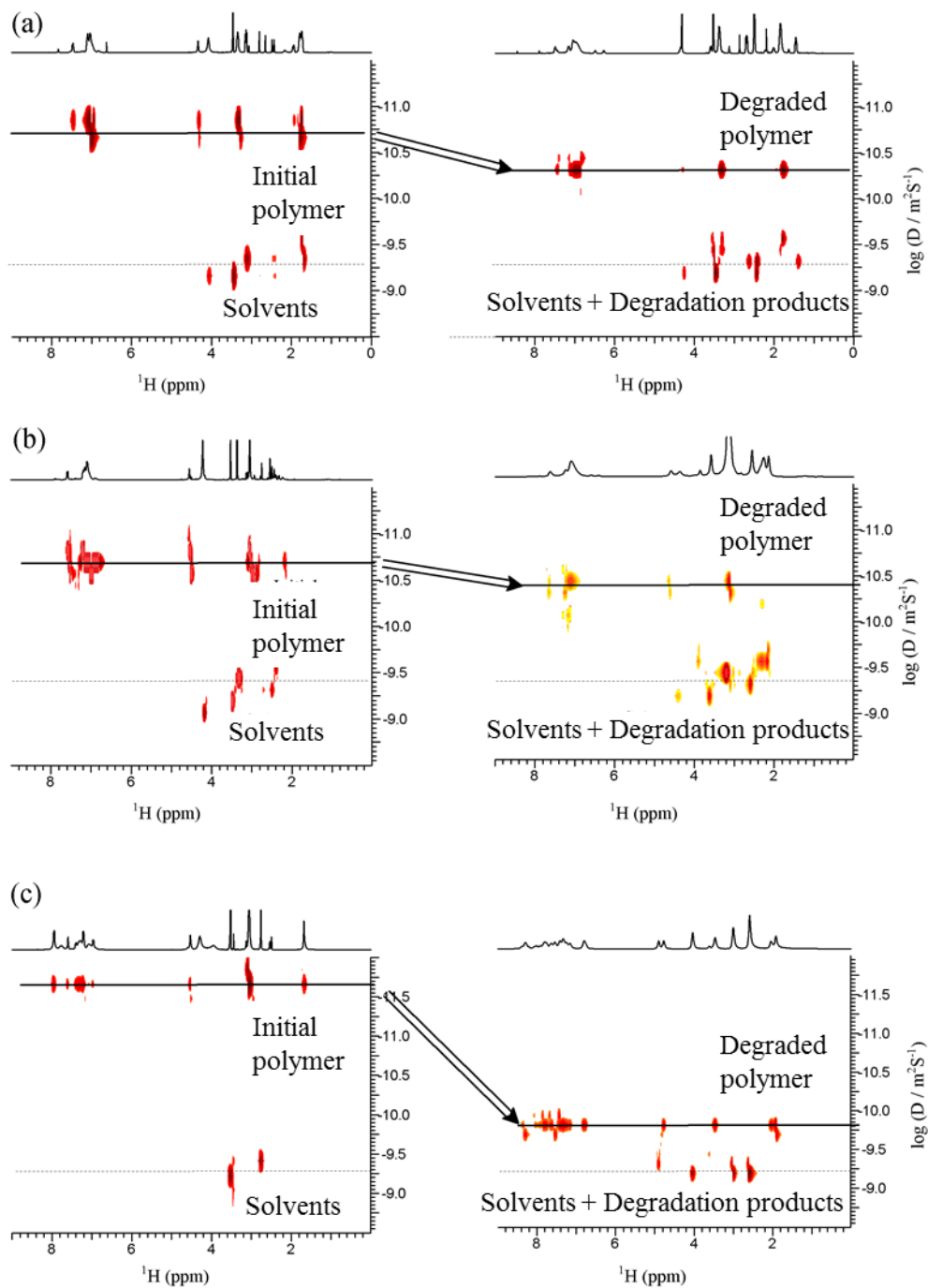


Figure 6.6 DOSY spectra of initial and degraded (a) PAE-Q, (b) PAE-N, and

(c) QmFPES- $X_{6.4}Y_{4.7}$ .

# CHAPTER 7

## USAGE OF SYNTHESIZED ANION CONDUCTIVE POLYMERS FOR HYBRID DIRECT METHANOL FUEL CELLS

### 7.1. Introduction and Objectives

The evaluating tool of the anion conductive polymer synthesized here is a hybrid cell using methanol fuel in which the polymers are utilized as an anion conductive ionomer. Methanol is the liquid fuel of high energy density whose theoretical energy density is about 5.0 kW/kg. This benefit is significant comparable to that of pressurized hydrogen (1.1 kW/kg) and that of lithium ion batteries (180 W/kg).<sup>84, 85</sup> Another and more remarkable feature of a fuel cell system using methanol fuel is that it is suitable for portable electronics because of no need of reformers that is required for hydrogen fuel cell systems, facile fuel replenishment using methanol cartridges, its compact size, and the possibility to operate at room temperature.<sup>86</sup>

However, methanol based PEMFC has been hampered from broad commercialization because of several issues. First of all, the rate of methanol oxidation at an anode is significantly slower than that of hydrogen oxidation. As indicated electrochemical reactions in Table 7.1, methanol oxidation is involved with six electrons compared to two electrons for hydrogen oxidation, which leads to sluggish oxidation. The considerable amount of noble metal catalysts is required to obtain the reasonable reaction rate, which is inevitably accompanied with cost issues of the device.

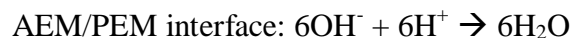
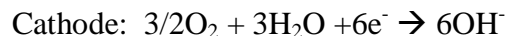
Table 7.1 Electrochemical reaction of methanol and hydrogen based fuel cells.

Anode: $\text{CH}_3\text{OH} + \text{H}_2\text{O} \rightarrow 6\text{H}^+ + 6\text{e}^- + \text{CO}_2$	Anode: $\text{H}_2 \rightarrow 2\text{H}^+ + 2\text{e}^-$
Cathode: $3/2\text{O}_2 + 6\text{e}^- + 6\text{H}^+ \rightarrow 3\text{H}_2\text{O}$	Cathode: $1/2\text{O}_2 + 2\text{e}^- + 2\text{H}^+ \rightarrow \text{H}_2\text{O}$
Overall: $\text{CH}_3\text{OH} + 3/2\text{O}_2 \rightarrow 2\text{H}_2\text{O} + \text{CO}_2$	Overall: $\text{H}_2 + 1/2\text{O}_2 \rightarrow \text{H}_2\text{O}$

Direct methanol PEMFCs also suffer from the fuel crossover problem, methanol transports across the membrane mainly due to the concentration gradient and the electro-osmotic drag along with proton transportation. The fuel crossover can cause several problems including the depression of open circuit voltage, deterioration of coulombic efficiency, and the decrease of catalyst utilization.<sup>87</sup> Electro-osmotic drag and water management of the direct methanol fuel cell can cause another problem, cathode flooding. More water added by electro-osmotic drag at cathode where water is produced by oxygen reduction generally results in the blockage of oxygen transport and the decrease of catalyst utilization.

Alkaline based direct methanol fuel cells are thought to be an alternative to address the restrictions of proton based direct methanol fuel cells because of the following reasons: 1) Alkaline conditions enhance methanol oxidation kinetics,<sup>88</sup> 2) the possible usage of non-noble metal catalysts leads to reduced cost, and 3) the opposite direction of anion transport to that of proton transport suppresses methanol crossover and cathode flooding.<sup>89</sup> However, effective anion conductive membranes and ionomers have not been established for alkaline based methanol fuel cells. Further developments of anion conductive polymeric materials and non-noble metal catalysts are required to improve the cell performance.

A new cell configuration has been attempted to utilize the advantages of the PEM and the AEM together, a hybrid polymer electrolyte fuel cell.<sup>90</sup> This cell enables exploiting favored electro-kinetics of oxygen reduction using non-noble metal catalysts with utilizing the highly conductive and stable PEM. Among the two possible configurations, AEM anode / PEM cathode and AEM cathode / PEM anode, the second configuration is chosen for the evaluating tool of synthesized anion conductive polymers as an ionomer. This configuration can take advantage of favorable oxygen reduction at high pH. Water management is also relatively facile since water is created in the interface close to the cathode in which water is consumed.<sup>79</sup> The reactions in this hybrid cell are listed as follows:



Main objectives of this study are to evaluate the performance of selected anion conductive polymers synthesized here as an ionomer for the AEM cathode electrode, and to correlate the properties of the polymers with cell performance.

## 7.2. Experimental Details

### 7.2.1. Materials

The catalyst for anode, Pt 50wt% / Ru 25wt% / C 25wt% was purchased from Alfa Aesar. The catalyst for cathode Pt 40wt% /C was obtained from FuelCellStore. The anode catalyst loading was 4 mg/cm<sup>2</sup> and the cathode catalyst loading was 2 mg/cm<sup>2</sup>. Nafion 117 membranes and Nafion in isopropanol (IPA) (5 wt%) were obtained from Ion Power Inc. High purity solvents including dimethyl formamide (DMF), IPA, methanol, and sodium hydroxide were purchased from VWR. Oxygen and air were obtained from Airgas Inc. Deionized water was used for all experiments. A hydrophilic gas diffusion layer (GDL) 2050L for the anode and a hydrophobic TGPH-090 for the cathode were obtained from FuelCellStore.

The Nafion 117 membrane was pretreated by boiling in 3% H<sub>2</sub>O<sub>2</sub>, followed by treating with 1M H<sub>2</sub>SO<sub>4</sub> and then H<sub>2</sub>O at 80°C. Each step was followed by rinsing with distilled water several times. The membranes were stored in distilled water until used in the membrane electrode assembly (MEA) fabrication.

### 7.2.2. Electrode fabrication<sup>87,91</sup>

#### Thin-film method

The electrode fabrication consisted of the following sequence. For the AEM cathode, the alkaline ionomer (2 wt% in DMF) was mixed with the Pt/C catalyst (40 wt %) so that the ionomer content was 10 wt% with respect to the catalyst. A DMF and ethanol mixture (3:2 by weight) was added in order to prepare the catalyst slurry. The

prepared mixture was then sonicated for 30 minutes at room temperature. The mixture was sprayed on the GDL 2050L until the desired loading was achieved. A half of the amount of initial ionomer was sprayed on the catalyst layer surface to prevent the direct contact of the catalyst with the membrane. The electrodes were then dried at room temperature and immersed in 0.1 M NaOH solution overnight in order to exchange  $\text{Cl}^-$  to  $\text{OH}^-$  ions. Fresh aq. 0.1 M NaOH was replenished for the completion ion exchange. Finally, the electrodes were soaked in distilled water to remove the excess  $\text{OH}^-$  ions.

For the PEM anode, PtRu/C (75 wt%) was mixed with a 5 wt% Nafion solution in IPA so that the Nafion consisted of 15 wt% with respect to the catalyst for the preparation of the low pH electrodes. Water and isopropyl alcohol (IPA) (1:3 by weight) were used to prepare the catalyst slurry. The slurry was sprayed on the GDL TGPH 90 and dried at room temperature.

#### Ionomer impregnation method

The AEM cathodes were prepared by first spraying the catalyst ink without the ionomer followed by spraying the ionomer solution. The catalyst ink was prepared by mixing Pt/C (40 wt %) with DMF and ethanol (3:2 by weight) and 5 wt% PTFE in aqueous dispersion whose amount become 10 wt% of the catalyst. The ink was ultrasonically agitated for 30 minutes and sprayed directly on the GDL TGPH 90. The GDL with the catalyst layer was then annealed at 250 °C under  $\text{N}_2$  flowing. The alkaline ionomer solution (2 wt % in DMF) was then sprayed on the catalyst surface so that it accounted for 10 wt% compared to the catalyst. The electrodes were then dried at room

temperature and exchanged in the same procedure as described before. The PEM anodes were prepared by the same procedure as described for the thin-film method.

### **7.2.3. MEA assembly**

A 5 wt% Nafion/ IPA mixture was sprayed directly on the electrode surface immediately before assembly. The PEM anode and the AEM cathode were pressed onto the Nafion 117 membrane at 60°C and 2 MPa gauge pressure for 10 minutes.

The fuel cell hardware was obtained from Fuel Cell Technologies. The Poco graphite blocks were machined with a single serpentine pattern for the fuel and gas flow. Stainless steel plates were used as the current collectors. Preheated methanol (55°C) was circulated at different speeds (0.15 to 5 ml/min) with a peristaltic pump. Oxygen gas flew counter current to the methanol flow at the cathode at 50 sccm in all tests at ambient pressure. The equilibration of the MEA was carried out by operating the cell at a constant load of 250 mV for 10 hours before the electrochemical data were recorded. The polarization curves for the MEAs were obtained by using a Princeton PAR 2273 potentiostat.

## **7.3. Results and Discussion**

### **7.3.1 Different ion exchange groups**

The anion conductive polymers as an ionomer for this comparison, as shown in Figure 7.1, were obtained from The Kohl group (PAE-Q and PAE-N). The detail synthetic scheme is illustrated in Figure 6.1. The polymer is poly (arylene ether)s composed of a highly hydrophobic backbone with hydrophilic ion exchange groups

tethered off from the backbone. Different ion exchange groups, trimethyl ammonium and quinuclidinium, were introduced in the final step of the synthetic scheme.

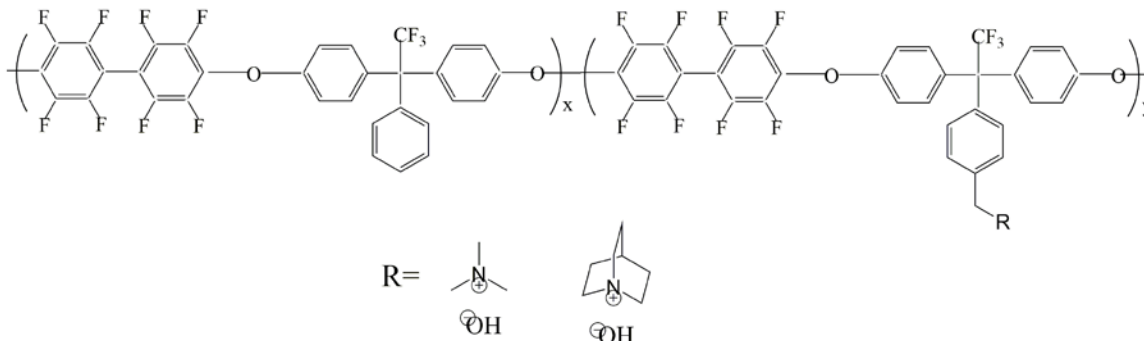


Figure 7.1 Selected anion conductive ionomer with different ion exchange group, trimethylamine and quinuclidinium (PAE-Q and PAE-N).<sup>79</sup>

Figure 7.2 compares the performance of the hybrid cells using quinuclidinium and trimethyl ammonium based ionomers for the AEM cathode at different methanol flow rate. At the 0.6 ml/min flow rate of methanol, the quinuclidinium ionomer outperformed compared to the trimethyl ammonium ion exchange groups. Previous reports that van der Waals volume of quinuclidine cation is greater than that of n-hexyl trimethyl ammonium cation for ionic liquids based on two cations (i.e., 0.137 nm<sup>3</sup> for quinuclidine versus 0.110 nm<sup>3</sup> for trimethyl ammonium).<sup>92</sup> The better performance of the quinuclidinium based ionomer could be attributed to the greater free-volume within the electrode structure resulting in efficient mass transport.

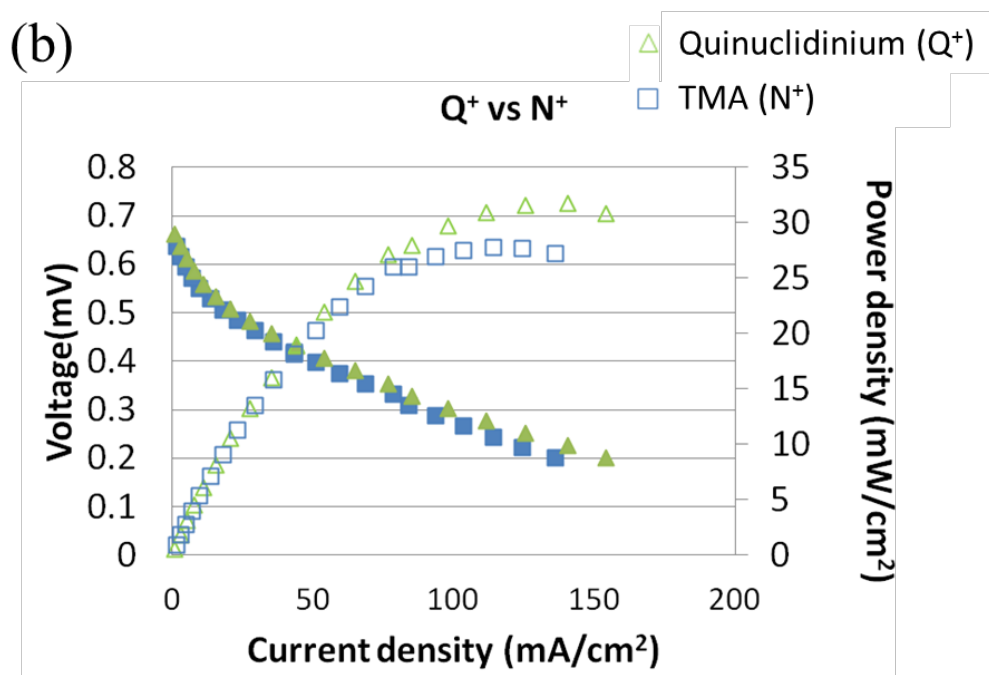
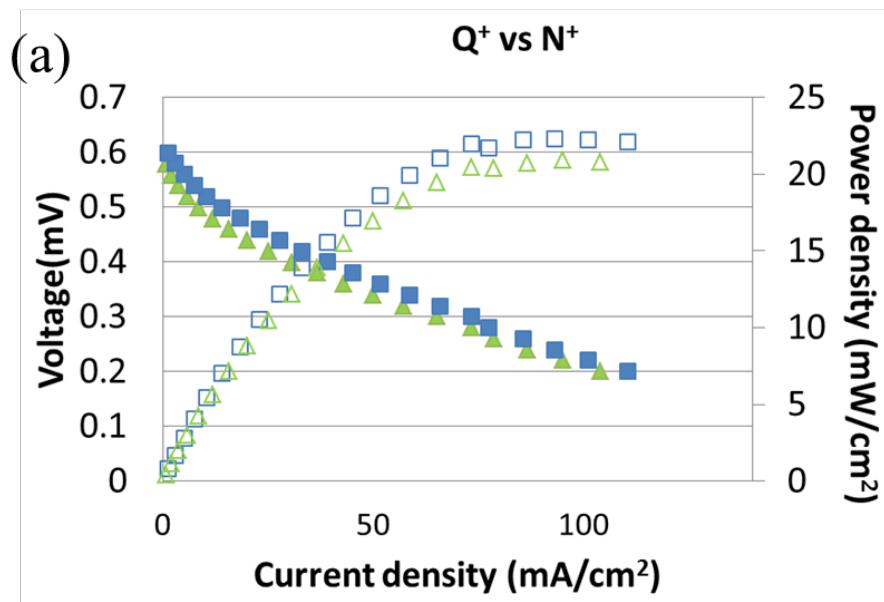


Figure 7.2. Voltage and power density curves for the hybrid fuel cells with trimethyl ammonium and quinuclidinium ionomers at the AEM cathode using 2M MeOH and 50 sccm O<sub>2</sub> at 55°C, (a) methanol flow rate is 5 ml/min and (b) methanol flow rate is 0.6 ml/min.

### **7.3.2. Different circulation rate of methanol**

I also learned that the methanol flow rate considerably influences on the cell performance. The low flow rate of methanol circulation exhibited improved performance most likely due to less methanol cross-over. At the low circulation rate, the consumed methanol may not be replenished quickly, so that the concentration gradient of methanol becomes larger and thus methanol cross-over could be reduced. Figure 7.3 shows the results of the cell operation at much lower circulation rate of methanol. The lower circulation rate than 0.6 ml/min of methanol did not provide any benefits in terms of maximum power density and steadiness of the cell performance.

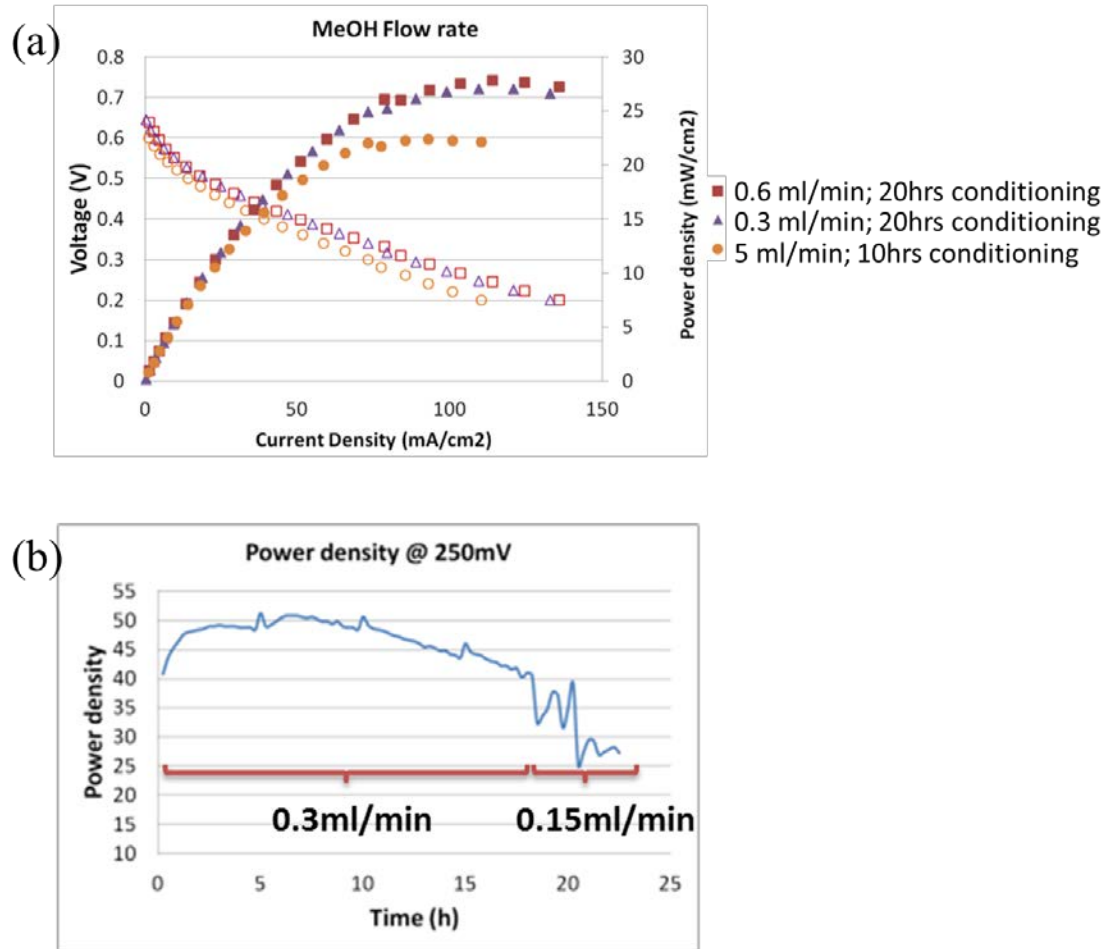


Figure 7.3 (a) Voltage and power density curves for the hybrid fuel cells with quinuclidinium ionomers at the AEM cathode using 50 sccm O<sub>2</sub> and 2M methanol at 55°C at different methanol flow rates. (b) Steady state performance of the cell at constant voltage of 250mV at different flow rate

### 7.3.3. Different oxidants (oxygen and air)

Figure 7.4 demonstrates that the cell polarization power density curve obtained from the hybride cell with the quinuclidinium ionomer using different oxidants, oxygen and air of 50 SCCM. As expected, the cell using oxygen offered the higher open circuit voltage and the better performance than the case of air. The low oxygen partial pressures

of air reaching the cathode catalyst reduced the reaction kinetics at cathode. The current density difference for each case increased as the cell potential decreased.<sup>93</sup>

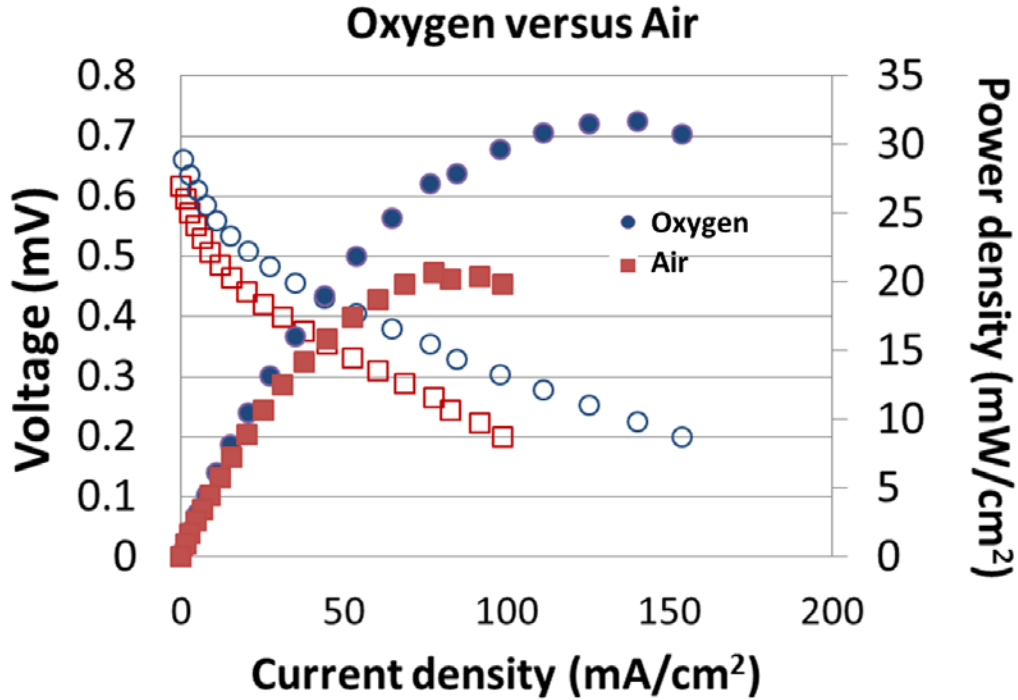


Figure 7.4. Voltage and power density curves for the hybrid fuel cells with quinuclidinium ionomers at the AEM cathode using 2M MeOH and 50 sccm of different oxidants, O<sub>2</sub> and air at 55°C

#### 7.3.4. Different fabrication methods (thin-film and ionomer impregnation)

M. Ünlü et al. evaluated two different fabrication methods, thin-film and ion-impregnation, creating different structures of a catalyst layer.<sup>91</sup> As illustrated in Figure 7.5, the ionomer impregnation method generated non-uniform ionomer distribution in the catalyst layer as compared to the relatively uniform electrode structure out of the thin-film method. They found that the ionomer impregnation method leads to enhanced cell performance, which is attributed to increased free volume and thus gas diffusion caused

by non-uniform distribution of the ionomer. I applied the two fabrication methods to the direct methanol hybrid cell using the ionomer, PAE-Q.

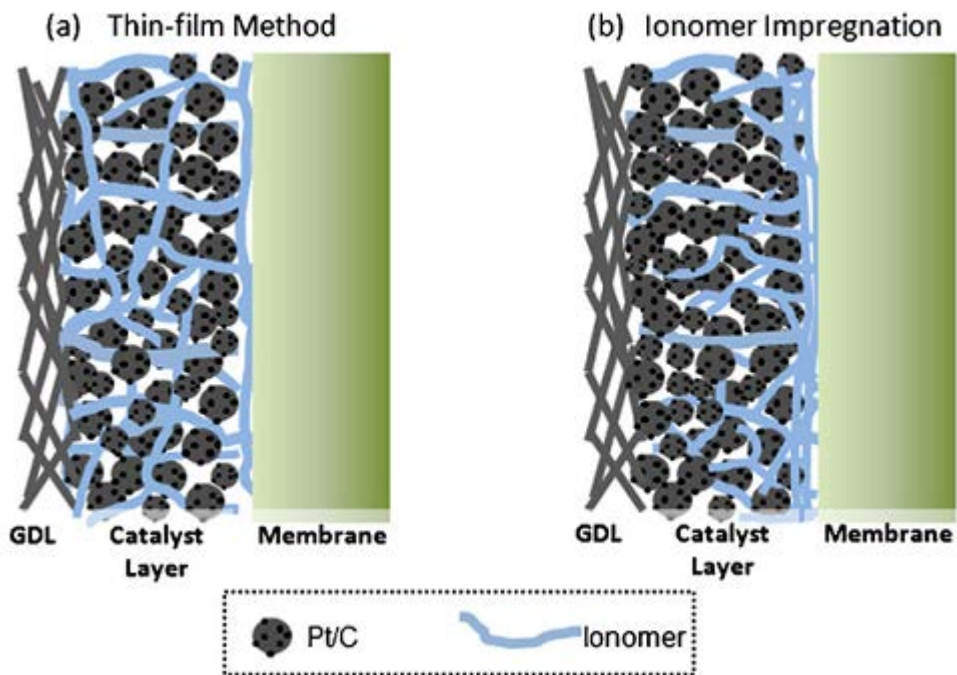


Figure 7.5 Schematic diagram of the electrode structure created by (a) thin-film and (b) ionomer impregnation methods<sup>91</sup>

As shown in Figure 7.6, the two methods did not make a significant difference in terms of maximum power density. However, the performance of the cell prepared using the thin-film method is more stable than that of the cell prepared using the ionomer impregnation method. This result suggests that the transportation of liquid fuel (i.e., 2M methanol in water) is not influenced by the morphology change of the electrode induced by the different fabrication methods. Further investigation will be necessary to investigate the relationship between a fabrication method and performance of a cell using liquid fuel.

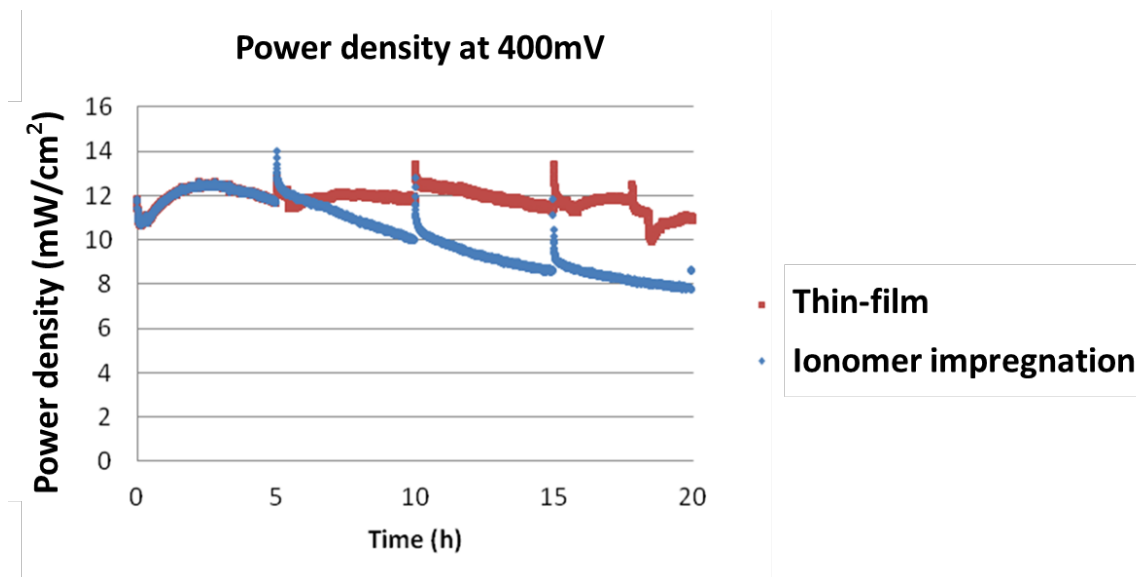


Figure 7.6. Steady state performance of the cell created by the thin-film method and the ionomer impregnation at constant voltage of 400mV.

### 7.3.5. Multiblock copolymer ionomers

I utilized several multiblock copolymers as an ionomer for the AEM cathode of the direct methanol hybrid fuel cell. An ionomer is a critical element to determine overall fuel cell performance since it plays very important roles in the electrode including a binder of catalyst particle, an ion conducting agent, and a fuel and oxidant transporting material. As illustrated in Figure 1.9, three main resistances are involved in an ionomer that exists in the AEM cathode: (1) the inhibition of the oxygen diffusion by the blockage of secondary pores (i.e., pores between agglomerated catalyst-supported carbon particles), (2) the resistance to oxygen permeation from the secondary pores to a reaction site through the ionomer layers, and (3) the limitation of anion conductivity. I believed that multiblock copolymer ionomers with different properties such as water uptake, an IEC, ion conductivity, hydrophobicity, and a segment size were suitable to investigate the relationship between properties of ionomers and cell performance.

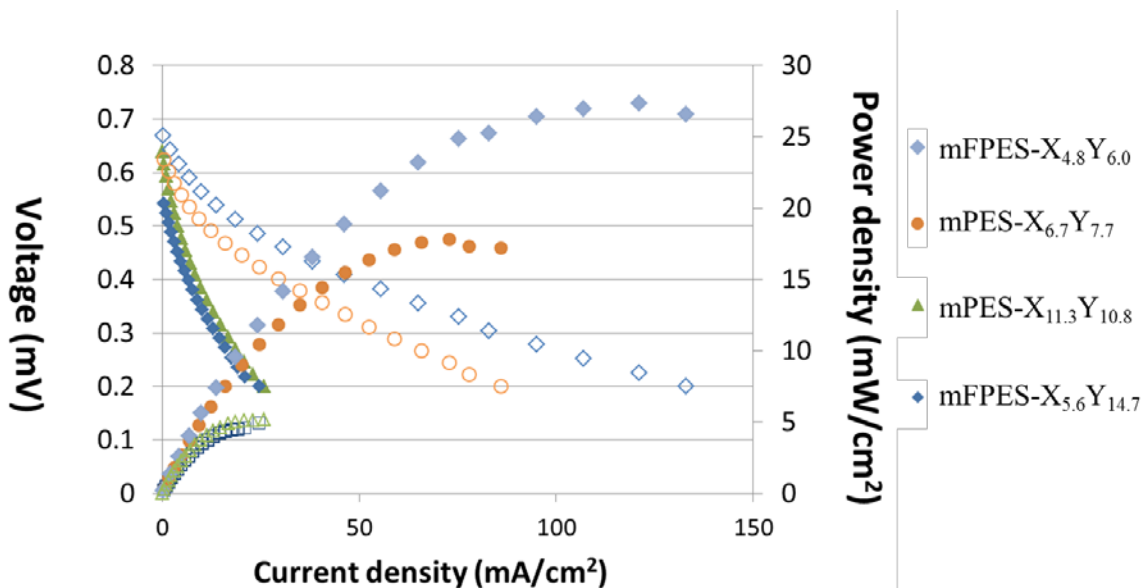


Figure 7.7. Voltage and power density curves for the hybrid fuel cells with selected multiblock copolymer ionomers at the AEM cathode using 2M MeOH and 50 sccm of O<sub>2</sub> at 55°C

Table 7.2. Properties of selected multiblock copolymers as an ionomer of the AEM cathode

	Y/X	IEC (meq/g)	Water uptake (%)	Conductivity @ 60°C
mFPES-X <sub>4.8</sub> Y <sub>6.0</sub>	1.2	2.0	49.0	43.5
mFPES-X <sub>5.6</sub> Y <sub>14.7</sub>	2.6	3.0	147	48.7
mPES-X <sub>6.7</sub> Y <sub>7.7</sub>	1.1	2.3	47.5	27.9
mPES-X <sub>11.3</sub> Y <sub>10.8</sub>	0.95	1.9	59.5	23.1

As shown in Table 7.2 and Figure 7.7, properties of the multiblock copolymers significantly impact cell performance. The highest performance was obtained using mFPES-X<sub>4.8</sub>Y<sub>6.0</sub>. Its high conductivity and moderate water uptake are believed to lead to improved cell performance. The mPES-X<sub>6.7</sub>Y<sub>7.7</sub> ionomer with lower conductivity than mFPES-X<sub>4.8</sub>Y<sub>6.0</sub> despite similar IEC and water uptake might cause the lower cell performance. The comparison between mFPES-X<sub>4.8</sub>Y<sub>6.0</sub> and mFPES-X<sub>5.6</sub>Y<sub>14.7</sub> revealed

the effect of water uptake. In spite of similar conductivities of two ionomers, the cell performance using two ionomers was remarkably different. Excessive water uptake of mFPES- $X_{5.6}Y_{14.7}$  may cause the resistance of oxygen transport through a catalyst layer by swelling of the ionomer. The length of hydrophilic segments seemed to be a key factor for optimum cell performance. The usage of the mPES- $X_{11.3}Y_{10.8}$  ionomer for the hybrid cell did not perform positively. Its slightly higher water uptake and lower conductivity than those of mFPES- $X_{4.8}Y_{6.0}$  might lead to poor performance of the cell. In addition, incorporation of catalyst with the multiblock ionomer having long segment lengths might not be efficient. Further investigation of catalyst incorporation relating to size and polarity of the ionomers will need to prove this hypothesis.

## CHAPTER 8

### CONCLUSION AND FUTURE WORKS

#### 8.1. Summary and Concluding Remarks

A systematic study of the effect of block lengths, the degree of randomness, and hydrophobicity on the ionic conductivity in a series of multiblock and random copolymers containing quaternary ammonium groups was undertaken. The polymers were synthesized by a polycondensation reaction of separately synthesized oligomers. The multiblock copolymers with additional fluorine groups were prepared to investigate the effect of the increased polarity difference between hydrophilic and hydrophobic segments. The reaction conditions were optimized and the length of the blocks, overall molecular weight of the polymers, and the degree of chloromethylation were controlled. NMR techniques, including the DEPT-135 and the two-dimensional HMBC and COSY, were used to determine the degree of randomness and the position of chloromethyl groups in the polymers.

Quaternary ammonium attached anionic conductive membranes were prepared with reasonably high conductivity despite the low water uptake (37.7 mS/cm at 60 °C in mPES- $X_{6.7}Y_{3.4}$ ). The NMR relaxation times ( $T_1$  and  $T_2$ ) of water in the membranes were used to explain 1) the high conductivity obtained with mPES- $X_{6.7}Y_{3.4}$  compared to multiblock copolymers with higher IEC values, 2) the higher conductivity of multiblock copolymer membranes compared to their random copolymer counterparts, and 3) the

observed nonlinear dependency of the ionic conductivity on the IEC and water content. These results imply that the higher performance which was found in optimized IEC with facile ion/water transport correlates with the channel morphology and short NMR relaxation times for water.

The additional fluorinated multiblock copolymer membranes with enhanced conductivity were prepared (50.5 mS/cm at 60 °C in mFPES-X<sub>5.6</sub>Y<sub>9.7</sub>). Low temperature DSC measurements to determine the amount of freezable and non-freezable water were employed to explain different conductivities of the fluorinated membranes with similar water uptake and IEC. The ratio between the number of freezable water and non-freezable water had a linear relationship with conductivity at a lower IEC than 2.2 meq/g. DSC results along with the activation energy of diffusion also offered insights into the anion conducting processes in the membranes. The observations that the majority of water turned out to be non-freezable water and reasonably high conductivity of the membrane with virtually no freezable water (e.g.,  $\sigma = 31.4$  mS/cm for mFPES-X<sub>6.4</sub>Y<sub>4.7</sub> and  $\sigma = 36.8$  mS/cm for mFPES-X<sub>3.5</sub>Y<sub>4.7</sub>) imply that the dominant ion transportation that takes place in the extreme proximity of the ion-exchange groups of the membrane.

Quantitative chemical stability of the synthesized AEMs relating to the characteristics of polymer backbones and ion-exchange groups was tested using *in-situ* <sup>1</sup>H NMR measurements and DOSY. The electron-withdrawing groups like sulfones accelerated degradation processes. The comparison between QmPES-X<sub>6.7</sub>Y<sub>7.7</sub> and QmFPES-X<sub>6.4</sub>Y<sub>4.7</sub> suggested that the higher hydrophobicity of the polymer improved the durability. The DOSY offered the information about molecular weight decrease by

detecting the increase of diffusion coefficients caused by the polymer backbone decomposition.

Finally, the synthesized polymers, PAEs and multiblock PESs, were applied as an ionomer for the AEM cathode of direct methanol hybrid fuel cells. The operation conditions of the cell such as the speed of methanol circulation and the fabrication methods for the AEM cathode were optimized. The quinuclidinium cationic head group of the PAE led to superior performance of the cell to the trimethyl ammonium cationic head group. The different properties of multiblock copolymers impact significantly on the cell performance. Improved cell performance was obtained using high conductivity with moderate water uptake. Excessive water uptake had a detrimental effect of resisting gas transportation through the catalyst layer.

## **8.2. Suggested Future Works**

### **8.2.1 Further development of nanostructure for more efficient ion conduction**

In this thesis, I presented anion conductive multiblock copolymer in which nanostructures with tunable morphologies and domain sizes by controlling the lengths and the polarity of each segment. Further developments of a less-tortuous and well-organized nanostructure could be accomplished by modifying film-formation methods. Park and Balsara demonstrated that anisotropic conductivities (i.e., in-plane and through-plane conductivities) were obtained by applying various external stimuli such as shear flow, pressure, and electric field.<sup>94</sup> This study can be supported by the measurements of

anisotropic diffusion coefficient of water molecule inside a membrane,<sup>95</sup> two-dimensional small angle scattering (SAXS), and TEM,<sup>96</sup> and may suggest an efficient membrane-formation method to tune conductivity in targeted directions.

As discussed in Chapter 4, the additional fluorinated multiblock copolymers had enhanced conductivities and this improvement was attributed to more distinct phase-separated and well-organized morphology of the membrane. I also observed that increased hydrophobicity enable to retain more water without destroying ion channels. In the light of this observation, I suggest that adding more fluorine group selectively on the hydrophobic segments could be helpful to increase conductivity without sacrificing physical properties at excessive water uptake.

### **8.2.2. Ion exchange groups other than quaternary ammonium groups**

As discussed in Chapter 6, quaternary ammonium groups are still standard ion exchange groups for anion conductive membranes. Recently, a few reports that other ion exchange groups such as phosphonium,<sup>35, 97, 98</sup> guanidinium,<sup>99</sup> imidazolium,<sup>100</sup> and pyridinium<sup>101</sup> offered benefits in terms of chemical stability of the membrane and cell performance using the polymers were appeared. In this research, I also found that quinuclidinium cationic groups outperformed as an ionomer for direct methanol hybrid cell compared to trimethyl ammonium groups. Electron-withdrawing groups and steric hindrance turned out to be the key factors to determine the chemical stability of an AEM. Overall, fundamental investigations on various ion exchange groups considering inductive and/or steric effects will be necessary for designing robust AEMs.

### 8.2.3. Nanocomposite polymer membranes for alkaline fuel cells

Use of nanotechnology in the development of AEMs is potentially beneficial because it could increase mechanical properties of membranes and ion mobility caused by augmented free volume. Besides, functionalized nanoparticles could be an additional source of ion exchange groups. Wu et al. investigated an optimum heat treatment that increased alkaline resistance and the thermal stability of silica/poly(2,6-dimethyl-1,4-phenylene oxide) AEMs.<sup>102</sup> Lue et al. found that silica/poly (vinyl alcohol) (PVA) nanocomposite membranes exhibited reduced methanol crossover behavior when they compared plain PVA membranes in direct methanol alkaline fuel cells (DMAFCs).<sup>103</sup> They also attributed the facilitated water transport to the increased free volume of nanocomposite membranes. Wang et al. reported the possibility that inorganic nanoparticles acted as additional ion channels.<sup>104</sup> The addition of 3-(trimethylammonium) propyl-functionalized silica to PVA showed higher water uptake without affecting on stability.

I proposed the synthesis of novel AEMs that are nanocomposited between fluorinated aromatic polymers containing the quaternary ammonium group and functionalized inorganic oxide (e.g., silica or TiO<sub>2</sub>). The functionalization of inorganic oxide with quaternary ammonium groups will be additional sources of the ion channel. Moreover, perfluorinated phenyl or alkyl ligands onto nanoparticles should increase the miscibility with fluorinated polymers.<sup>105</sup> Once polymers composited with synthesized inorganic nanoparticles, further investigation of the optimum film casting conditions with the aforementioned PNCs will need to follow.<sup>106</sup>

# APPENDIX

## DIFFUSION ORDERED SPECTROSCOPY FOR CYLINDRICAL POLYMER BRUSHES

### A.1. Introduction and Objectives

Cylindrical polybrush materials have been drawing attention because of their special morphological features. They exhibited exceptional polymer chain stiffness and extension with persistence lengths over 100 nm,<sup>107</sup> compared to a random coil morphology. Their morphological and structural characteristics enable them to be applied for dendronized polymers<sup>108</sup> and highly ordered film assembly under flow.<sup>109</sup> A polyrotaxane, a topological linear polymer onto which several macrocyclic molecules (e.g., cyclodextrins) are threaded, can be the candidate of scaffolds for the polybrush. Recently, Teuchert et al. reported the synthesis of cylindrical polymer brushes, by atom transfer radical polymerization of methyl methacrylate (MMA) from an  $\alpha$ -cyclodextrin ( $\alpha$ -CD) polyrotaxane template.<sup>110</sup> They observed that the synthesized polybrushes exhibited two distinct peaks in the GPC curve, one of which was corresponded to the polybrush and the other was corresponded to the dethreaded  $\alpha$ -CD-PMMA. They attributed this phenomenon to mechanical forces (i.e., shear force induced by passing through GPC column). DOSY experiments were suggested to support this concept because it can provide molecular size information of a specific molecule without any mechanical stress during measurements. This technique was already used for providing

the direct evidence of threading for the polyrotaxane.<sup>111</sup> This section of the thesis aims at characterizing the rupture of the cyclic polybrush using DOSY in the comparison with GPC results.

## A.2. Experimental Details

Diffusion ordered NMR spectroscopy (DOSY) was conducted at 22 °C using 5-mm NMR tubes on a Bruker AMX 400 operating at 400 MHz. Sample concentrations were 0.4% (w/v) in CDCl<sub>3</sub>. All DOSY spectra were collected using a bipolar pulse pair and longitudinal eddy current delay (BPP-LED) sequence. For the BPP-LED sequence, gradients were applied for 5 ms ( $\delta$ ), and the diffusion time ( $\Delta$ ) was 500 ms. The delay times for gradient recovery and eddy current elimination were 0.2 and 5 ms, respectively. Homospoil gradients were applied for 0.6 ms to remove residual transverse magnetization. The delay between each scan was 10 s and the number of scans was 16. The gradients were incremented from 0.67 to 32.02 G/cm, which enabled the final intensity of each peak to be less than 3% of its original intensity. Consequently, 32 free induction decays containing 8k data points were collected. The DOSY spectra were constructed based on the assumption that the intensity trends of all chemical shifts over the gradients followed bi-exponential decays.

### A.3. Results and Discussion

The cylindrical polybrush is prepared by the following three steps as illustrated in Figure A.1: 1) the synthesis of  $\alpha$ -CD / PEG polyrotaxane, 2) the attachment of initiators to the threaded  $\alpha$ -CD (the degree of substitution is 7-8, and 3) the ATRP of MMA from initiators on the  $\alpha$ -CDs.<sup>110</sup>

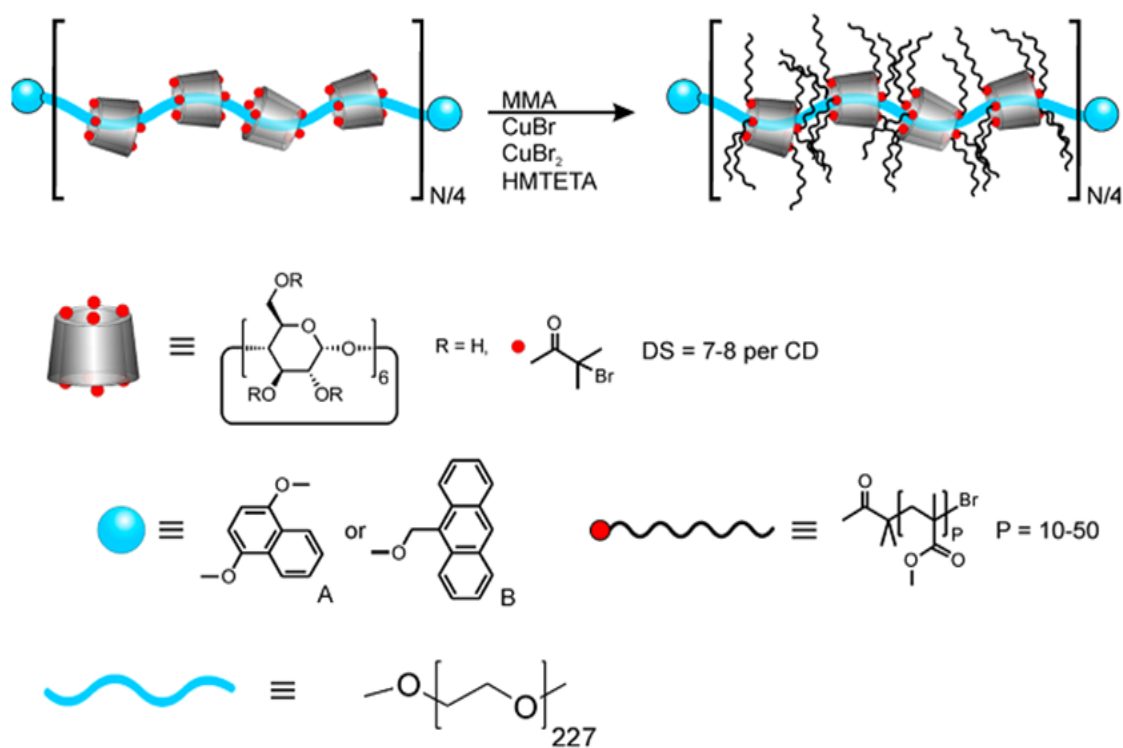


Figure A.1. Synthesis of cylindrical polymer brushes by ATRP from  $\alpha$ -CD-PEG polyrotaxane macroinitiators<sup>110</sup>

DOSY spectra of the polyrotaxane macroinitiator (PRx) and the polybrush are shown in Figure A.2. In each spectrum, two sets of peaks are observed (marked with horizontal dashed lines), indicating that each sample consists of two components with characteristic diffusion coefficients. In Figure A.2 (a), the larger component (smaller  $D$ )

is the PRx and the smaller component (larger  $D$ ) is the initiator attached  $\alpha$ CD. In Figure A.2 (b), the larger component (smaller  $D$ ) is the polybrush and the smaller component (larger  $D$ ) is the PMMA attached  $\alpha$ CD ( $\alpha$ CD star). For both components, the diffusion coefficient decreases from macroinitiator to brush as the grafting reaction leads to larger molecules:  $\log D = -10.35$  to  $-10.6$  for the PRx and  $\log D = -9.4$  to  $-9.75$  for the  $\alpha$ CD star. The DOSY spectrum of the macroinitiator shows  $^1\text{H}$  peaks due to the CD (3.7 – 5.15 ppm) and bromoisobutyrate (1.78 ppm) moieties. The DOSY spectrum of the brush reveals only  $^1\text{H}$  peaks for the PMMA: 0.81, 1.00, 1.78 – 1.93, and 3.63 ppm. The DOSY spectrum of the macroinitiator shows minor amounts of free  $\alpha$ CD initiator even though this is not apparent in the  $^1\text{H}$  NMR spectrum. These observations indicate that the DOSY technique, in which the NMR signal is spread across a second dimension according to molecular size, is more sensitive than standard  $^1\text{H}$  NMR for the structural characterization of these materials.

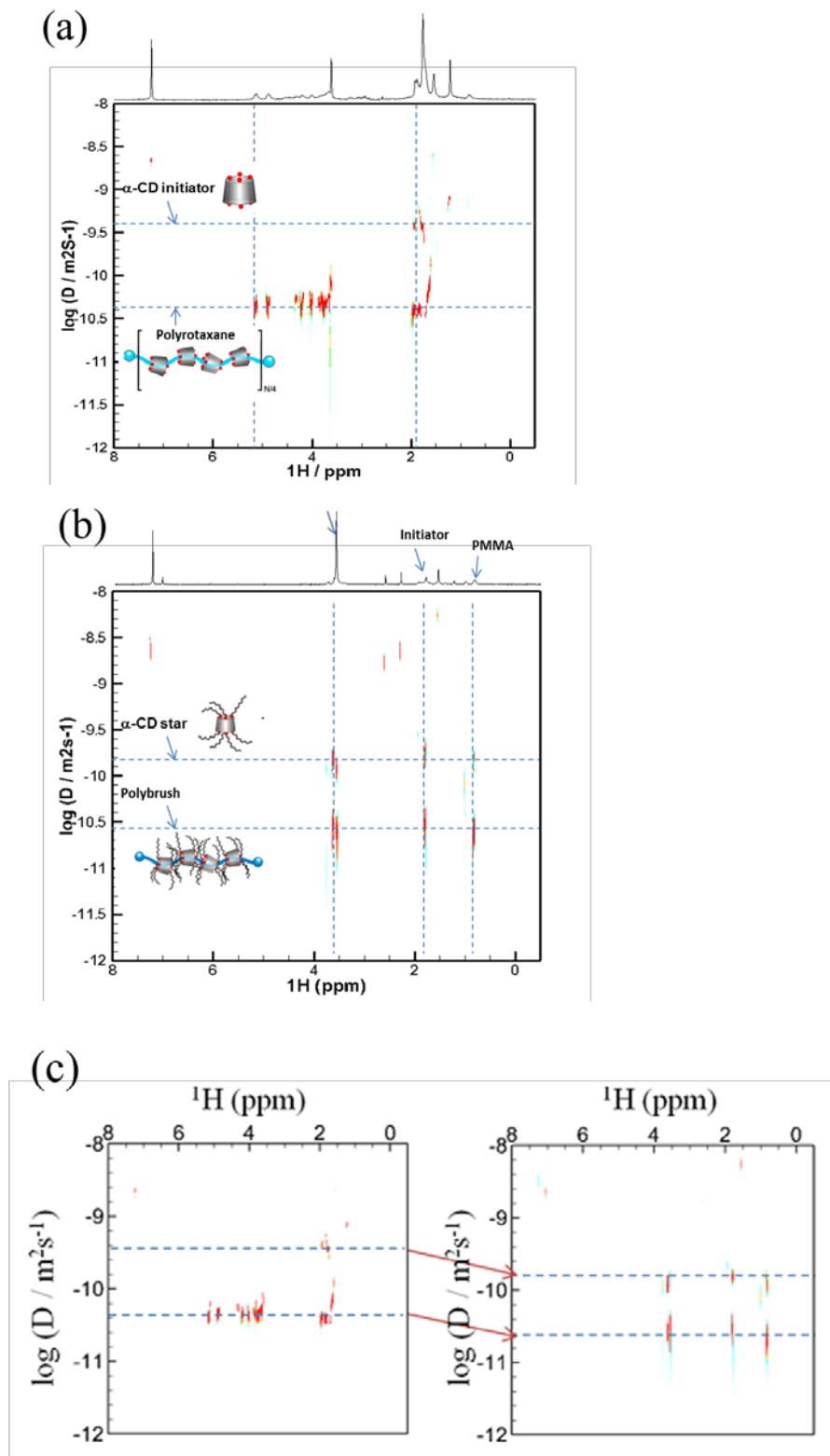


Figure A.2. DOSY spectra of (a) the polyrotaxane and (b) the polybrush. (C) shows the change of diffusion coefficients after MMA polymerization

The relative amounts of star versus brush polymer are obtained from the slice of the DOSY spectrum at 0.8 ppm (corresponding to the  $-\text{CH}_3$  group of the PMMA) along the  $\log D$  axis. Evidently, the NMR signal of the star in the polybrush is much smaller (the fraction of  $\alpha\text{CD}$  star = 20%) than the signal in the corresponding GPC trace, shown for comparison in Figure A.3. Even accounting for the parameters that influence peak intensities in these two techniques (relaxation times versus pulse delays in NMR, and refractive indices in GPC), the signal intensity for the star polymer is still much smaller in NMR than in GPC. Thus, I conclude that shear forces rupture significant amount of the brush thread as the material passes through the GPC column.

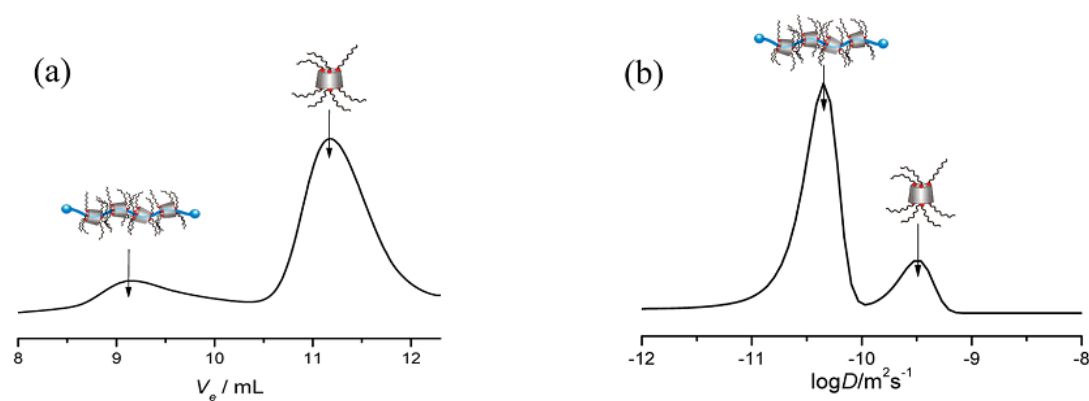


Figure A.3. Comparison of (a) GPC trace and (b) a slice at 0.8 ppm in the DOSY spectrum of the polybrush

## REFERENCES

1. Larminie, J., *Fuel cell systems explained*. J. Wiley: Chichester, West Sussex :, 2003.
2. Shekhawat, D., Spivey, J. J., & Berry, D. A., *Fuel Cells: Technologies for Fuel Processing*. 2011.
3. Department of Energy,  
[http://www1.eere.energy.gov/hydrogenandfuelcells/fuelcells/pdfs/fc\\_comparison\\_chart.pdf](http://www1.eere.energy.gov/hydrogenandfuelcells/fuelcells/pdfs/fc_comparison_chart.pdf).
4. [http://www.fctec.com/fctec\\_types\\_afc.asp](http://www.fctec.com/fctec_types_afc.asp).
5. Mauritz, K. A.; Moore, R. B., State of understanding of Nafion. *Chem Rev* 2004, 104, 4535-4585.
6. Agel, E.; Bouet, J.; Fauvarque, J. F.; Yassir, H., The use of a solid polymer electrolyte in alkaline fuel cells. *Annales De Chimie-Science Des Materiaux* 2001, 26, 59-68.
7. Asazawa, K.; Yamada, K.; Tanaka, H.; Oka, A.; Taniguchi, M.; Kobayashi, T., A platinum-free zero-carbon-emission easy fuelling direct hydrazine fuel cell for vehicles. *Angew Chem Int Edit* 2007, 46, 8024-8027.
8. Christopher G. Arges, V. R., and Peter N. Pintauro, The Chalkboard: Anion Exchange Membrane Fuel Cells. *The electrochemical society's interface* 2010, 19, 31-15.
9. Merle, G.; Wessling, M.; Nijmeijer, K., Anion exchange membranes for alkaline fuel cells: A review. *J Membrane Sci* 2011, 377, 1-35.

10. Peckham, T. J.; Holdcroft, S., Structure-Morphology-Property Relationships of Non-Perfluorinated Proton-Conducting Membranes. *Adv Mater* 2010, 22, 4667-4690.
11. Kreuer, K. D.; Paddison, S. J.; Spohr, E.; Schuster, M., Transport in proton conductors for fuel-cell applications: Simulations, elementary reactions, and phenomenology. *Chem Rev* 2004, 104, 4637-4678.
12. Weber, A. Z.; Newman, J., Transport in polymer-electrolyte membranes - III. Model validation in a simple fuel-cell model. *J. Electrochem. Soc.* 2004, 151, A326-A339.
13. Weber, A. Z.; Newman, J., Transport in polymer-electrolyte membranes - II. Mathematical model. *J. Electrochem. Soc.* 2004, 151, A311-A325.
14. Grew, K. N.; Chiu, W. K. S., A Dusty Fluid Model for Predicting Hydroxyl Anion Conductivity in Alkaline Anion Exchange Membranes. *J. Electrochem. Soc.* 2010, 157, B327-B337.
15. Tuckerman, M. E.; Marx, D.; Parrinello, M., The nature and transport mechanism of hydrated hydroxide ions in aqueous solution. *Nature* 2002, 417, 925-929.
16. Vanysek, P., *Ionic conductivity and diffusion at infinite dilution*. 83rd ed. ed.; Physics: 2002.
17. Hibbs, M. R.; Hickner, M. A.; Alam, T. M.; McIntyre, S. K.; Fujimoto, C. H.; Cornelius, C. J., Transport properties of hydroxide and proton conducting membranes. *Chemistry of Materials* 2008, 20, 2566-2573.
18. Gierke, T. D.; Munn, G. E.; Wilson, F. C., THE MORPHOLOGY IN NAFION PERFLUORINATED MEMBRANE PRODUCTS, AS DETERMINED BY WIDE-

ANGLE AND SMALL-ANGLE X-RAY STUDIES. *Journal of Polymer Science Part B-Polymer Physics* 1981, 19, 1687-1704.

19. Schmidt-Rohr, K.; Chen, Q., Parallel cylindrical water nanochannels in Nafion fuel-cell membranes. *Nature Materials* 2008, 7, 75-83.

20. Miyatake, K.; Shimura, T.; Mikami, T.; Watanabe, M., Aromatic ionomers with superacid groups. *Chemical Communications* 2009, 6403-6405.

21. Yoshimura, K.; Iwasaki, K., Aromatic Polymer with Pendant Perfluoroalkyl Sulfonic Acid for Fuel Cell Applications. *Macromolecules* 2009, 42, 9302-9306.

22. Matsumoto, K.; Higashihara, T.; Ueda, M., Locally and Densely Sulfonated Poly(ether sulfone)s as Proton Exchange Membrane. *Macromolecules* 2009, 42, 1161-1166.

23. Roy, A.; Lee, H. S.; McGrath, J. E., Hydrophilic-hydrophobic multiblock copolymers based on poly(arylene ether sulfone)s as novel proton exchange membranes - Part B. *Polymer* 2008, 49, 5037-5044.

24. Bae, B.; Yoda, T.; Miyatake, K.; Uchida, H.; Watanabe, M., Proton-Conductive Aromatic Ionomers Containing Highly Sulfonated Blocks for High-Temperature-Operable Fuel Cells. *Angew Chem Int Edit* 2010, 49, 317-320.

25. Li, N.; Wang, C.; Lee, S. Y.; Park, C. H.; Lee, Y. M.; Guiver, M. D., Enhancement of Proton Transport by Nanochannels in Comb-Shaped Copoly(arylene ether sulfone)s. *Angew Chem Int Edit* 2011, 50, 9158-9161.

26. Tanaka, M.; Fukasawa, K.; Nishino, E.; Yamaguchi, S.; Yamada, K.; Tanaka, H.; Bae, B.; Miyatake, K.; Watanabe, M., Anion Conductive Block Poly(arylene ether)s:

- Synthesis, Properties, and Application in Alkaline Fuel Cells. *J Am Chem Soc* 2011, 133, 10646-10654.
27. Elabd, Y. A.; Hickner, M. A., Block Copolymers for Fuel Cells. *Macromolecules* 2011, 44, 1-11.
28. Li, N.; Hwang, D. S.; Lee, S. Y.; Liu, Y.-L.; Lee, Y. M.; Guiver, M. D., Densely Sulfophenylated Segmented Copoly(arylene ether sulfone) Proton Exchange Membranes. *Macromolecules* 2011, 44, 4901-4910.
29. Takamuku, S.; Jannasch, P., Multiblock Copolymers with Highly Sulfonated Blocks Containing Di- and Tetrasulfonated Arylene Sulfone Segments for Proton Exchange Membrane Fuel Cell Applications. *Advanced Energy Materials* 2012, 2, 129-140.
30. Nicotera, I.; Coppola, L.; Rossi, C. O.; Youssry, M.; Ranieri, G. A., NMR Investigation of the Dynamics of Confined Water in Nafion-Based Electrolyte Membranes at Subfreezing Temperatures. *J Phys Chem B* 2009, 113, 13935-13941.
31. Sierra-Martin, B.; Choi, Y.; Romero-Cano, M. S.; Cosgrove, T.; Vincent, B.; Fernandez-Barbero, A., Microscopic signature of a microgel volume phase transition. *Macromolecules* 2005, 38, 10782-10787.
32. Siu, A.; Schmeisser, J.; Holdcroft, S., Effect of water on the low temperature conductivity of polymer electrolytes. *J Phys Chem B* 2006, 110, 6072-6080.
33. Thompson, E. L.; Capehart, T. W.; Fuller, T. J.; Jorne, J., Investigation of low-temperature proton transport in Nafion using direct current conductivity and differential scanning calorimetry. *J. Electrochem. Soc.* 2006, 153, A2351-A2362.

34. Mecheri, B.; Felice, V.; Zhang, Z.; D'Epifanio, A.; Licoccia, S.; Tavares, A. C., DSC and DVS Investigation of Water Mobility in Nafion/Zeolite Composite Membranes for Fuel Cell Applications. *Journal of Physical Chemistry C* 2012, 116, 20820-20829.
35. Noonan, K. J. T.; Hugar, K. M.; Kostalik, H. A.; Lobkovsky, E. B.; Abruna, H. D.; Coates, G. W., Phosphonium-Functionalized Polyethylene: A New Class of Base-Stable Alkaline Anion Exchange Membranes. *J Am Chem Soc* 2012, 134, 18161-18164.
36. Thomas, O. D.; Soo, K.; Peckham, T. J.; Kulkarni, M. P.; Holdcroft, S., A Stable Hydroxide-Conducting Polymer. *J Am Chem Soc* 2012, 134, 10753-10756.
37. Fujimoto, C.; Kim, D. S.; Hibbs, M.; Wroblewski, D.; Kim, Y. S., Backbone stability of quaternized polyaromatics for alkaline membrane fuel cells. *J Membrane Sci* 2012, 423, 438-449.
38. Yan, J. L.; Hickner, M. A., Anion Exchange Membranes by Bromination of Benzylmethyl-Containing Poly(sulfone)s. *Macromolecules* 2010, 43, 2349-2356.
39. Zhou, J. F.; Unlu, M.; Anestis-Richard, I.; Kohl, P. A., Crosslinked, epoxy-based anion conductive membranes for alkaline membrane fuel cells. *J Membrane Sci* 2010, 350, 286-292.
40. Zhou, J.; Uenlue, M.; Anestis-Richard, I.; Kim, H.; Kohl, P. A., Solvent processible, high-performance partially fluorinated copoly (arylene ether) alkaline ionomers for alkaline electrodes. *Journal of Power Sources* 2011, 196, 7924-7930.
41. Robertson, N. J.; Kostalik, H. A.; Clark, T. J.; Mutolo, P. F.; Abruna, H. D.; Coates, G. W., Tunable High Performance Cross-Linked Alkaline Anion Exchange Membranes for Fuel Cell Applications. *J Am Chem Soc* 2010, 132, 3400-3404.

42. Luo, Y. T.; Guo, J. C.; Wang, C. S.; Chu, D., Quaternized poly(methyl methacrylate-co-butyl acrylate-co-vinylbenzyl chloride) membrane for alkaline fuel cells. *Journal of Power Sources* 2010, 195, 3765-3771.
43. Thomas, O. D.; Soo, K.; Peckham, T. J.; Kulkarni, M. P.; Holdcroft, S., Anion conducting poly(dialkyl benzimidazolium) salts. *Polymer Chemistry* 2011, 2, 1641-1643.
44. Bae, B.; Miyatake, K.; Watanabe, M., Sulfonated Poly(arylene ether sulfone ketone) Multiblock Copolymers with Highly Sulfonated Block. Synthesis and Properties. *Macromolecules* 2010, 43, 2684-2691.
45. Na, T. Y.; Shao, K.; Zhu, J.; Sun, H. C.; Liu, Z. G.; Zhao, C. J.; Zhang, Z. Q.; Lew, C. M.; Zhang, G., Block sulfonated poly(arylene ether ketone) containing flexible side-chain groups for direct methanol fuel cells usage. *J Membrane Sci* 2012, 417, 61-68.
46. Zhang, X.; Hu, Z.; Luo, L.; Chen, S.; Liu, J.; Chen, S.; Wang, L., Graft-crosslinked Copolymers Based on Poly(arylene ether ketone)-g-sulfonated Poly(arylene ether sulfone) for PEMFC Applications. *Macromolecular Rapid Communications* 2011, 32, 1108-1113.
47. Nakajima, T.; Tamaki, T.; Ohashi, H.; Yamaguchi, T., Systematic Evaluation of Polymer Electrolyte Fuel Cell Electrodes with Hydrocarbon Polyelectrolytes by Considering the Polymer Properties. *Journal of Physical Chemistry C* 2012, 116, 1422-1428.
48. Zhou, X. M.; Jiang, Z. H., Sequence analysis of poly (ether sulfone) copolymers by C-13 NMR. *Journal of Polymer Science Part B-Polymer Physics* 2005, 43, 1624-1630.

49. Lee, H.-S.; Roy, A.; Lane, O.; Dunn, S.; McGrath, J. E., Hydrophilic-hydrophobic multiblock copolymers based on poly(arylene ether sulfone) via low-temperature coupling reactions for proton exchange membrane fuel cells. *Polymer* 2008, 49, 715-723.
50. Wang, G.; Weng, Y.; Chu, D.; Chen, R.; Xie, D., Developing a polysulfone-based alkaline anion exchange membrane for improved ionic conductivity. *J Membrane Sci* 2009, 332, 63-68.
51. Khandelwal, D.; Hooda, S.; Brar, A. S.; Shankar, R., 1D and 2D NMR studies of isobornyl acrylate - Methyl methacrylate copolymers. *Journal of Molecular Structure* 2011, 1004, 121-130.
52. Khandpur, A. K.; Forster, S.; Bates, F. S.; Hamley, I. W.; Ryan, A. J.; Bras, W.; Almdal, K.; Mortensen, K., Polyisoprene-polystyrene diblock copolymer phase diagram near the order-disorder transition. *Macromolecules* 1995, 28, 8796-8806.
53. Leibler, L., Theory of microphase separation in block copolymers. *Macromolecules* 1980, 13, 1602-1617.
54. Li, N. W.; Hwang, D. S.; Lee, S. Y.; Liu, Y. L.; Lee, Y. M.; Guiver, M. D., Densely Sulfophenylated Segmented Copoly(arylene ether sulfone) Proton Exchange Membranes. *Macromolecules* 2011, 44, 4901-4910.
55. Neves, L. A.; Sebastiao, P. J.; Coelho, I. M.; Crespo, J. G., Proton NMR Relaxometry Study of Nafion Membranes Modified with Ionic Liquid Cations. *J Phys Chem B* 2011, 115, 8713-8723.
56. Perrin, J. C.; Lyonnard, S.; Guillermo, A.; Levitz, P., Water dynamics in ionomer membranes by field-cycling NMR relaxometry. *J Phys Chem B* 2006, 110, 5439-5444.

57. Kunze, M.; Karatas, Y.; Wiemhoefer, H.-D.; Eckert, H.; Schoenhoff, M., Activation of transport and local dynamics in polysiloxane-based salt-in-polymer electrolytes: a multinuclear NMR study. *Physical Chemistry Chemical Physics* 2010, 12, 6844-6851.
58. Tsang, E. M. W.; Zhang, Z. B.; Yang, A. C. C.; Shi, Z. Q.; Peckham, T. J.; Narimani, R.; Frisken, B. J.; Holdcroft, S., Nanostructure, Morphology, and Properties of Fluorous Copolymers Bearing Ionic Grafts. *Macromolecules* 2009, 42, 9467-9480.
59. Peckham, T. J.; Schmeisser, J.; Rodgers, M.; Holdcroft, S., Main-chain, statistically sulfonated proton exchange membranes: the relationships of acid concentration and proton mobility to water content and their effect upon proton conductivity. *J Mater Chem* 2007, 17, 3269-3269.
60. Karlsson, L. E.; Wesslen, B.; Jannasch, P., Water absorption and proton conductivity of sulfonated acrylamide copolymers. *Electrochimica Acta* 2002, 47, 3269-3275.
61. Wu, X. M.; He, G. H.; Gu, S.; Hu, Z. W.; Yan, X. M., The state of water in the series of sulfonated poly (phthalazinone ether sulfone ketone) (SPPEsk) proton exchange membranes. *Chemical Engineering Journal* 2010, 156, 578-581.
62. Kim, D. S.; Park, H. B.; Jang, J. Y.; Lee, Y. M., Synthesis of sulfonated poly(imidoaryl ether sulfone) membranes for polymer electrolyte membrane fuel cells. *J. Polym. Sci. Pol. Chem.* 2005, 43, 5620-5631.
63. Hwang, B. J.; Joseph, J.; Zeng, Y. Z.; Lin, C. W.; Cheng, M. Y., Analysis of states of water in poly (vinyl alcohol) based DMFC membranes using FTIR and DSC. *J Membrane Sci* 2011, 369, 88-95.

64. Kunimatsu, K.; Bae, B.; Miyatake, K.; Uchida, H.; Watanabe, M., ATR-FTIR Study of Water in Nafion Membrane Combined with Proton Conductivity Measurements during Hydration/Dehydration Cycle. *J Phys Chem B* 2011, 115, 4315-4321.
65. Hirata, Y.; Miura, Y.; Nakagawa, T., Oxygen permeability and the state of water in Nafion((R)) membranes with alkali metal and amino sugar counterions. *J Membrane Sci* 1999, 163, 357-366.
66. Lu, Z. J.; Polizos, G.; Macdonald, D. D.; Manias, E., State of water in perfluorosulfonic ionomer (Nafion 117) proton exchange membranes. *J. Electrochem. Soc.* 2008, 155, B163-B171.
67. Yang, Y. N.; Zhang, H. X.; Wang, P.; Zheng, Q. Z.; Li, J., The influence of nano-sized TiO<sub>2</sub> fillers on the morphologies and properties of PSFUF membrane. *J Membrane Sci* 2007, 288, 231-238.
68. Moster, A. L.; Mitchell, B. S., Hydration and Proton Conduction in Nafion/Ceramic Nanocomposite Membranes Produced by Solid-State Processing of Powders from Mechanical Attrition. *Journal of Applied Polymer Science* 2009, 113, 243-250.
69. Lingwood, M. D.; Zhang, Z.; Kidd, B. E.; McCreary, K. B.; Hou, J.; Madsen, L. A., Unraveling the local energetics of transport in a polymer ion conductor. *Chemical Communications* 2013, 49, 4283-4285.
70. Eikerling, M.; Kornyshev, A. A.; Kuznetsov, A. M.; Ulstrup, J.; Walbran, S., Mechanisms of proton conductance in polymer electrolyte membranes. *J Phys Chem B* 2001, 105, 3646-3662.

71. Merinov, B. V.; Goddard, W. A., Computational modeling of structure and OH<sup>-</sup> anion diffusion in quaternary ammonium polysulfone hydroxide - Polymer electrolyte for application in electrochemical devices. *J Membrane Sci* 2013, 431, 79-85.
72. Stejskal, E. O.; Tanner, J. E., Spin diffusion measurements: spin echoes in the presence of a time dependent field gradient. *Journal of Chemical Physics* 1965, 42, 288-292.
73. Tanaka, M.; Koike, M.; Miyatake, K.; Watanabe, M., Synthesis and properties of anion conductive ionomers containing fluorenyl groups for alkaline fuel cell applications. *Polymer Chemistry* 2011, 2, 99-106.
74. Deavin, O. I.; Murphy, S.; Ong, A. L.; Poynton, S. D.; Zeng, R.; Herman, H.; Varcoe, J. R., Anion-exchange membranes for alkaline polymer electrolyte fuel cells: comparison of pendent benzyltrimethylammonium- and benzylmethylimidazolium-head-groups. *Energy & Environmental Science* 2012, 5, 8584-8597.
75. Nuñez, S. A.; Hickner, M. A., Quantitative <sup>1</sup>H NMR Analysis of Chemical Stabilities in Anion-Exchange Membranes. *ACS Macro Letters* 2012, 2, 49-52.
76. Ye, Y. S.; Elabd, Y. A., Relative Chemical Stability of Imidazolium-Based Alkaline Anion Exchange Polymerized Ionic Liquids. *Macromolecules* 2011, 44, 8494-8503.
77. Yuesheng, Y.; Yossef, A. E., Chemical Stability of Anion Exchange Membranes for Alkaline Fuel Cells. In *Polymers for Energy Storage and Delivery: Polyelectrolytes for Batteries and Fuel Cells*, American Chemical Society: 2012; Vol. 1096, pp 233-251.

78. Johnson, C. S., Diffusion ordered nuclear magnetic resonance spectroscopy: principles and applications. *Progress in Nuclear Magnetic Resonance Spectroscopy* 1999, 34, 203-256.
79. Junfeng Zhou, K. J., John M. Ahlfield, Doh-Yeon Park, and Paul A. Kohl, Poly(arylene ether) Ionomers with Pendant Quinuclidium Groups and Varying Molecular Weight for Alkaline Electrodes. *Submitted* 2013.
80. Arges, C. G.; Ramani, V., Two-dimensional NMR spectroscopy reveals cation-triggered backbone degradation in polysulfone-based anion exchange membranes. *Proceedings of the National Academy of Sciences of the United States of America* 2013, 110, 2490-2495.
81. Mizuno, K.; Miyashita, Y.; Shindo, Y.; Ogawa, H., NMR and FT-IR studies of hydrogen-bonds in ethanol-water mixture. *Journal of Physical Chemistry* 1995, 99, 3225-3228.
82. Macomber, C. S.; Boncella, J. M.; Pivovar, B. S.; Rau, J. A., Decomposition pathways of an alkaline fuel cell membrane material component via evolved gas analysis. *Journal of Thermal Analysis and Calorimetry* 2008, 93, 225-229.
83. Sata, T.; Tsujimoto, M.; Yamaguchi, T.; Matsusaki, K., Change of anion exchange membranes in an aqueous sodium hydroxide solution at high temperature. *J Membrane Sci* 1996, 112, 161-170.
84. Carrette, L.; Friedrich, K. A.; Stimming, U., Fuel Cells - Fundamentals and Applications. *Fuel Cells* 2001, 1, 5-39.
85. Xu, K., Nonaqueous liquid electrolytes for lithium-based rechargeable batteries. *Chem Rev* 2004, 104, 4303-4417.

86. Kim, Y.; Shin, D.; Seo, J.; Chang, N.; Cho, H.; Kim, Y.; Yoon, S., System integration of a portable direct methanol fuel cell and a battery hybrid. *International Journal of Hydrogen Energy* 2010, 35, 5621-5637.
87. Joseph, K. S., Hybrid direct methanol fuel cells. *Dissertation, Georgia Institute of Technology* 2012.
88. Tripkovic, A. V.; Popovic, K. D.; Grgur, B. N.; Blizanac, B.; Ross, P. N.; Markovic, N. M., Methanol electrooxidation on supported Pt and PtRu catalysts in acid and alkaline solutions. *Electrochimica Acta* 2002, 47, 3707-3714.
89. Li, Y. S.; Zhao, T. S.; Chen, R., Cathode flooding behaviour in alkaline direct ethanol fuel cells. *Journal of Power Sources* 2011, 196, 133-139.
90. Unlu, M.; Zhou, J. F.; Kohl, P. A., Hybrid Polymer Electrolyte Fuel Cells: Alkaline Electrodes with Proton Conducting Membrane. *Angew Chem Int Edit* 2010, 49, 1299-1301.
91. Unlu, M.; Zhou, J. F.; Anestis-Richard, I.; Kim, H.; Kohl, P. A., Improved gas diffusion electrodes for hybrid polymer electrolyte fuel cells. *Electrochimica Acta* 2011, 56, 4439-4444.
92. Kazock, J. Y.; Taggougui, M.; Anouti, M.; Willman, P.; Carre, B.; Lemordant, D., Ionic liquids based on 1-aza-bicyclo 2,2,2 octane (Quinuclidine) salts: synthesis and physicochemical properties. *Journal of Applied Electrochemistry* 2009, 39, 2461-2467.
93. Scott, K.; Yu, E.; Vlachogiannopoulos, G.; Shivare, M.; Duteanu, N., Performance of a direct methanol alkaline membrane fuel cell. *Journal of Power Sources* 2008, 175, 452-457.

94. Park, M. J.; Balsara, N. P., Anisotropic Proton Conduction in Aligned Block Copolymer Electrolyte Membranes at Equilibrium with Humid Air. *Macromolecules* 2010, 43, 292-298.
95. Hou, J.; Li, J.; Madsen, L. A., Anisotropy and Transport in Poly(arylene ether sulfone) Hydrophilic-Hydrophobic Block Copolymers. *Macromolecules* 2010, 43, 347-353.
96. Park, M. J.; Balsara, N. P., Phase behavior of symmetric sulfonated block copolymers. *Macromolecules* 2008, 41, 3678-3687.
97. Gu, S.; Cai, R.; Luo, T.; Chen, Z.; Sun, M.; Liu, Y.; He, G.; Yan, Y., A Soluble and Highly Conductive Ionomer for High-Performance Hydroxide Exchange Membrane Fuel Cells. *Angewandte Chemie International Edition* 2009, 48, 6499-6502.
98. Gu, S.; Cai, R.; Luo, T.; Jensen, K.; Contreras, C.; Yan, Y. S., Quaternary Phosphonium-Based Polymers as Hydroxide Exchange Membranes. *Chemsuschem* 2010, 3, 555-558.
99. Wang, J. H.; Li, S. H.; Zhang, S. B., Novel Hydroxide-Conducting Polyelectrolyte Composed of an Poly(arylene ether sulfone) Containing Pendant Quaternary Guanidinium Groups for Alkaline Fuel Cell Applications. *Macromolecules* 2010, 43, 3890-3896.
100. Li, W.; Fang, J.; Lv, M.; Chen, C.; Chi, X.; Yang, Y.; Zhang, Y., Novel anion exchange membranes based on polymerizable imidazolium salt for alkaline fuel cell applications. *J Mater Chem* 2011, 21, 11340-11346.

101. Hnat, J.; Paidar, M.; Schauer, J.; Zitka, J.; Bouzek, K., Polymer anion selective membranes for electrolytic splitting of water. Part I: stability of ion-exchange groups and impact of the polymer binder. *Journal of Applied Electrochemistry* 2011, 41, 1043-1052.
102. Wu, Y. H.; Wu, C. M.; Xu, T. W.; Lin, X. C.; Fu, Y. X., Novel silica/poly(2,6-dimethyl-1,4-phenylene oxide) hybrid anion-exchange membranes for alkaline fuel cells: Effect of heat treatment. *J Membrane Sci* 2009, 338, 51-60.
103. Lue, S. J.; Wang, W. T.; Mahesh, K. P. O.; Yang, C. C., Enhanced performance of a direct methanol alkaline fuel cell (DMAFC) using a polyvinyl alcohol/fumed silica/KOH electrolyte. *Journal of Power Sources* 2010, 195, 7991-7999.
104. Wang, E. D.; Zhao, T. S.; Yang, W. W., Poly (vinyl alcohol)/3-(trimethylammonium) propyl-functionalized silica hybrid membranes for alkaline direct ethanol fuel cells. *International Journal of Hydrogen Energy* 2010, 35, 2183-2189.
105. Kim, P.; Jones, S. C.; Hotchkiss, P. J.; Haddock, J. N.; Kippelen, B.; Marder, S. R.; Perry, J. W., Phosphonic acid-modified barium titanate polymer nanocomposites with high permittivity and dielectric strength. *Adv Mater* 2007, 19, 1001-+.
106. Alonso, R. H.; Estevez, L.; Lian, H. Q.; Kellarakis, A.; Giannelis, E. P., Nafion-clay nanocomposite membranes: Morphology and properties. *Polymer* 2009, 50, 2402-2410.
107. Sheiko, S. S.; Gerle, M.; Fischer, K.; Schmidt, M.; Moller, M., Wormlike polystyrene brushes in thin films. *Langmuir* 1997, 13, 5368-5372.
108. Zhang, A. F.; Shu, L. J.; Bo, Z. S.; Schluter, A. D., Dendronized polymers: Recent progress in synthesis. *Macromolecular Chemistry and Physics* 2003, 204, 328-339.

109. Sheiko, S. S.; Sumerlin, B. S.; Matyjaszewski, K., Cylindrical molecular brushes: Synthesis, characterization, and properties. *Progress in Polymer Science* 2008, 33, 759-785.
110. Teuchert, C.; Michel, C.; Hansen, F.; Park, D. Y.; Beckham, H. W.; Wenz, G., Cylindrical Polymer Brushes by Atom Transfer Radical Polymerization from Cyclodextrin-PEG Polyrotaxanes: Synthesis and Mechanical Stability. *Macromolecules* 2013, 46, 2-7.
111. Zhao, T. J.; Beckham, H. W., Direct synthesis of cyclodextrin-rotaxanated poly(ethylene glycol)s and their self-diffusion behavior in dilute solution. *Macromolecules* 2003, 36, 9859-9865.